British Geological Survey

NATURAL ENVIRONMENT RESEARCH COUNCIL

Final Report of FORGE WP4.1.1: The stress-path permeameter experiment conducted on Callovo-Oxfordian Claystone

Minerals and Waste Programme

Commissioned Report CR/12/140

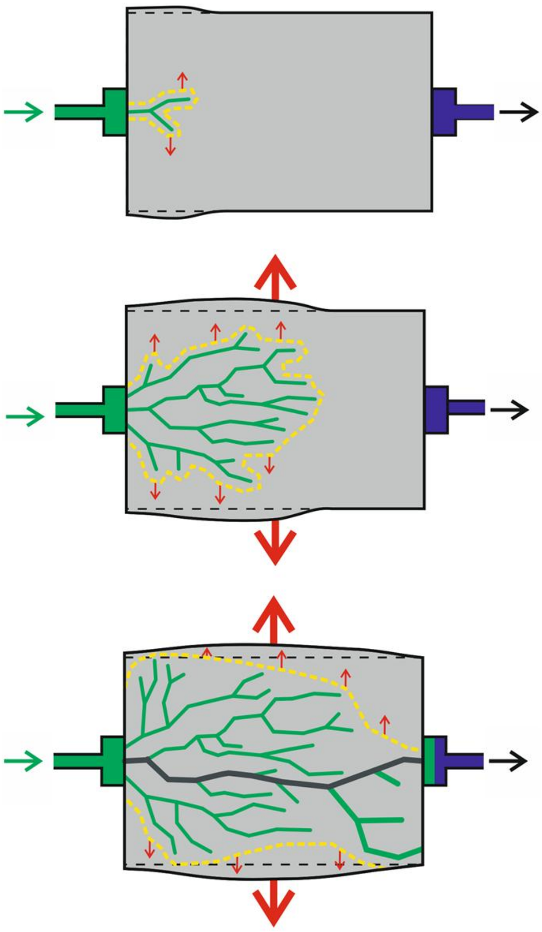

BRITISH GEOLOGICAL SURVEY

MINERALS AND WASTE PROGRAMME

COMMISSIONED REPORT CR/12/140

Final Report of FORGE WP4.1.1: The stress-path permeameter experiment conducted on Callovo-Oxfordian Claystone

R.J. Cuss, J.F. Harrington, and D.J. Noy

Keywords

SPP, FORGE, stress-path testing, Callovo-Oxfordian claystone, COx, dilatancy flow.

Front cover

Conceptual model of dilatancy flow seen in Callovo-Oxfordian Claystone.

Bibliographical reference

CUSS, R.J., HARRINGTON, J.F., and NOY, D.J. 2012. Final Report of FORGE WP4.1.1: The stress-path permeameter experiment conducted on Callovo-Oxfordian Claystone. *British Geological Survey Commissioned Report,* CR/12/140. 116pp.

Keyworth, Nottingham British Geological Survey 2012

BRITISH GEOLOGICAL SURVEY

The full range of our publications is available from BGS shops at Nottingham, Edinburgh, London and Cardiff (Welsh publications only) see contact details below or shop online at www.geologyshop.com

The London Information Office also maintains a reference collection of BGS publications, including maps, for consultation.

We publish an annual catalogue of our maps and other publications; this catalogue is available online or from any of the BGS shops.

The British Geological Survey carries out the geological survey of Great Britain and Northern Ireland (the latter as an agency service for the government of Northern Ireland), and of the surrounding continental shelf, as well as basic research projects. It also undertakes programmes of technical aid in geology in developing countries.

The British Geological Survey is a component body of the Natural Environment Research Council.

British Geological Survey offices

BGS Central Enquiries Desk
Tel 0115 936 3143 Fax 0115 936 3276
email enquires@bgs.ac.uk

Kingsley Dunham Centre, Keyworth, Nottingham NG12 5GG
Tel 0115 936 3241 Fax 0115 936 3488
email sales@bgs.ac.uk

Murchison House, West Mains Road, Edinburgh EH9 3LA
Tel 0131 667 1000 Fax 0131 668 2683
email scotsales@bgs.ac.uk

London Information Office at the Natural History Museum (Earth Galleries), Exhibition Road, South Kensington, London SW7 2DE
Tel 020 7589 4090 Fax 020 7584 8270
Tel 020 7942 5344/45 email bgslondon@bgs.ac.uk

Columbus House, Greenmeadow Springs, Tongwynlais, Cardiff CF15 7NE
Tel 029 2052 1962 Fax 029 2052 1963

Forde House, Park Five Business Centre, Harrier Way, Sowton EX2 7HU
Tel 01392 445271 Fax 01392 445371

Maclean Building, Crowmarsh Gifford, Wallingford OX10 8BB
Tel 01491 838800 Fax 01491 692345

Geological Survey of Northern Ireland, Colby House, Stranmillis Court, Belfast BT9 5BF
Tel 028 9038 8462 Fax 028 9038 8461

www.bgs.ac.uk/gsni/

Parent Body

Natural Environment Research Council, Polaris House, North Star Avenue, Swindon SN2 1EU
Tel 01793 411500 Fax 01793 411501
www.nerc.ac.uk

Website www.bgs.ac.uk
Shop online at www.geologyshop.com

Foreword

This report is the product of a study by the British Geological Survey (BGS) undertaken on behalf of the French radioactive waste management company Agence Nationale pour la Gestion des Déchets Radioactifs (Andra) and the European Union 7th Framework Euratom Programme under the auspices of the Fate of repository Gases (FORGE) project, to examine the effect of the stress-path on the hydraulic and gas transport properties of the Callovo-Oxfordian claystone.

Acknowledgements

The study was undertaken by staff of the Minerals and Waste Programme of the BGS using the experimental facilities of the Transport Properties Research Laboratory (TPRL). Funding for the study was provided by the French radioactive waste management operator, Andra, the European Union (FORGE Project) and the British Geological Survey through its well-founded laboratory programme. The authors would like to thank the skilled staff of the Research & Development Workshops at the BGS, in particular Humphrey Wallis and Steve Upton, for their design and construction of the experimental apparatus, Neil Stacey of the BGS Core Store for his skilled preparation of the samples tested and Pete Hobbs for his assistance in using SHRINKiT to measure the final dimensions of the test sample.

Contents

FIGURES

TABLES

Executive summary

This report describes in detail the stress-path permeameter (SPP) apparatus and the test programme conducted on Callovo-Oxfordian (COx) Claystone from the Bure underground research laboratory (URL) in France. Funding for this study has been provided by the French radioactive waste management operator, Andra, the European Union (FORGE Project, Project number 230357) and the British Geological Survey through its well-founded laboratory programme and the Geosphere Containment project (part of the BGS core strategic programme).

The results from the first test conducted using the SPP showed that COx has a very pronounced time-dependent component of deformation. This had implications for the following test conducted on COx and also has implications when comparing tests that have been deformed at a much faster rate.

Test SPP_COx-1 was conducted with water as a test permeant at constant pore-pressure along a pre-defined stress-path. Volumetric deformation was observed during 16 steps along the stress-path, with considerable time-dependent deformation and anisotropy seen in radial strain. The 16th stage saw the sample fail through the formation of a fracture after the sample had experienced constant stress conditions for 5.5 days; this emphasises the observed time dependent deformation.

The results from test SPP_COx-2 clearly showed that the sample dilated at the onset of gas propagation; dilatancy was observed in three radial and one axial direction. A component of this volumetric deformation was associated with changes in pore-pressure. However, pore-pressure variation cannot account for the full amount of strain recorded and a proportion of the strain observed was the result of gas migration by dilatant pathway formation. Prior to the sample attaining steady-state flow, outflow from the sample slowly reduced and the conductive features experienced self-sealing. Gas injection pressure was raised and back-pressure was carefully lowered; neither course of action re-initiated flow through the sample.

1 Introduction

The original objective of the experimental programme was to examine the impact of changing effective stress (e.g. caused by the construction of a disposal/storage facility) and its effect on the sealing characteristics of the Callovo-Oxfordian (COx) claystone. As such, there is a need to understand the roles of the stress tensor, the stress-path and associated mechanical deformation in determining permeability changes affecting the sealing efficiency of the claystone. A secondary objective of the experimental programme was to determine the volumetric deformation observed during the onset of gas flow and to discriminate between flow mechanisms.

As will be described in detail, two experiments were conducted in the experimental programme. The first test, SPP_COx-1, aimed to define the bulk volumetric deformation of a sample during progression along a stress-path through to ultimate failure. Unforeseen was the strong observed time-dependent deformation caused by changes of boundary condition. This meant that mechanical tests had to have long test stages in order to allow the COx to fully equilibrate to the boundary conditions. The second test conducted, SPP_COx-2, had a much greater gas entry pressure than had been anticipated. This proved problematic as a gas entry close to confining pressure results in little scope to alter the stress-path and as a result a stress-path leading to failure could not be achieved. Prior to altering the stress field, flow in the sample stopped and the conductive pathways self-sealed; this too was unexpected. Therefore metrology limited the ability of the study to fully achieve the primary aims and as a result the secondary aim of the study became the focus of investigation.

Under certain stress conditions, mudrock deformation will result in dilation (net volume increase) or contraction (net volume decrease). The boundary between these conditions is referred to as the dilatancy boundary and this plots as a point in the mean stress (p) versus deviatoric stress (q) space, or a line when specific volume (v) is used as a third axis. Critical state mechanics shows that complex deformation can be described by a series of yield surfaces in the $p' - q' - v$ parametric space. Calibration of this model can be undertaken by taking samples of mudrock along predefined stress-paths extending to the yield surfaces while measuring the resulting changes in permeability (both aqueous and gaseous). The main output of the research will be to enhance process understating in Engineering Disturbed Zone (EDZ) mudrock environments, through the critical examination and subsequent validity of key geomechanical relationships applied to mudrock deformation and its role in the temporal evolution of permeability during the operational and post closure repository phases.

1.1 DEFORMATION AND CRITICAL STATE CONCEPTS

Roscoe *et al*. (1958), proposed the critical state theory of soils, which provides a unified model of behaviour where stress states and volume states are interrelated. Gerogiannopoulos & Brown later modified this theory in 1978, to account for the brittle or work-softening behaviour of rocks. Shah (1997) also showed that further modification is required to the classical critical state model to account for the tensile strength of rocks, as soils are assumed to have zero tensile strength.

The *state* of shale subject to a simple stress field is defined by its position in the effective stress (p') – differential stress (q') – void ratio (v) parametric space. A change in state can be represented as a *path* within the p' - q' - v space. The projection of this change in the p' - q' space is referred to as the stress-path. The deformation path can be used to describe fully the deformation history of the rock and can be used to infer certain aspects of the deformation, such as whether it is drained or undrained, etc. Thus a complex deformation history can be represented and described by critical state theory.

A model is proposed where an isotropic soil yields, i.e. passes from purely elastic to elastoplastic behaviour, at a critical specific volume ($v_c = 1 + e_c$). Yielding or shear slipping is considered to occur as a combination of effective stress (σ'_1, σ'_2, σ'_3) and specific volume (v_c) coinciding with a state boundary surface. Experimentation has shown that when sheared, a deforming rock will tend towards criticality, a state where large shear distortions will occur without any further changes in p', q', or v (Roscoe & Burland, 1968; Schofield & Wroth, 1968). The critical state line (CSL) is the locus of all possible critical states in the p' - q' - v parametric space. Figure 1-1 shows a soil yield surface, which can be split into three distinct surfaces: the tension, Hvorslev, and Roscoe surfaces. The normal consolidation (NCL) and critical state (CSL) lines bound these surfaces, which are geometrically and, to a degree, physically equivalent to a Mohr-Coulomb type failure surface for porous rocks (Jones *et al.*, 1987; Loe *et al.*, 1992).

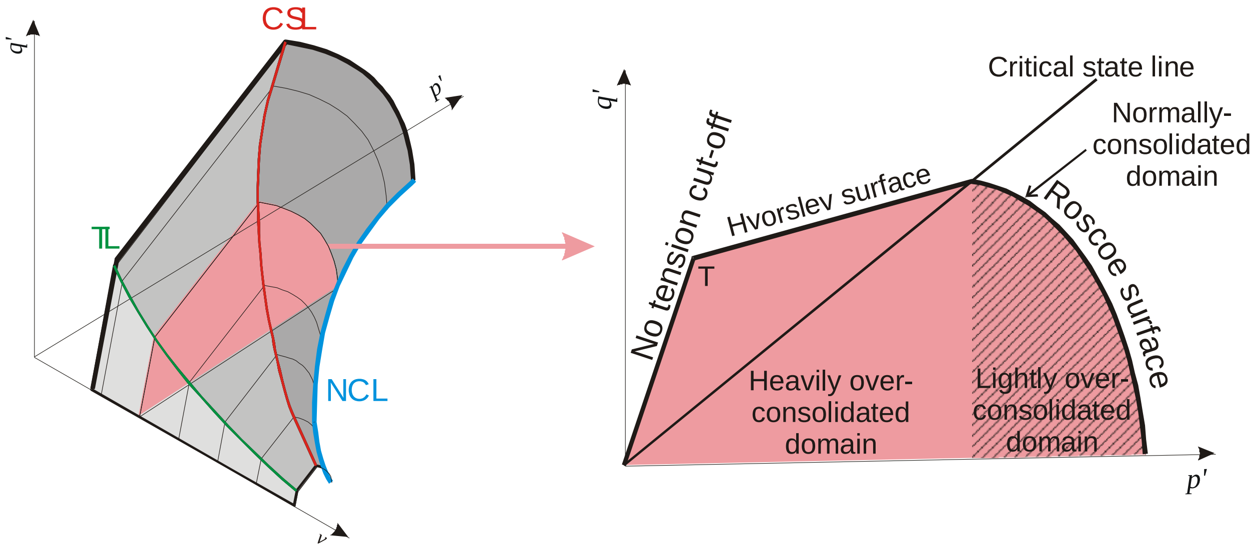

Figure 1-1 The critical state model of soil mechanics, showing the relationship of the tension line (TL), normal consolidation line (NCL) and critical state line (CSL). These lines bound the Hvorslev and Roscoe surfaces in the p' - q' space.

During consolidation under isotropic stress the volume change path will move along the NCL, which is in the plane of zero deviatoric stress (i.e. when stress in all directions is equal). The volumetric strain during consolidation is considered to have elastic (recoverable) and plastic (non-recoverable) components (Scholfied & Wroth, 1968). Figure 1-2b-d shows the paths a material would take in drained (reducing volume path $C \rightarrow D$) and undrained (constant volume path $C \rightarrow U$) tests. Yield occurs at U_1, D_1, U_2, D_2, U_3, and D_3; in the p' - q' - v space this line represents the CSL. On unloading, deformed sediments will only recover the elastic component of deformation; plastic deformation by definition is non-recoverable. The path then follows the rebound-reconsolidation line (RRL), also known as the swelling line.

1.1.1 Critical state theory and real sediments

There are many examples within the literature of studies on soils and clays that demonstrate the validity of critical state theory and the use of the Cam-clay derived models; including: Adams & Wulfsohn (1997), Cotecchia & Chandler (2000), Diaz-Rodriguez *et al.* (1992), Kirby (1994) Kirby & O'Sullivan (1997), Maâtouk *et al.* (1995), Mitchell (1970), Petley (1999), Tavenas & Leroueil (1977), and Wheeler & Sivakumar (1995). Kirby & O'Sullivan (1997) clearly show how successfully the modified Cam-clay critical state model, with only five material property parameters (*M*, *λ*, *k*, *E* and *η*[1]), reproduces non-linear soil deformation behaviour in four dimensions.

The simplistic model of critical state theory is complicated in rocks by features that are generally absent in soils. The concepts of, and relationships between, consolidation and shear are quantitatively valid for clays, fine carbonates, and sands where grain size and angularity do not cause dilatation during shear. For coarse angular grained clastic sediments the critical state concept must be modified to incorporate hardening associated with dilatant shear. Pore volume increase is minimal if high porosities are maintained, and as structure becomes more densely packed the dilatation effects become more pronounced. Yield surface form is unaltered, although deformation paths for dilatant materials will be more complex. Shear deformation is complicated at low stresses by elastic stiffness created by intergranular bonding. Studies show a consistent deformation style irrespective of sediment type and strength (Jones, 1994; Vaughan, 1985). Chalk shows a marked behaviour change with increased stress that is more complex than the ideal critical state behaviour; similar features have been observed in bonded mudrocks, carbonates, and sand (Jones, 1994).

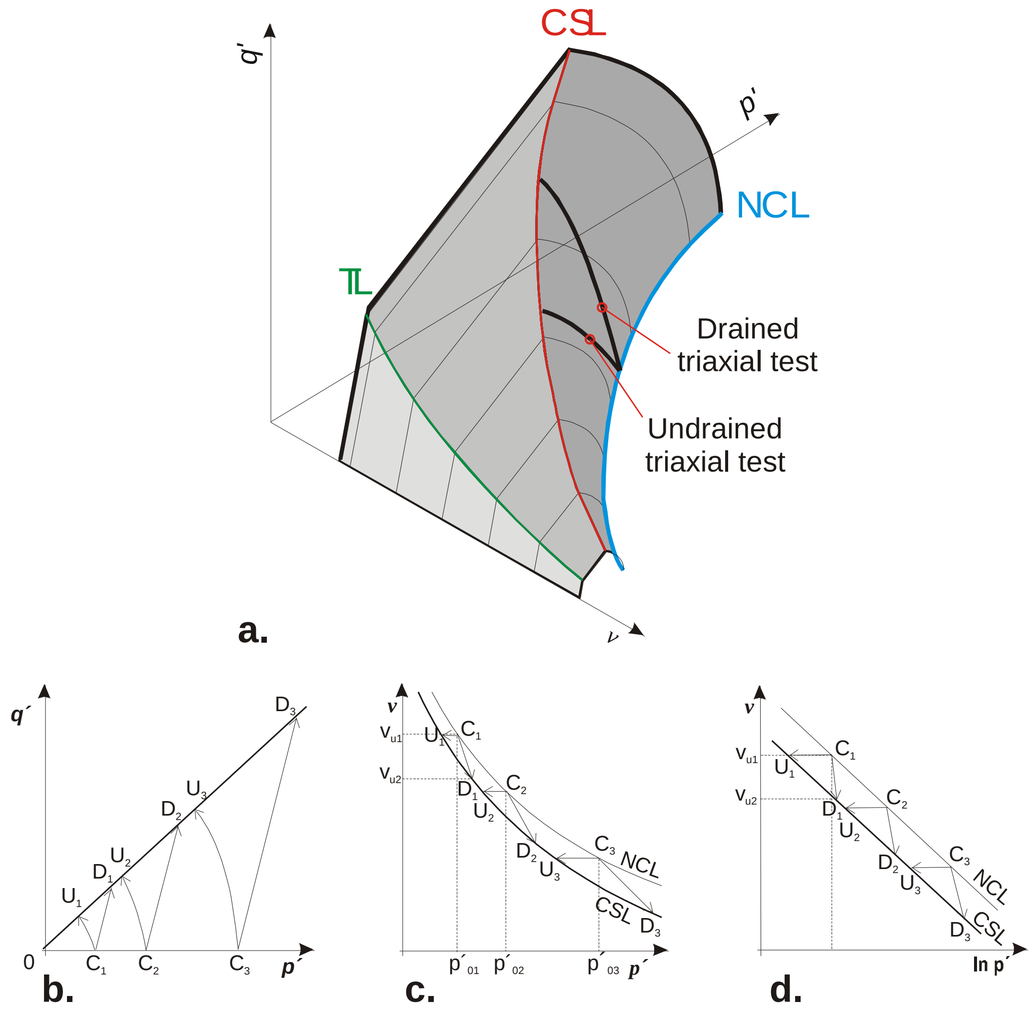

Figure 1-2 The critical state model of soil mechanics in detail. a) The state boundary surface for a particulate sediment (after Atkinson & Bransby, 1978). b-d) p' - q' - v plots of triaxial test results for drained (D) and undrained (U) tests. The stress-path for all tests tends towards the critical state line where critical state deformation continues.

---

[1] *E* is the elastic modulus and *η* is the Poisson's ratio of the soil

At low consolidation stresses, mudstones and sandstones reach the state boundary in an intact bonded condition. Stresses beyond the state boundary can be supported until interception of the peak strength envelope occurs resulting in shear failure. A stress drop is experienced from peak strength to residual strength, as the newly formed shear fracture can no longer support loads above the state boundary. These observations have been shown experimentally in sandstones and mudrocks (Leddra *et al*., 1993; Leddra *et al*., 1992; Petley *et al*., 1992).

What occurs at intermediate and high consolidation stresses is difficult to observe in many rock types as pervasive disaggregation renders test material an incohesive powder. Dissagregation means materials cannot support stresses above the CSL. At the critical state, shear deformation is pervasive and accompanied by grain sliding and rotation.

The critical state concept and yield surface provide a powerful and effective framework in which all aspects of porous sediment deformation and evolution can be described and interrelated. Complex burial and stress-porosity histories can be described using this concept.

1.1.2 Modification of the critical state model

The critical state model described above, incorporating Hvorslev and Roscoe surfaces, has been shown to inadequately model certain geomaterials, especially in the Hvorslev region (Byerlee, 1967; Cuss, 1999; Hudson and Harrison, 1997; Maltman, 1994; Ohnaka, 1973; Schofield, 1998; Wong *et al*., 1997). This is primarily due to the complications introduced by lithification and general rock-forming processes. Some researchers have chosen to replace the state boundary surfaces by more general failure criteria, which may be either theoretical (mathematically derived) or empirical (experimentally derived). It can be argued that the empirical approach is more appropriate and useful, however calibration demands accurate deformation data under known conditions that may not exist or be prohibitively expensive to obtain.

Many failure criteria exist that can be used to modify the critical state model. On the “dry side”, the Grittith-type, modified Griffith-type (McLintock & Walsh, 1962), Hoek-Brown (Hoek & Brown, 1980), Mohr-Coulomb, non-linear Mohr-Coulomb, or Khan empirical failure (Wong *et al.*, 1997) can be used to modify the no-tension and Hvorslev regions. Fewer options are available for the "wet side". The empirical elliptical cap model of DiMaggio & Sandler (1971) has been successfully applied to porous sandstone by Teng-fong Wong and co-workers (Wong *et al.*, 1997; Zhu *et al.*, 1997; Zhu & Wong, 1997[a,b]) and by others (Cuss, 1999; Cuss *et al.*, 2003).

1.1.3 Critical state model for argillaceous materials

Figure 1-3 summarises the features observed for shale deformation in terms of the critical state model and the dilatancy boundary. This data is presented in the p' - q' space, but could easily be expanded into the p' - q' - v critical state space.

Within the domain below the state boundary surface, permeability and porosity reduction is essentially independent of deviatoric stress (Zhu & Wong, 1997[b]). Prior to yield, porosity reduction will be elastic as pore space reduces as grains elastically deform. Porosity will also reduce as pre-existing damage (i.e. fractures) elastically close.

On the dry side, stresses above the idealised Hvorslev-type surface are achievable due to the strength of lithified shale. Brittle failure occurs at a deviator given by a brittle failure criterion, e.g. the Hoek-Brown failure criterion, and deformation progresses towards the idealised Hvorslev-type surface, which corresponds to the residual strength envelope. Considerable dilatancy is observed during this stage of deformation as a shear fracture is formed in shale. The further ‘left’ of the dilatancy boundary, i.e. at low effective mean stresses, the more dilatant deformation is. Critical state mechanics shows that further deformation progresses towards the critical state where deformation is isovolumetric. During this progression, shale work hardens as the further granulation of material within the shear band becomes more difficult to disaggregate. Dilatancy hardening may also be present under undrained conditions. The reduction in porosity along the fracture leads to a significant reduction in permeability (a self sealing process). Permeability will reach a minimum at the critical state.

On the wet side, deformation always results in contractancy of the bulk material. This leads to a reduction in porosity by the processes of compaction/consolidation and cataclasis. Intracrystalline plasticity may also contribute to a lowering of porosity. This results in a reduction in permeability, which further reduces as deformation progresses up the Roscoe-type surface towards the critical state. The further ‘right’ of the dilatancy boundary, i.e. at high effective mean stresses, the more contractive deformation is and the higher the degree of permeability reduction. The extreme case is the stress-path that coincides with the NCL. Here plastic volumetric strains are largest and the decline in permeability is most marked.

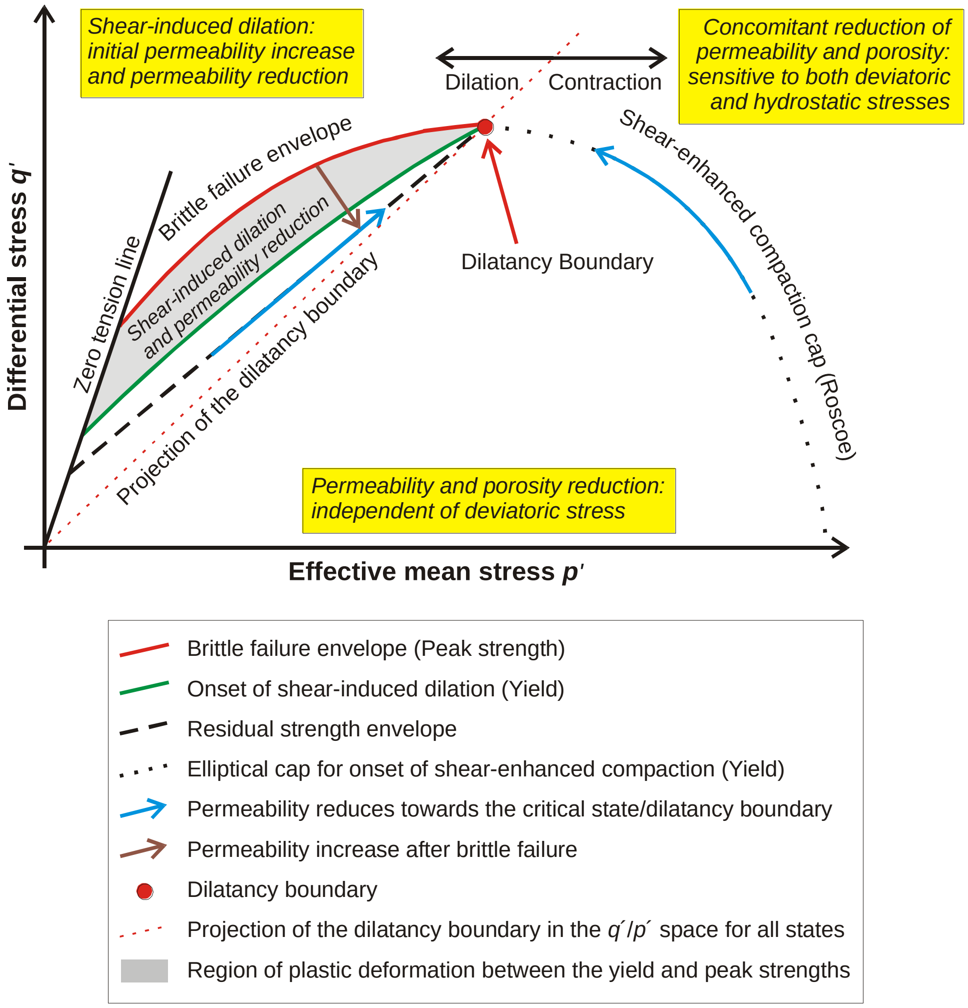

Figure 1-3 The role of the dilatancy boundary in shale sealing as shown in the p′ - q′ space. Modified from Zhu & Wong (1997^{b}).

A thorough knowledge of the dilatancy boundary is required in order to predict the likely mode of deformation and forecast the effect of deformation on the capacity of the rock to impede fluid movement.

It can be seen that the disposal of waste in a geological repository is favourable under “wet” conditions. As long as pore-pressure is not raised, which would lower effective mean stress, induced deformation under these conditions will result in a more effective self-sealing of discontinuities such as faults and fractures. The construction of a waste site will inevitably alter the local stress field, and as rocks at depth can be viewed as approaching a state of limiting equilibrium[2], deformation and yield are likely. Since permeability enhancement by dilation can be ruled out in "wet side" sediments, deformation and yield of these host materials will pose no special problems in the context of fluid flow and radionuclide transport.

Lithified shale at shallow depths is over-consolidated, and thus deformation will tend to be on the "dry side". There seems little doubt that shales that lie substantially to the left of the dilatancy boundary, will be subject to strong dilation and permeability enhancement during repository development or disturbance by external factors such as seismicity. Self-sealing may no longer be effective in rocks which are heavily over-consolidated and prone to shear-dilatancy.

1.2 DEFORMATION AND TRANSPORT PROPERTIES

The following section briefly summarises the evidence for transport property change during deformation. Considerable work has been conducted on the porosity and permeability evolution of sediments with simple hydrostatic load, i.e. simulating increasing burial depth. Many studies have also been conducted on how permeability changes during the triaxial deformation of samples.

The permeability of any one formation is variable because it can change with corresponding changes in boundary conditions, for example stress or deformation (Heiland, 2003). Therefore, a thorough knowledge is required of how permeability changes with stress and orientation.

In the case of underground waste disposal, the permeability of the rock mass surrounding the repository should be as small as possible. As the deformation induced during the construction of the EDZ is known to enhance permeability, research has tended to focus on looking at permeability variations associated with EDZ development. In the case of argillaceous rocks, we are interested in both the onset of dilatancy and the way in which fractures alter the hydromechanical behaviour of the EDZ.

Considerable work has also been conducted on permeability evolution by the hydrocarbons industry. As many rocks obey the law of effective stress, the lowering of reservoir pore-pressures during reservoir depletion results in an increased effective stress. If a sufficient change in stress occurs, the reservoir rocks can start to compact, and this in turn will reduce permeability. Usually it is assumed that the rock mass is subject to uniaxial strain conditions during reservoir depletion, which means that only vertical compaction occurs due to increasing effective vertical stresses, and that lateral deformation is zero (Schutjens & de Ruig, 1997). However, stress measurements have shown that a reservoir can undergo different stress-paths, depending on the boundary conditions, geometry and the poroelastic properties of the rock (Heiland, 2003).

The permeability of rocks has been widely reported under hydrostatic stress conditions (e.g. Zoback & Byerlee 1975; Walsh & Brace 1984; Morrow *et al.*, 1984; David *et al.*, 1994; Dewhurst *et al.*, 1999[a,b]; Katsube, 2000; Katsube *et al.*, 1996[a,b]; Kwon *et al.*, 2001; Neuzil *et al.*, 1984) in order to establish the relationship between effective stress and permeability for different rock types. However, in the field, rocks are normally subjected to an inhomogeneous stress-field, where the vertical stress (determined by the weight of the overburden) exceeds the two horizontal stresses (Holt, 1990). This has led to investigations of the sensitivity of matrix permeability to non-hydrostatic stress conditions, especially in sandstones (e.g. Keaney *et al.*, 1998; Zhu & Wong, 1994; Zhu & Wong, 1997[a,b]).

Volumetric deformation of shale on the 'dry side' (brittle field) is complex. Figure 1-4 shows the volumetric strain for a sample of North Sea shale (from Remvik & Skalle, 1993). As the sample contracts in the elastic phase, the pore-pressure increases. At or around the onset of yield (point of initiation of permanent deformation), contraction behaviour stabilises, and by the peak

---

[2] In many regions, the upper crust is subject to shear stresses approaching the frictional strength of favourably orientated faults (Engelder, 1993). This results in a state of limiting equilibrium within the crust with everywhere at the point of failure according to Byerlee's rule.

strength, shale has initiated dilatant deformation. In undrained conditions, a pore-pressure maximum is observed. Plastic volumetric strain starts to dilate around the peak of the total volumetric strain curve; this increase in microcrack porosity explains why the pore-pressure decreases.

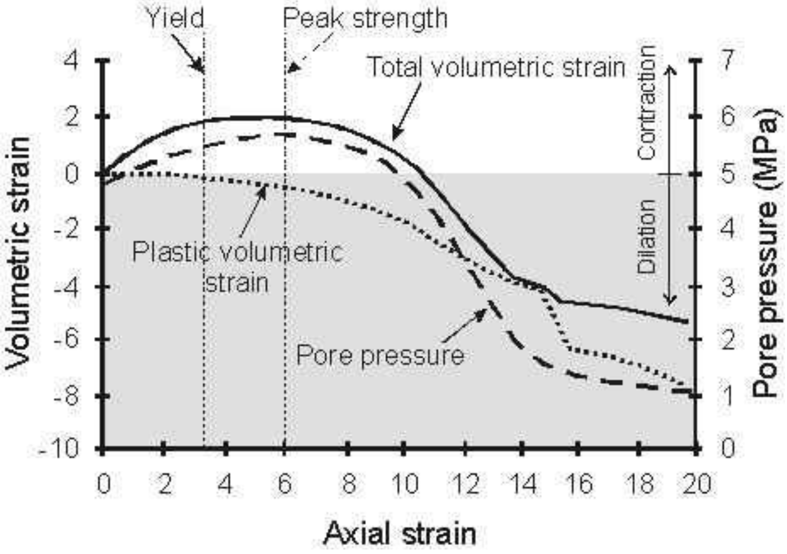

Figure 1-4 Total and plastic volumetric strain for North Sea shale during ‘dry’ deformation (modified from Remvik & Skalle, 1993).

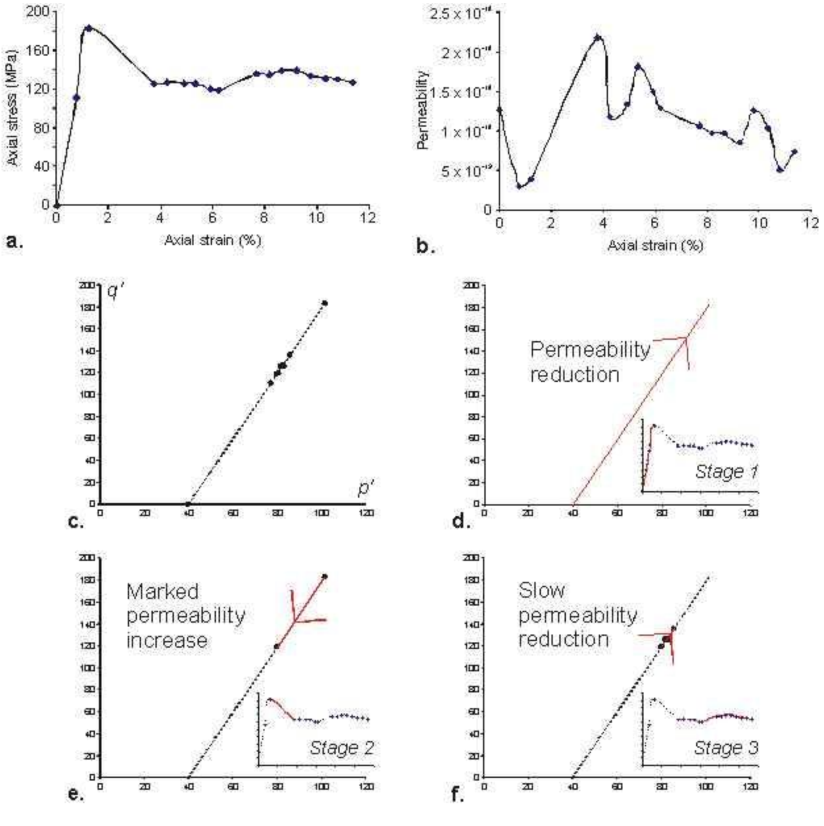

Figure 1-5 Evolution of permeability in Tennessee sandstone during brittle fracture: a) stress-strain result, b) permeability-strain result, c) the stress-path taken during deformation, note that a straight line is the result as the pore-pressure is kept constant, d) – f) permeability observations during the different stages of brittle deformation. Data from Keaney *et al.* (1998).

The work of Keaney *et al.* (1998) illustrates the complex evolution of porosity and permeability (Figure 1-5) during brittle fracturing in a drained system. During the elastic stage of deformation, porosity and permeability decrease due to the elastic closure of pre-existing fractures and the poroelastic response. At about 1% axial strain, dilatant volume increase is initiated as new fractures are formed. After about 1.5% axial strain, the net volume of the sample is less than when first tested. At the peak stress level, deformation is concentrated into a fracture by the process of shear localisation. During the stress drop, permeability is markedly increased as the stress level equilibrates to the residual strength of the material. As deformation continues at the residual strength, the permeability reduces. Porosity continues to increase slowly. Strain hardening and experimental artefacts may contribute to this observation, but it is clear that permeability does decrease as the localised fracture develops.

These observations show that permeability both decreases and increases in the brittle regime. This can be explained microstructurally by observing what happens at the different stages of shear localisation. Several workers have described the microstructural evolution of different sandstone types during deformation (Cuss, 1999; Cuss *et al*., 2003; Menéndez *et al*., 1996). With the application of axial load within the elastic region, porosity closes preferentially in the axial direction, resulting in the formation of axial impingement fractures between point contacts. Porosity increases and tortuosity decreases as these fractures open, resulting in an increase in material permeability. Damage concentrates into a band angled at 30° to the axial load. Further deformation is concentrated within the shear band; no deformation is observed away from this feature. As strain increases at the residual strength, the central shear zone broadens and the gouge material becomes finer grained. The reduction in grain size and associated compaction within the shear band creates an effective barrier, reducing the bulk permeability of the test sample, as described by Keaney *et al*. (1998). Although this work, and work by Zhu & Wong (1997), has been conducted on sandstones, it represents the best data available for permeability changes during deformation.

1.3 STRESS-PATHS DURING TUNNELLING

The construction of a gallery within pre-stressed rock will result in some form of stress concentration that will in turn result in deformation. The transient nature of tunnel construction will play a significant role in that deformation, as will the method of construction. Tunnel construction is slow compared to the transient (creep) properties of rock, so the way in which the gallery face progresses will influence subsequent deformation. As deformation at the face will occur, other physical properties, such as pore-pressure, will also change before the face is completed. Hence it is vital to consider the transient changes in stress during construction and analyse how these influence deformation. Stress-path modelling of tunnels has become common practice. This requires careful stress-path experiments as well as stress-path analysis of models. A comprehensive review of stress-paths and tunnels is given by Barla (1999).

Finite element analysis of an elasto-plastic medium was conducted by Ng & Lo (1985) in order to determine the stress-path at three typical points around a tunnel. These points corresponded to the tunnel roof or crown, the sidewall, and a point half way between the two. This enables a continuous stress-path to be determined for the entire tunnel, with 45° between estimates. Figure 1-6 shows the result of this study, with a K_0 = 0.75 condition and the excavation process simulated by reducing the initial stresses. The study shows that the tunnel wall has a significant stress-path history. Steiner (1992) showed that the shape of the tunnel plays a significant role on the resulting stress-path.

Bellwald (1990) and Aristorenas (1992) examined the effective stress-path around a tunnel by means of theoretical considerations and showed there are two clear phases of the stress-path:

1. The first is created during the tunnel excavation,
2. The second phase occurs after excavation and is a drained phase when the negative excess pore-pressure dissipates.

The construction of a tunnel into material that may undergo swelling will alter the stress-path and needs to be incorporated into coupled models. This was addressed by Anagnostou (1991), who interpreted the time-dependent development of swelling strain as a consequence of the dissipation of negative pore-pressure. Tunnel geometry change will occur slowly and will change the stress-path as plastic deformation occurs.

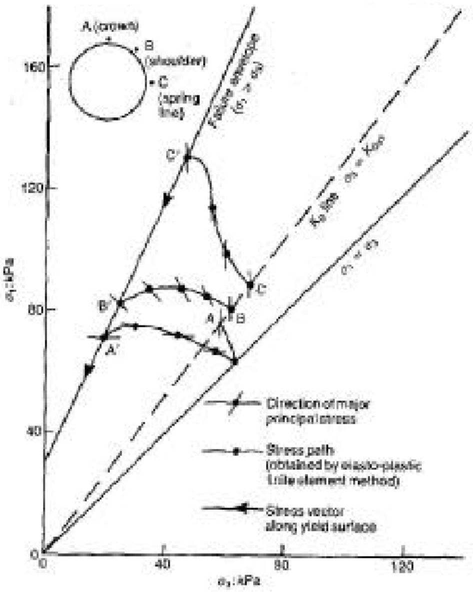

Figure 1-6 Stress-paths for typical elements in soil due to tunnelling (Ng & Lo 1985; taken from Barla, 1999).

1.3.1 Stress-paths during face advancement: 3-D Elastic Stress-paths

The work of Barla and co-workers at the Politecnico di Torino, Italy (G. Barla, M. Barla, M. Bonini) gives a useful account of stress-paths created by an advancing excavation in rock (Barla, 1999, 2001; Barla & Barla, 2001; Bonini *et al.*, 2001). This work was carried out by numerical analysis using finite difference element modelling (Flac and Flac3D: Itasca, 1996) and boundary element modelling (Examine3D: Rocsicience, 1998). The study modelled stress-paths at the sidewalls (S) and at the crown/invert (C).

The stress states at points C and S depend on the depth of cover and the stress ratio (minimum to maximum principal stress ratio, K_0) prior to excavation. The tunnel face advances during excavation and continues to completion of excavation. The Torino study considered two different stress conditions, depending on the K_0 ratio. For each case, two-dimensional and three-dimensional analyses were performed and the results compared with the closed form solutions available.

The numerical results (Figure 1-7) show a significant difference between the stresses computed for three-dimensional and two-dimensional conditions, with clear implications for understanding the stress-path around the tunnel. It is evident that the stress history, particularly near the tunnel face, can only be properly described by simulating three-dimensional conditions (Bonini *et al.*, 2001).

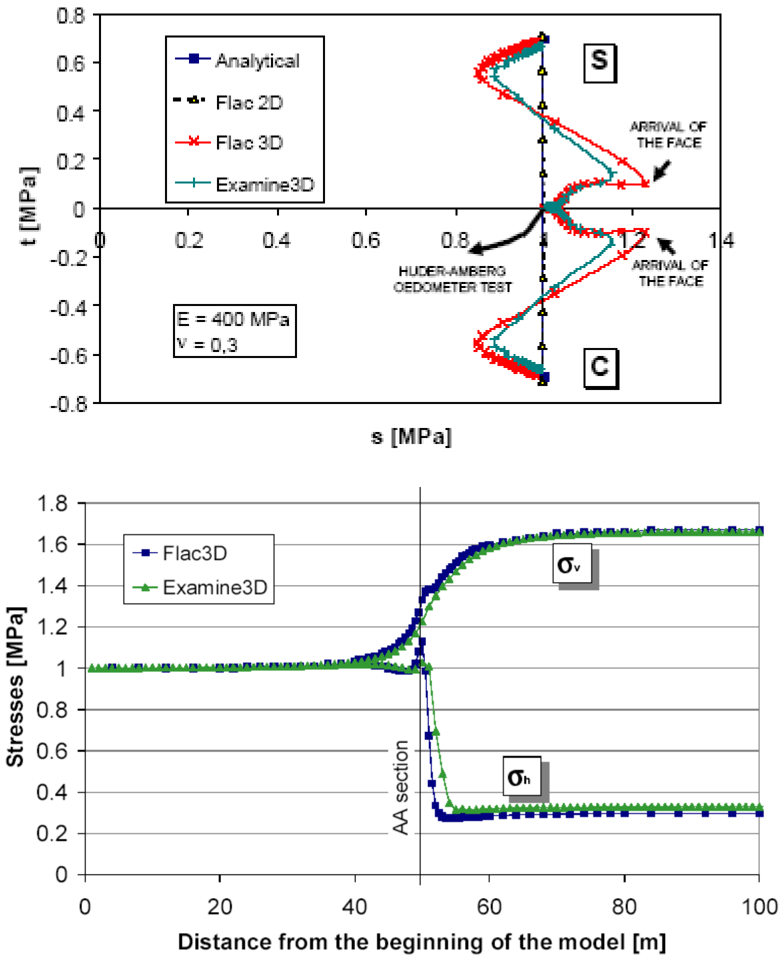

a).

b).

Figure 1-7 (a) Stress-paths for points S (sidewalls) and C (crown/invert) for the elastic K_0 = 1 analyses. (b) Vertical and horizontal stresses at point S in the sidewalls for the 3D elastic K_0 = 1 analysis (from Bonini *et al.*, 2001).

1.3.2 Stress-paths during face advancement: 3-D elastoplastic stress-paths

Barla *et al.* (Barla, 1999, 2001; Barla & Barla, 2001; Bonini *et al.*, 2001) modelled the system as elastoplastic with strain-softening. A limit value (ε_1) for the axial strain (ε) was defined below which the peak strength parameters (τ_o = cohesion, ϕ = friction angle) apply. For values of ε greater than ε_1, the strength parameters are taken to change linearly down to the residual strength parameters (c_r, ϕ_r), which hold true for greater than the limit value ε_2 (Barla, 1999).

During the simulation, strength is exceeded and plastic deformation occurs around the tunnel. When K_0 = 1, the stress initially increases and then decreases strongly with distance from the beginning of the model at both points S and C, as shown for S in Figure 1-8. The decrease in stress initiates when the excavation face is still 5 to 6 metres away from the monitored section, A-A. This analysis shows that a plastic zone is created around the tunnel during excavation. When the deformation resulting from the stresses changes from elastic to plastic behaviour, both the vertical and horizontal stresses decrease to a small value and determine the decrease of σ. This occurs as soon as the plastic zone gets through the A-A section. After this point, there is very little change in the state of stress.

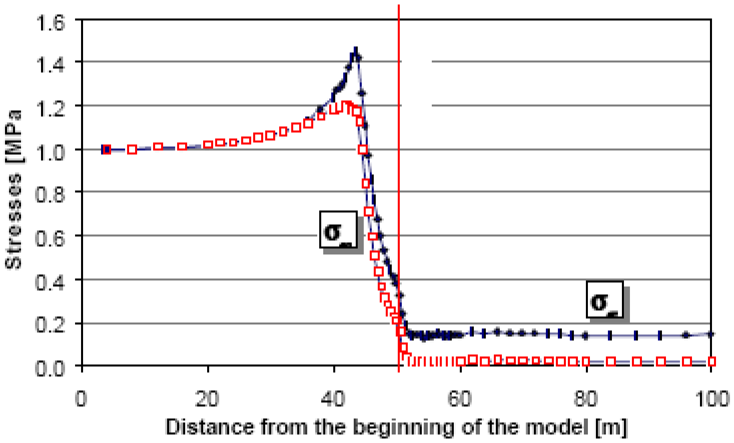

Figure 1-8 Stresses at point S (sidewall) for the 3D elastoplastic K_0 = 1 analysis (from Barla, 1999).

1.3.3 Conclusions of stress-paths

The work summarised above shows that stress-paths are highly complex during the construction of a repository tunnel. Wall rock will undergo large changes in stress as the tunnel advances, and with the addition of time-dependent deformation, further stress-path changes will occur while the tunnel is open. Long-term convergence will result in a further modification of the stress-path. Therefore, it is essential to understand the effect the changing stress-path has on the physical and transport properties of the Callovo-Oxfordian claystone.

1.4 GAS FLOW

In a geological disposal facility (GDF) for radioactive waste, corrosion of ferrous materials under anoxic conditions combined with the radioactive decay of the waste and the radiolysis of water, will lead to the formation of hydrogen. A full understanding of the migration behaviour of this gas is of fundamental importance to the development of the GDF. If the rate of gas production exceeds the rate of gas diffusion within the pores of the barrier or host rock, a discrete gas phase will form (Weetjens & Sillen, 2006; Ortiz *et al*., 2002; Wikramaratna *et al*., 1993). If this occurs, capillary restrictions (Aziz & Settari, 1979) on the movement of gas will result in the build-up of pressure to a critical value when pressure becomes sufficiently large for it to enter the surrounding material and move through advective processes.

To accurately predict the movement of gas through argillaceous materials (Neretnieks, 1984; Kreis, 1991; Askarieh *et al*., 2000; Ekeroth *et al*., 2006; Smart *et al*., 2006), it is first necessary to define the correct conceptual model that best represents the empirical data. In a clay-based GDF four primary phenomenological models can be defined to describe gas flow as proposed by Marschall *et al*. (2005; Figure 1-9):

(i) Gas movement by solution and/or diffusion governed by Henry's and Fick's Laws respectively within interstitial fluids along prevailing hydraulic gradients;

(ii) Gas flow in the original porosity of the fabric governed by a generalised form of Darcy's Law, commonly referred to visco-capillary (or 2-phase) flow;

(iii) Gas flow along localised dilatant pathways (micro-fissuring), which may or may not interact with the continuum stress field, the permeability of which is dependent on an interplay between local gas pressure and the effective stress state; and

(iv) gas flow along macro fractures similar in form to those observed in hydrofracture activities during reservoir stimulation, where fracture initiation occurs when the gas pressure exceeds the sum of the minor principle stress and tensile strength.

For engineering problems such as radioactive waste disposal, underground gas storage and carbon dioxide sequestration, most interest is focussed on understanding the processes and mechanisms governing the advective transport of gas (mechanisms ii through iv).

There is now a growing body of evidence (Angeli *et al*., 2009; Harrington & Horseman, 1999; Horseman *et al*., 1996, 2004; Harrington *et al*., 2009, 2012) that in the case of plastic clays and in particular bentonite, classic concepts of porous medium two-phase flow are inappropriate. Flow through dilatant pathways has been shown in a number of argillaceous materials (Angeli *et al*., 2009; Autio *et al*., 2006; Gallé & Tanai, 1998; Harington & Horseman, 1994, 1997, 1999; Horseman *et al*., 1999; Ortiz *et al*., 1996, 2002). The pathways are pressure-induced and their aperture is a function of their internal gas pressure and structural constraints within the clay. However, the exact mechanisms controlling gas entry, flow and pathway sealing in clay-rich media are not fully understood and the "memory" of such pathways could impair barrier performance.

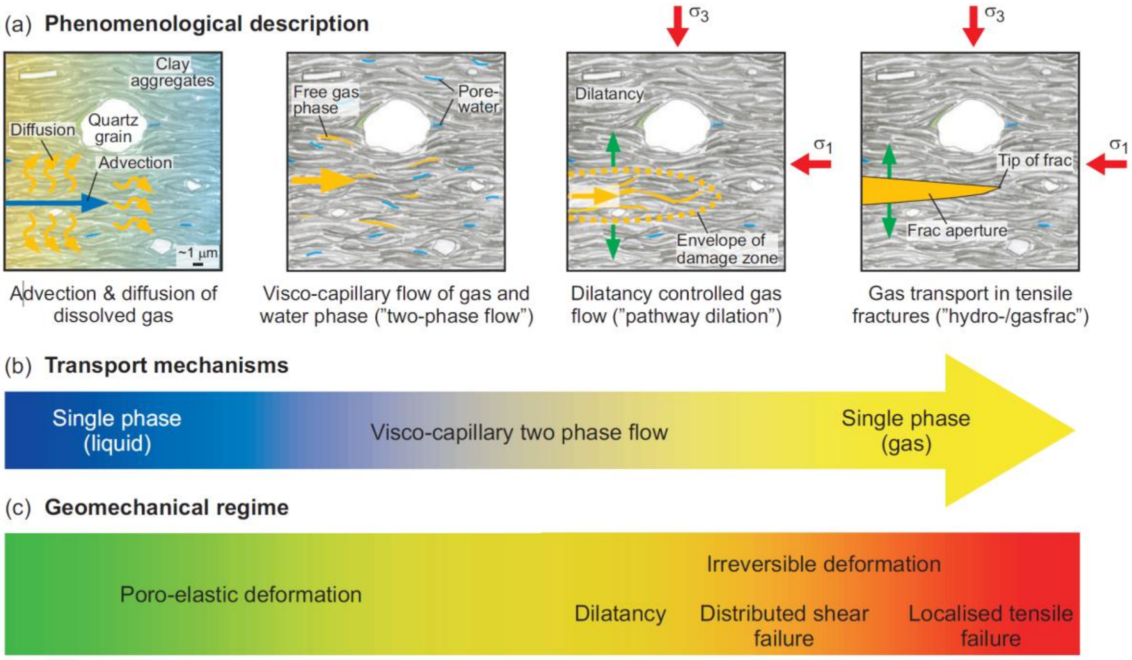

Figure 1-9 Classification and analysis of gas transport processes in clays (after Marschall *et al*., 2005). a) phenomenological description based on the microstructural model concept; (i) diffusion and/or solution within interstitial water; (ii) visco-capillary (or 2-phase) flow in the original porosity of the fabric; (iii) flow along localised dilatant pathways (micro-fissuring); and (iv) gas fracturing of the rock; b) basic transport mechanisms; and c) geomechanical regime.

1.5 THE CONCEPT OF EFFECTIVE STRESS

An important aspect of the critical state theory of soil mechanics of the concept of effective stress. The experimental setup used allows a study to be conducted of effective stress in COx as pore-pressure is measured in four distinct locations within the test sample. Therefore a study of effective stress became a secondary focus of attention in the experimental programme.

The introduction of pore-fluid under pressure has a profound effect on the physical properties of porous solids (Hubbert & Rubey, 1959; Terzaghi, 1943). In a saturated porous system, the fluid supports some proportion of the applied load, creating fluid-pressure, which acts in the opposite direction to the load, lowering the overall stress exerted through grains. The addition of fluid pressure lowers available stress by an amount that is proportional to the pore-pressure. Therefore the law of effective stress states:

$$\sigma' = \sigma - u$$

where σ' is effective stress, σ is total stress, and u is pore-pressure. Strength is determined not by confining pressure alone, but by the difference between confining and pore-pressures. In simple drained tests, pore-pressure remains constant at atmospheric pressure and the observed effective stress is similar to the applied load. Conversely, if the pore-fluid system is closed, pore-pressure rises in proportion to the applied load as pore space is reduced, significantly lowering the overall effective stress. Thus, the mechanical response of rocks to applied load is significantly affected by the ability of fluids to drain.

Many rocks have been shown to follow the law of effective stress, including shale (Handin *et al*., 1963; Kwon *et al*., 2001) and sandstone (Byerlee, 1975; Cuss, 1999). However, due to the compressibility of clay and the poroelastic effect (after Biot, 1941), where the effective stress is modified by the partial transfer of pore-pressure to the granular framework, the law of effective stress is modified with the effective pressure coefficient (χ):

$$\sigma' = \sigma - \chi\, u$$

Kwon *et al*. (2001) showed that the effective pressure coefficient χ was equal to 0.99 ± 0.06 for Wilcox shale. This value is indistinguishable from unity and demonstrates that the law of effective stress is obeyed in this particular shale variety. Burrus (1998) showed that χ much less than unity was appropriate for shale for the Mahakam Delta ($\chi = 0.65 – 0.85$).

Conceptual models of argillaceous rock deformation, such as critical state soil mechanics (Schofield & Wroth, 1968; Atkinson & Bransby, 1978; Wood, 1990), use the law of effective stress. Therefore careful experimentation has to be undertaken to account for drainage effects and to determine the role that pore-pressure has on the deformation of sediments.

2 Experimental geometry

2.1 TEST MATERIAL

The composition of the Callovo-Oxfordian claystone (150-160 Ma) can be divided in to three main constituents; clay, silt and carbonate. Wenk *et al.* (2008) reports these constituents (at the Bure site) as follows; clay 25-55 wt%, 23-44% carbonates and 20-31% silt (essentially quartz + feldspar). Clay minerals are reported to include illite and illite-smectite with subordinate kaolinite and chlorite. In the upper half of the formation the illite-smectite is disordered and contains 50-70% smectite interlayers, whilst in the lower half the illite-smectite is ordered (R=1 type) with lower contents (20-40%) of smectite interlayers (Wenk *et al.*, 2008). Beds can contain common organic matter.

Other authors report compositions similar to these. Wileveau & Bernier (2008) quote values for quartz (18%), calcite (25%), clay minerals (55%; illite-smectite ~65%, illite 30%) and kaolinite and chlorite (2%) with subordinate feldspars, pyrite and iron oxides (2%). Esteban *et al.* (2006) report 35-60% clay minerals with the remaining shared by calcite and silt. Gaucher *et al.* (2004) includes highly detailed mineralogical and chemical compositions of the sequence which are again in broad agreement with the above compositions.

The claystone was deposited under marine basin conditions during a period in which the Paris Basin was variously linked to the Atlantic and Tethyan Oceans, as well as to the London Basin and North Sea (Rousset & Clauer, 2003). Clay sedimentation is therefore considered to have two primary inputs; continental and oceanic. The claystone is over- and underlain by Oxfordian and Bathonian shelf limestones. It is primarily clayey at its base, then becomes increasingly silty and then increasingly calcareous at its top (Gaucher *et al.*, 2004). A maximum clay content zone within the clayey base has been identified; this is interpreted to mark the inflection point (and interval of maximum flooding) from a lower transgressive sequence to an upper regressive sequence (Gaucher *et al.*, 2004).

Upon receipt of the preserved T1-cell core barrels at BGS, the material was catalogued and stored under refrigerated conditions of 4°C (to minimise biological and chemical degradation) ready for future testing. The core material is delivered with a rubber material around the COx sample, surrounded by a cement material with a plastic outer jacketing material, as seen in Figure 2-1a. Each T1-cell contains approximately 300mm of core, enough for three finished samples. The core barrel was cut into three (approximately 100mm length) using a dry-cut diamond encrusted bladed saw (see Figure 2-1b).

2.1.1 Production of sample SPP_COx-1 using diamond coring

The production of samples at least 75mm length and 56mm diameter proved difficult during preparation of sample SPP_COx-1. The dry-cutting of the core barrels proved problematic as the blade tends to bind and snag in the hard cement material used to pack the barrel. This results in damage to the sample material, as seen in Figure 2-1c. In order to reduce this problem the packing material was removed prior to cutting to 100m length samples.

The core material was sub-sampled to 56mm diameter and approximately 75mm length using a combination of dry core-drilling (with gas flushing and vacuum removal of fines, as shown in Figure 2-1d) and diamond slicing. Core drilling was also problematic as the samples contained a number of weaknesses (micro-fractures and fossils) that resulted in the samples splitting along their length, as seen in Figure 2-2. One sample was successfully cored and was finished by trimming on a lathe to get a good even surface finish and the sample ends were ground flat and parallel to minimise “end-effects” during testing. The specimen was accurately measured using a digital micrometer and weighed. Off-cuts from the coring process were weighed and oven dried to obtain an estimate of moisture content. The dimensions and provisional geotechnical properties of the specimen are given in Table 2-1.

Figure 2-1 Sample preparation. (a) The core samples are delivered with the COx material encased in a thin rubber material, surrounded by a cement material, and the outside of the core barrel is a plastic material. (b) The 300mm length core barrel was sub-sampled into 100mm length by dry cutting using a diamond encrusted blade. (c) Damage caused to the COx core as the dry cutting blade “sticks” while cutting the hard cement packing material. (d) Dry diamond coring of a 100mm length of COx core material. (e) Finished sample of COx.

Sample SPP_COx-1 was cut parallel to the bedding, and was taken from drilling core EST30340, dated 30/10/08 from location OH2, T cell T1.1112, drilling interval 30.17m to 30.49m. The torque applied to the axial confining system of the T1-cell was around 18 Nm.

2.1.2 Production of sample SPP_COx-2 using machine lathing

Following the problems reported above for sample SPP_COx-1, a modified methodology was employed for sample SPP_COx-2. A 100m section of complete core was placed in a lathe and slowly trimmed to a diameter of 56mm to get a good even surface finish and the sample ends were ground flat and parallel to minimise “end-effects” during testing. The specimen was accurately measured using a digital micrometer and weighed. Off-cuts from the coring process were weighed and oven dried to obtain an estimate of moisture content. The dimensions and provisional geotechnical properties of the specimen are given in Table 2-1.

Sample SPP_COx-2 was cut parallel to the bedding, and was taken from drilling core EST30341, dated 30/10/08 from borehole OHZ1201, T cell T1.1111, drilling interval 30.49m to 30.80m. The torque applied to the axial confining system of the T1-cell was around 18 Nm. Test sample SPP_COx-2 was from the adjacent core barrel as test sample SPP_COx-1.

Figure 2-2 A sample of COx that split lengthwise while being diamond cored. As can be seen, the core split revealing a fossil within the core (see right). Two samples split lengthwise during sample preparation.

2.2 BASIC PHYSICAL PROPERTIES

The starting sample was measured five times for length and nine times for diameter. The sample was weighed, which allowed bulk density to be determined. Table 2-1 shows the pre-test physical properties of the specimens based on the moisture content of the off-cuts and a grain density of 2.70 Mg m^{-3} (Zhang *et al.*, 2007). The data presented in Table 2-1 is in good agreement between samples and with the generic values quoted by Zhang *et al*.

	Units	Value	Value
Sample reference		SPP_CoX-1	SPP_COx-2
Location		Bure URL, France	Bure URL, France
Borehole / drill core		OHZ1201 / EST30340	OHZ1201 / EST30341
Core direction		Parallel to bedding	Parallel to bedding
Average length	mm	76.63 ± 0.02	82.45 ± 0.03
Average diameter	mm	55.50 ± 0.01	55.85 ± 0.04
Volume	m^3	1.854×10^{-4}	2.020×10^{-4}
Average weight	g	455.6	495.02
Density	$g.cc^{-1}$	2.458	2.451
Grain density	$g.cc^{-1}$	2.7	2.7
Moisture weight	g	24.6	28.7
Moisture content	%	5.7	6.2
Dry weight	g	431	466
Dry density	$g.cc^{-1}$	2.33	2.31
Void ratio		0.166	0.174
Porosity	%	14.2	14.8
Saturation	%	93	96

Table 2-1 Dimensions and basic properties of the Callovo-Oxfordian claystone test material (samples SPP_COx-1 and SPP_COx-2) from pre-test measurements of water content from off-cut material adjacent to the core. An assumed specific gravity for the mineral phases of 2.70 $Mg.m^{-3}$ (Zhang *et al.* 2007) was used in these calculations.

2.3 EXPERIMENTAL SET-UP

The stress-path permeameter (SPP) is an evolution of the elastimeter apparatus that has been shown to perform well (Horseman *et al.*, 2005) and was specifically designed to resolve very small volumetric (axial and radial) strains potentially associated with the onset of gas flow. A schematic of the SPP is shown in Figure 2-3, along with a photo in Figure 2-4. The SPP comprises 6 main components:

1) The specimen, surrounded by a modified flexible Hoek sleeve (Figure 2-6b) and main pressure vessel body.
2) Three dash pots (Figure 2-6c) that are mounted along the radial mid-plane of the sample which directly measure the radial strain of the sample. The dash pots are pressure balanced in order to reduce the force imposed upon the sample and to make sure the push-rods are not simply pushed out of the pressure vessel.
3) An axial load system comprising of an Enerpac single acting hydraulic ram (see Figure 2-4) pressurised by an ISCO-500 series D syringe pump. This is connected via an axial strain jig to a Global Digital Systems optical encoder for measuring linear displacement accurate to 0.003 mm. Miniture load cells are located at the piston ends to measure stress at the sample ends.

4) A confining pressure system using an ISCO-500 series D syringe pump and glycerol confining medium allowing radial strain measurements to be calculated through volume change.
5) A pore-pressure system comprising two ISCO-100 series D syringe pumps to create pore fluid pressure and monitor back-pressure. The injection media can be either water or gas (usually Helium).
6) A state-of-the-art custom designed data acquisition system facilitating the remote monitoring and control of all experimental parameters.

A cylindrical rock specimen was positioned between two stainless steel platens and jacketed in a flexible Hoek sleeve (Figure 2-6b) to exclude the confining fluid. The inlet and outlet zones for water flow to and from the specimen are provided by stainless-steel discs, nominally 20 mm in diameter and 3 mm depth. Guard-rings of 6mm thickness and 2 mm depth are located on the outer diameter of the platens, allowing pore-pressure to be measured in two locations on the faces of the sample.

The stainless steel load platens were in direct contact with the sample transmitting the axial force generated by the Enerpac ram directly to the specimen. Each platen had two ports facilitating flushing of the system and the removal of residual air prior to testing. Retaining collars and axial tie-rods locked the system components together to provide a rigid test rig, these were pre-tensioned at 300 Nm.

Axial displacement was measured using the GDS optical encoder connected to stainless steel push rods terminating a short distance behind the load-bearing face of each platen to minimise compliance effects. Data from the optical encoder was processed through a multiplexer to provide a continuous measure of axial strain. The confining system provided an indirect measurement of radial strain by monitoring changes in volume while porewater displacement was monitored via the back-pressure system.

Three pressure balanced dash-pots (Figure 2-6c) were located around the radial mid-plane of the specimen. Brass push-rods were in direct contact with the outer diameter of the Hoek sleeve. Three 10 × 10 mm brass plates were cemented to the outer edge of the Hoek sleeve (Figure 2-6b) in order to reduce the force the push-rods imposed on the sample surface. The push rods extended to the outside of the pressure vessel, where high precision LVDTs were used to measure the displacement of the sample diameter.

Each ISCO pump controller had an RS232 serial port that allowed volume and pressure data to be transmitted to an equivalent port of a 32-bit personal computer. A state-of-the-art data acquisition system was developed using National Instruments *LabVIEW*™ software. The system allowed both remote access to test parameters and control of all ISCO pumps via a LAN based telemetry link. The software prompted the pump controller and multiplexer unit to transmit data to the computer at pre-set time intervals. Data could be downloaded at any time without physical access to the laboratory, minimising thermal variations due to personnel working in the laboratory environment. The experimental rig was completed by a number of pressure sensors and thermocouples.

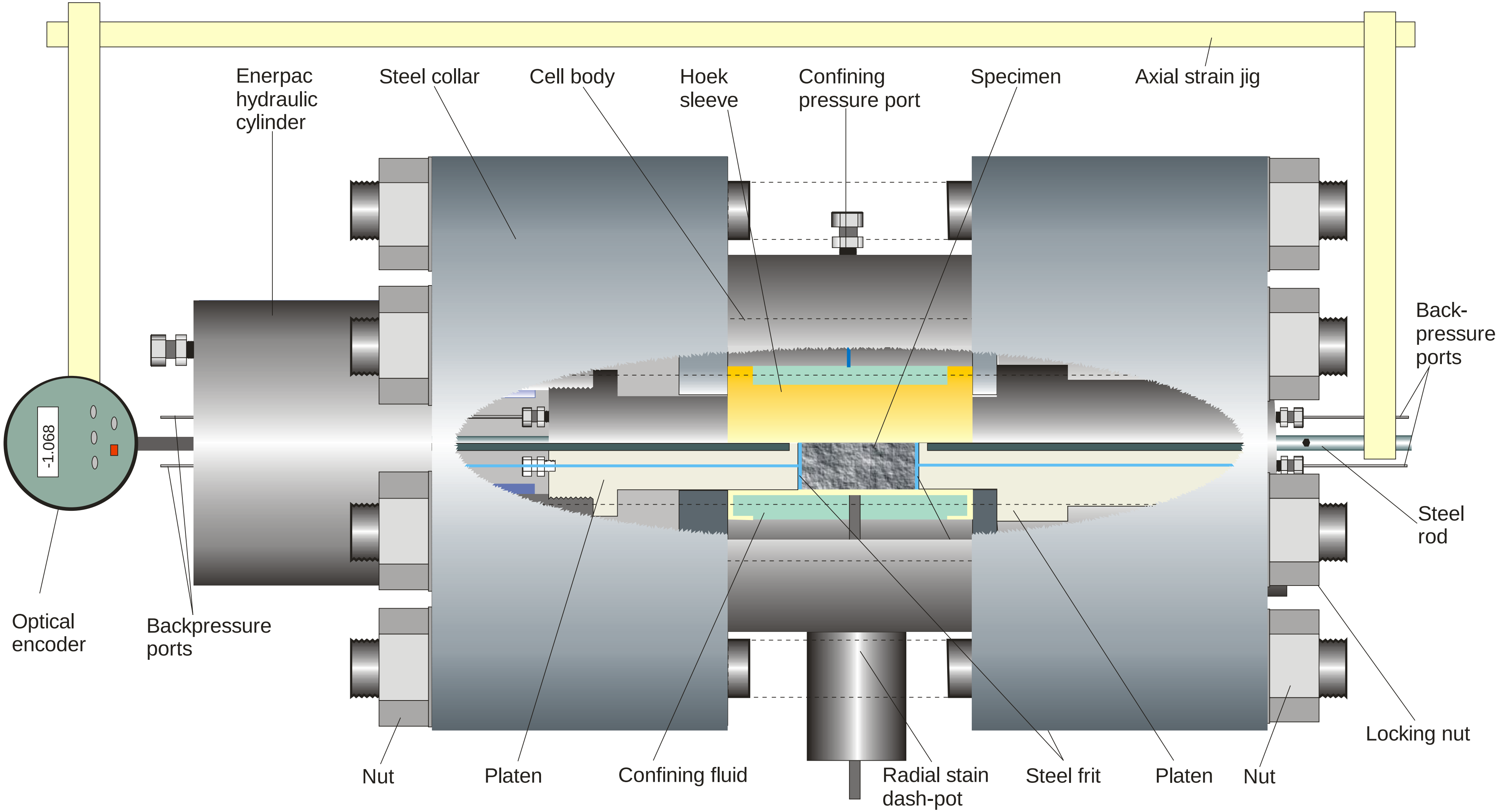

Figure 2-3 Schematic of the Stress-path Permeameter (SPP).

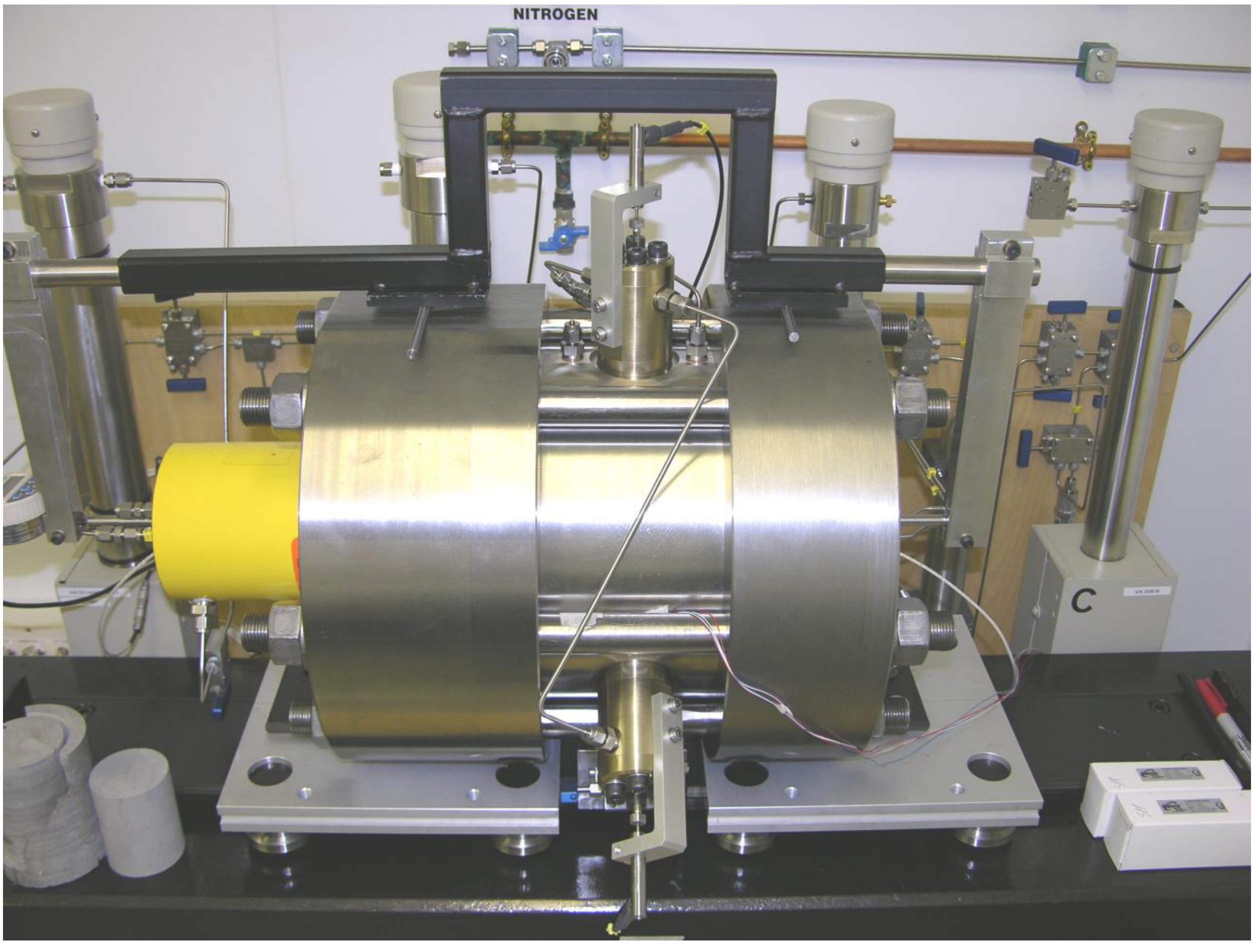

Figure 2-4 Photo of the SPP apparatus. The hydraulic ram (yellow) can be seen, along with the dash-pots used to measure radial deformation of the jacketed samples.

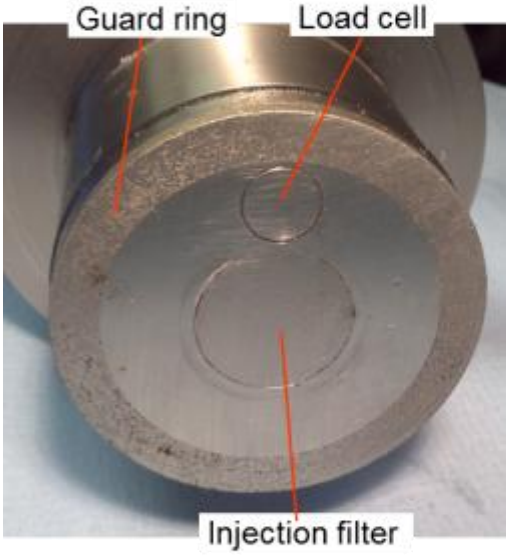

Figure 2-5 Photo of the end platen showing the injection filter and guard-ring arrangement.

One experimental uncertainty in transport testing is the short-circuiting of the flow system along the jacket of the test sample. The addition of a 6 mm wide, 2mm deep, porous stainless-steel annular filter along the outer edge of each platen (Figure 2-5) allowed pore-water pressure to be monitored and discount unwanted sidewall flow. These two guard-rings (Harrington *et al*., 2003) were each connected to a pressure transducer and the complete guard-ring system (filter, pipework and pressure sensor) was saturated with water and flushed in order to eliminate gas from the system. The inlet/outlet filter was made up of a porous disc 20 mm in diameter and 2 mm depth. The control board of the apparatus allowed the guard-rings to be either connected to the injection system to assist in hydration, or isolated to give an independent measure of pore-pressure. As well as being able to eliminate side-wall flow as a possible transport mechanism, the guard-rings meant pore-pressure was measured at four different points on the test sample (injection pressure, injection guard-ring pressure, back-pressure, back guard-ring pressure) providing data on the hydraulic anisotropy within the sample.

The SPP is able to conduct water and gas flow experiments under realistic *in situ* conditions. Tests can be conducted using a number of gases, although helium was used in the current test programme. For water flow experiments a chemically balanced synthetic pore fluid similar to that found at Bure was manufactured at BGS with the following composition: 227 mg.l^{-1} Ca^{2+}, 125 mg.l^{-1} Mg^{2+}, 1012 mg.l^{-1} Na^{+}, 35.7 mg.l^{-1} K^{+}, 1266 mg.l^{-1} SO$_4^{2-}$, 4.59 mg.l^{-1} Si, 9.83 mg.l^{-1} SiO$_2$, 13.5 mg.l^{-1} Sr, 423 mg.l^{-1} total S, and 0.941 mg.l^{-1} total Fe.

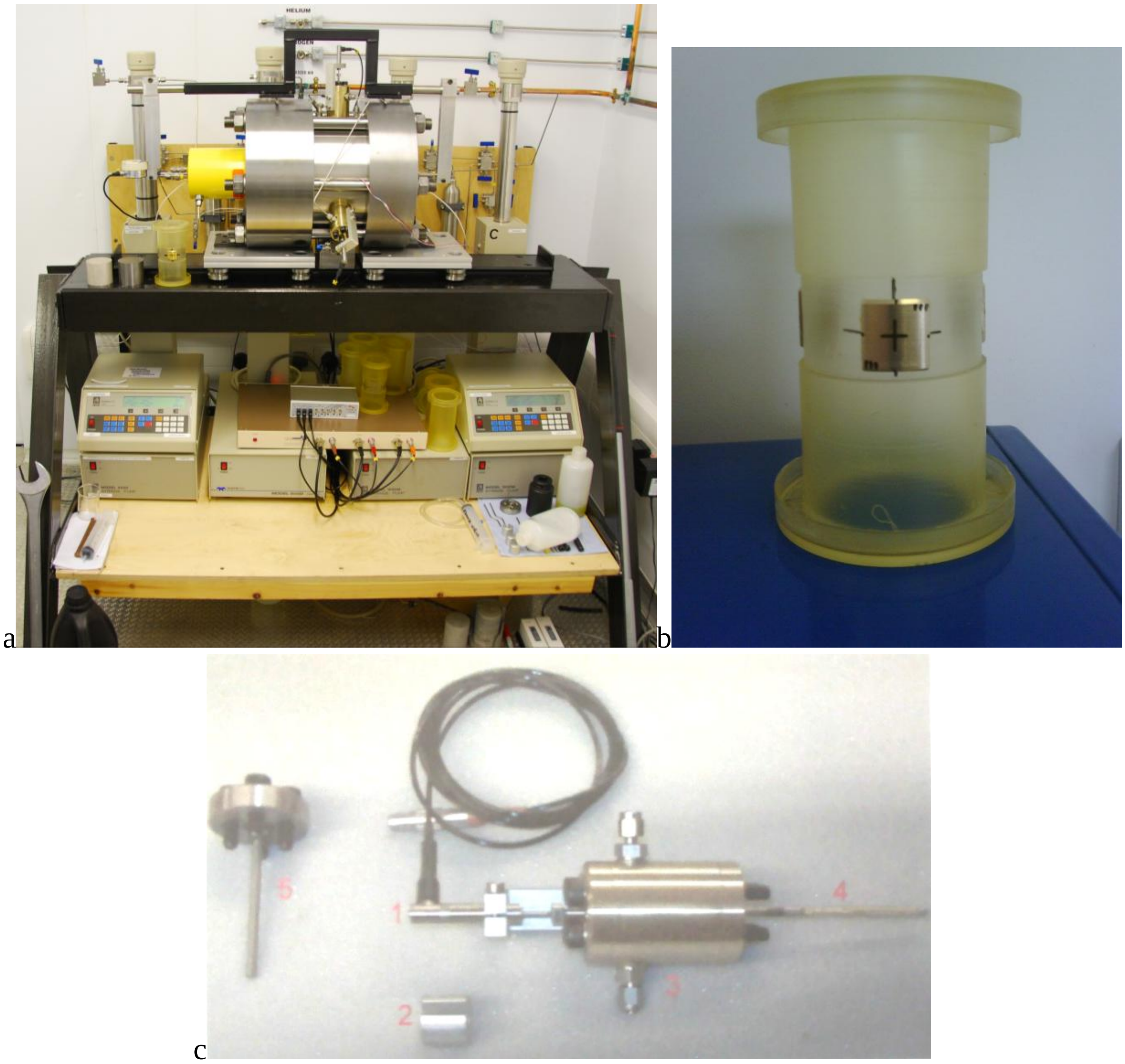

Figure 2-6 Components of the SPP. (a) The complete apparatus, showing the pressure vessel, pressure distribution board, four ISCO pumps [confining pressure, axial load, injection and back-pressure], and optical encoder box. (b) Modified Hoek sleve with brass additions that are in direct contact with the arms of the dash-pot arrangement. (c) Pressure balanced dash-pot system. The dashpot arm [4] is in direct contact with the outside of the sample jacket. The movement of this arm is recorded

by a high-precision LVDT [1]. The dashpot is pressure balanced through the pressure ports marked [3].

2.3.1 Measured parameters

The logging software directly recorded the following parameters every 2 minutes:

- SPP injection circuit pump (pressure, flow and volume)
- SPP back-pressure circuit pump (pressure, flow and volume)
- SPP axial load pump (pressure, flow and volume)
- SPP confining pressure pump (pressure, flow and volume)
- Load cell on the injection platen
- Load cell on the back-pressure platen
- Radial displacement of the sample mid-plane (Radial 1, Radial 2 & Radial 3)
- Axial displacement of the sample
- Temperature (vessel, laboratory low level and laboratory high level)

From the measured parameters, the following calculated parameters were determined:

- Axial strain of the sample
- Radial strain of the sample
- Volumetric strain of the sample
    - From direct measurements on the sample
    - From displacement of confining fluid
- Permeability and storage capacity
- Stress state

In addition to these parameters, physical properties were recorded prior to testing and on test completion.

2.4 CALIBRATION AND DATA ACQUISITION

A thorough set of calibration tests were undertaken in order to prove the SPP apparatus and to calibrate its systems, as described in Table 2-2.

Confining, injection, back-pressure and axial loading syringe pumps were calibrated using a Druck PTX610 pressure transmitter. Linear regression of data was undertaken to provide calibration values. In order to determine the axial load applied to the specimen through the surface of the platen at any given pump pressure, it was essential to accurately calibrate the ISCO pump used to pressurise the Enerpac ram. To minimise residual error between calibrated and measured values a second order polynomial fit was applied to the data. Calibration values were then multiplied by the ratio of surface areas between the ram piston and platen.

2.4.1 Testing for apparatus compliance

In order to try to assess the degree to which compliance of the apparatus might be affecting the results, the deformation of “standard” metal bars were measured within the apparatus under a series of applied axial and radial stresses (tests SPP_Cal07 & SPP_Cal09). Two materials were selected; 1) magnesium alloy, which is a relatively soft metal, and 2) tungsten, which is a very compliant metal. The magnesium alloy material was tested by the National Physics Laboratory to give accurate elastic constants for the reference material. The use of pure tungsten meant that reference elastic constants could be used.

Test number	Date	Sample	Description
SPP_Cal01	11/11/08	Mg	General testing of components • Confining pressure of 4 MPa; Axial load of 4.5 – 48 MPa
SPP_Cal02	11/11/08	Mg	Compliance test at 200 lb.force • Confining pressure of 1 MPa; Axial load of 2 – 24 – 2 MPa
SPP_Cal03	10/12/08	Mg	Compliance test at 300 Nm • Confining pressure of 1 MPa; Axial load of 2 – 48 – 2 MPa
SPP_Cal04	16/12/08	Mg	Compliance test at 300 Nm • Confining pressure of 1 MPa; Axial load of 2 MPa • Confining pressure of 46 MPa; Axial load of 48 MPa • Confining pressure of 1 MPa; Axial load of 48 MPa
SPP_Cal05	12/1/09	Mg	Compliance test at 300 Nm • Confining pressure of 2 MPa; Axial load of 2.5 MPa • Confining pressure of 2 MPa; Axial load of 2.5 – 48 MPa
SPP_Cal06	21/7/09	Mg	Compliance test at 300 Nm • Confining pressure of 1–40 MPa; Axial load of 20 – 48 – 10 MPa
SPP_Cal07	16/10/09	Mg	Test of compliance: • Confining pressure of 1 MPa; Axial load of 3.8 – 28.5 – 3.8 MPa • Axial load of 11 MPa; Confining pressure of 1 – 5 – 1 MPa
SPP_Cal08	13/11/09	Mg	Test of radial dash pots: • Confining pressure of 1 MPa; Axial load of 1.5 – 20 – 1.5 MPa • Confining pressure of 5 MPa; Axial load of 6 – 22 – 6 MPa • Confining pressure of 10 MPa; Axial load of 12 – 35 – 12 MPa
SPP_Cal09	16/11/09	Mg	Test of radial dash pots: • Confining pressure of 10 MPa; Axial load of 12 – 35 – 12 MPa • Confining pressure of 20 MPa; Axial load of 24 – 45 – 24 MPa • Confining pressure of 30 MPa; Axial load of 34 – 46 – 34 MPa • Confining pressure of 30 MPa; Axial load of 33 – 47 – 33 MPa
SPP_Cal10	16/11/09	Mg	Repeated loading cycles • Confining pressure of 10 MPa; Axial load of 11–35–11 MPa × 3
SPP_Cal11	17/11/09	Mg	Check of LVDTs • Confining pressure of 20 MPa; Axial load of 24 – 45 – 24 MPa • Confining pressure of 30 MPa; Axial load of 33 – 47 – 33 MPa
SPP_Cal12	18/1/10	Mg	Compliance test • Confining pressure of 1 MPa; Axial load of 1.5 – 20 – 1.5 MPa • Confining pressure of 5 MPa; Axial load of 6 – 25 – 6 MPa • Confining pressure of 10 MPa; Axial load of 12 – 35 – 12 MPa • Confining pressure of 20 MPa; Axial load of 24 – 45 – 24 MPa • Confining pressure of 30 MPa; Axial load of 34 – 46 – 34 MPa
SPP_Cal13	9/2/10	Mg	Pressure cycle test at 10 MPa. • Confining pressure of 10 MPa; Axial load of 12–35–12 MPa × 3
SPP_Cal14	2/3/10	Wg	Compliance test with Tungsten • Confining pressure of 1 MPa; Axial load of 1.5 – 20 – 1.5 MPa • Confining pressure of 5 MPa; Axial load of 6 – 25 – 6 MPa • Confining pressure of 5 MPa; Axial load of 12 – 35 – 12 MPa • Confining pressure of 5 MPa; Axial load of 24 – 45 – 24 MPa • Confining pressure of 10 MPa; Axial load of 12 – 35 – 12 MPa • Confining pressure of 20 MPa; Axial load of 24 – 45 – 24 MPa • Confining pressure of 30 MPa; Axial load of 34 – 46 – 34 MPa • Confining pressure of 10 MPa; Axial load of 12–35–12 MPa × 4
SPP_Cal15	4/5/10	/	Pump calibration (injection & back-pressure)
SPP_Cal16	5/5/10	/	Pump calibration (axial load)
SPP_Cal17	5/5/10	/	Pump calibration (confining pressure)
SPP_Cal18	Tba	/	Guard-ring pressure transducer calibration

Table 2-2 List of calibration tests undertaken to prove and calibrate the SPP apparatus.

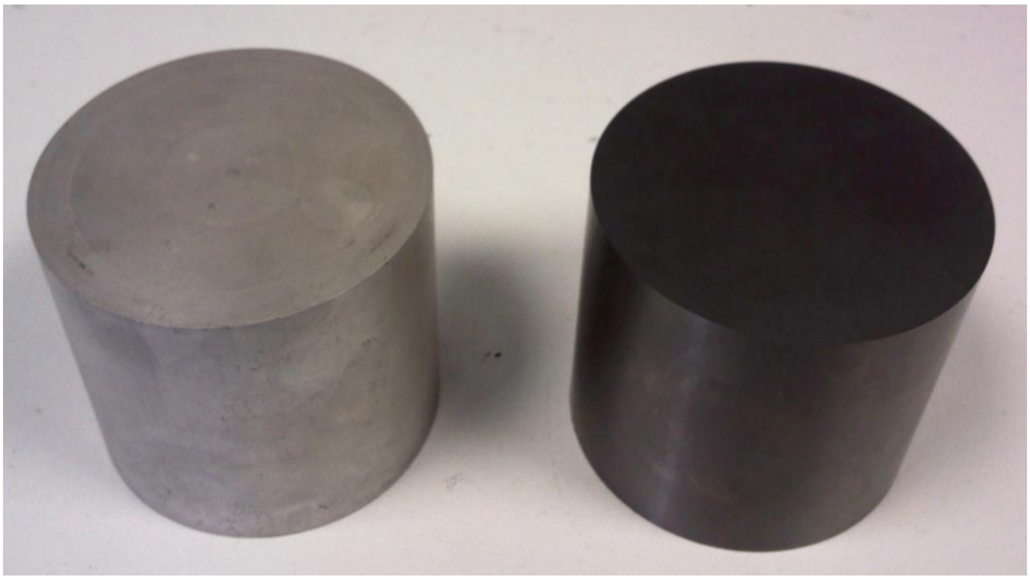

Figure 2-7 Calibration dummy samples; Magnesium alloy (left) and Tungsten (right).

Confining pressure (MPa)	Axial load (MPa)	Axial displacement (micron)	Radial displacement (micron)	Calculated axial displacement (microns)	Calculated radial displacement (microns)
Magnesium alloy					
1	1.5 – 20 – 1.5	43 (10)	7 (1.3)	22	6.4
5	6 – 25 - 6	34 (6)	5 (0)	22.6	6.6
10	12 – 35 – 12	43 (8)	6 (1)	27.4	7.9
20	24 – 45 – 24	36 (8)	3 (0)	25.0	7.3
30	34 – 46 – 34	15 (4)	1 (0)	14.3	4.1
10	12 – 35 – 12	36 (-1)	4.5 (-1)	27.4	8.9
10	12 – 35 – 12	50 (11)	6.6 (-1.4)	27.4	8.9
10	12 – 35 – 12	46 (9)	5.6 (2.1)	27.4	8.9
Tungsten					
1	1.5 – 20 – 1.5	15 (-3)	23.6 (8.4)	22.5	7.3
5	6 – 25 - 6	10 (-2)	12.7 (2.7)	23.1	7.5
5	12 – 35 – 12	8 (0)	12.4 (2.5)	27.9	9.1
5	24 – 45 – 24	3 (1)	10.8 (0.7)	25.5	8.3
10	12 – 35 – 12	6 (-2)	13.8 (0.1)	27.9	9.1
20	24 – 45 – 24	2 (-1)	17.4 (-0.3)	25.5	8.3
30	34 – 46 – 34	1 (1)	25.5 (-0.2)	14.6	4.7
10	12 – 35 – 12	5 (-1)	14.2 (1.4)	27.9	9.1
10	12 – 35 – 12	4 (4)	13.1 (0.6)	27.9	9.1
10	12 – 35 – 12	4.5 (0.5)	12.1 (0.4)	27.9	9.1
10	12 – 35 – 12	2 (0.5)	11.9 (0.3)	27.9	9.1

Table 2-3 Results for compliance testing experiments with aluminium alloy bar and tungsten bar (parenthesis report values of hysteresis).

The magnesium alloy test bar measured 50 mm in length and 56 mm in diameter; Its Young's modulus and Poisson's ratio was certified as 41.97 GPa and 0.29 respectively. The tungsten test bar measured 50.01 ± 0.01 mm in length and 56 ± 0.06 mm in diameter; Its Young's modulus and Poisson's ratio was assumed to be 411 GPa and 0.29 respectively. The test bars were subjected to a series of increasing and then decreasing axial stresses at confining pressures of 1, 5, 10, 20, and 30 MPa. Care was taken not to overload the samples and differential axial loading was limited to 25 MPa. Axial and radial displacements were observed during the pressure cycles and the results are given in Table 2-3. These results show that the apparatus was stiff, especially when one considers the likely strength and deformability of Callovo-Oxfordian claystone. Therefore the deformation of the experimental apparatus can be considered negligible compared with the expected deformation of the test material.

2.5 ORIGINAL PLANNED EXPERIMENTAL PROGRAMME

The experiment was conducted with a control on axial load, confining pressure and pore-pressure. The resultant strains were monitored on the platen ends and at three locations around the sample centre. The sample was able to undergo volumetric deformation and was only constrained by a confining fluid. The experiment planned to follow given stress-paths. A series of steps would approximate the paths by changing axial load and confining pressure; if necessary pore-pressure could also be altered. While the transition between steps was relatively quick, stress conditions were held constant for several weeks in order to achieve steady flow conditions.

The experimental programme was not fixed and the results and observations from one test fed into the next. The original plan was to conduct five experiments in order to examine the evolution of aqueous and gaseous permeability in response to changes in effective stress. Figure 2-8 shows the position of the Hoek-Brown failure criterion as supplied by Andra for COx when plotted in the $q - p$ space. The stress state of Bure is well defined with a confining pressure of 12.5 MPa. A pore-pressure of 4.5 MPa is typical, giving a starting effective mean stress of 8 MPa for all stress-paths. Table 2-4 summarises the original planned test programme.

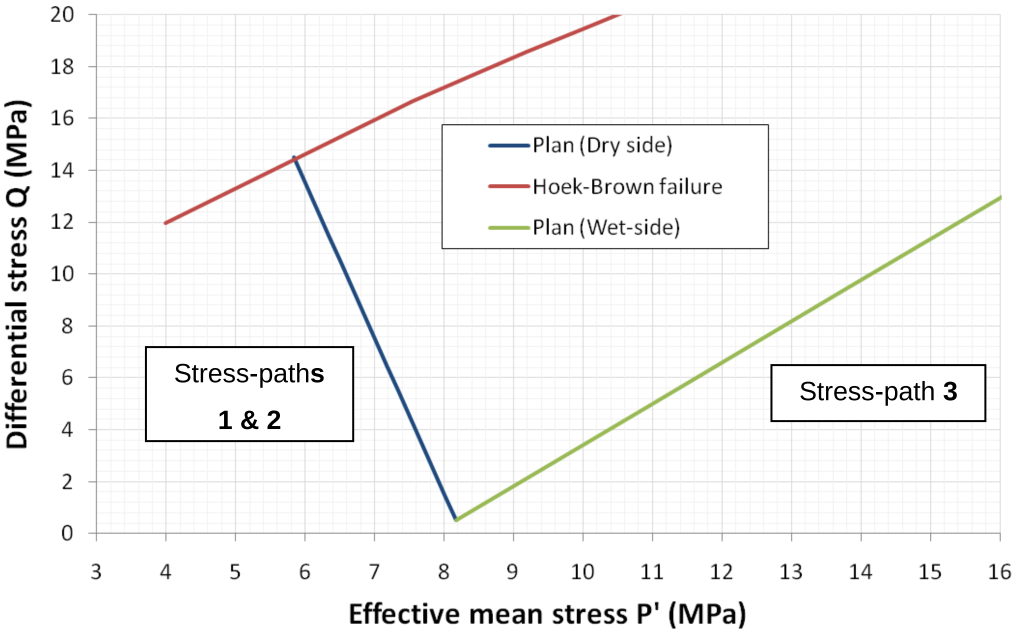

Figure 2-8 Hoek-Brown failure envelope as supplied by Andra and the BGS proposed stress-paths.

2.6 STRESS-PATH 1 - DRY SIDE DEFORMATION WITH NO POREWATER PRESSURE

The original plan for the first test (Test 1) was to perform deformation experiment with a constant pore-water pressure (drained) with relatively quick steps. This stress-path (see Figure 2-8) simulated rapid stress changes during the construction phase of a repository. Failure would be achieved by simultaneously altering both confining pressure and load stress. The test plan was as follows:

- Specimen to be fully resaturated ($S_w > 0.99$) while subject to the original conditions of effective stress.

- Simultaneous increments in both load and confining pressure then applied to the specimen (while monitoring volume change) in order to achieve failure.
- Post-test analysis of the core performed to examine fabric deformation along individual failure planes and to quantify the basic geotechnical properties of the remaining core.

The aim of this test was to define the location of the Hoek-Brown failure envelope through a number (>13) of steps of short duration (3 – 7 days). This information would then be used to select 4 – 5 steps for a much more detailed test (Stress-path 2).

2.7 STRESS-PATH 2 - DRY SIDE DEFORMATION WITH PORE-PRESSURE

The original plan for the second test (Test 2/3) was to be identical to that used in Stress-Path 1. Stress-path 2 would be driven at a much slower rate than for Stress-Path 1 with a pressure gradient between the injection and back-pressure filters to initiate flow and measure the evolution in transport properties. It was anticipated that four or five steps would be selected, pausing the stress-path and measuring the permeability at key points of the test. This experiment would help to confirm whether or not permeability changes below the failure envelope and whether permeability begins to alter before any other mechanical indicator is observed. The test would be conducted as follows:

- Specimen to be fully resaturated ($S_w > 0.99$) while subject to the original conditions of effective stress.
- The intrinsic permeability of the specimen measured by a combination of controlled flow rate and/or constant head methodologies using a synthetic groundwater solution.
- For gas testing (Test 2): After a period of pore-pressure equilibration, gas testing (using H_e as the permeant) would commence using a combination of controlled flow rate and/or constant pressure techniques until a steady stream of gas was observed, thereby determining the initial gas transport parameters.
- Simultaneous increments in both load and confining pressure would then be applied to the specimen (while monitoring volume change) in order to achieve failure.
- The intrinsic permeability of the specimen would be measured at each increment of stress in order to define the change in intrinsic permeability.
- Post-test analysis of the core would be performed to examine fabric deformation along individual failure planes and to quantify the basic geotechnical properties of the remaining core.
- For water testing (Test 3): The location of any aqueous tracers which may have been used would be investigated at this time.

The aim of these two experiments was to examine the role the stress-path has on transport properties and defining the onset of any changes in permeability.

2.8 STRESS-PATH 3 - WET SIDE DEFORMATION WITH POREWATER PRESSURE

If time permitted, a third stress-path (see Figure 2-8) would be investigated in order to look at the long-term convergent deformation observed over much longer time scales; this would result in a stress-path that induced wet-side deformation. This may result in significantly different processes and permeability evolution from that observed in Stress-Path 2. The test programme would be identical to that described for Stress-Path 2, but along a different stress-path.

Test Number	Stress-path	Permeant	Type of test	Steps	Detail	Conducted	Test
Test 1	Dry-side	Water	Drained	~10	Quick	Yes	SPP_COx-1
Test 2	Dry-side	Gas	Flow	~5	Detailed	Part	SPP_COx-2
Test 3	Dry-side	Water	Flow	~5	Detailed	No	/
Test 4	Wet-side	Water	Drained	~10	Quick	No	/
Test 5	Wet-side	Gas	Flow	~5	Detailed	No	/

Table 2-4 Original planned test programme.

2.9 MODIFICATION TO THE TEST PROGRAMME

As previously stated, the experimental programme had to modify for a number of reasons:

1) The results presented in Section 3 show that COx has a very pronounced time dependent component of deformation. This means that for large 55mm diameter samples it is necessary to have long duration steps of testing. This time-dependency means that each step of a stress-path has to be conducted for prolonged periods to allow the sample to achieve near steady-state flow conditions. This resulted in priority being given to gas flow experiments, with water flow experiments conducted only if time allowed.

2) The gas entry pressure experienced in test SPP_COx-2 was much greater than had been anticipated and was close to the confining pressure. A common constraint of rock deformation experiments is the limitation of having confining pressure greater than pore-pressure. The jacket seal arrangement in the SPP is likely to leak if pore-pressure greatly exceeds confining pressure. The dry-side stress-path requires confining pressure to reduce whilst axial load increases, which would result in jacket leakage. Therefore it proved problematic with the existing configuration of the SPP to follow a stress-path.

Therefore it was necessary to modify the test programme in light of the observed behavior. The modifications were agreed between BGS, Andra and the co-ordinator of the FORGE project.

3 Test SPP_COx-1 (mechanical test)

The first test, designated SPP_COx-1, was a relatively quick test in order to confirm the location of the Hoek-Brown failure envelope. The stress level at which failure occurred would be important in the following gas experiment (SPP_COx-2), which would follow the same stress-path but with five detailed steps designed to observe the changes in permeability during deformation.

The sample was loaded into the SPP apparatus on the 5th May 2010. The axial ram pump was set to a low pressure of 250 kPa so that the ram piston came in contact with the sample end. The axial pump pressure was then increased to 500 kPa to ensure that the sample and pistons were in direct contact. The first stage of the experiment consisted of a swelling stage at a confining pressure of 11.5 MPa, axial load of 12.5 MPa and pore-water pressure of 4.5 MPa (see Table 3-5). In order to achieve these starting conditions eight steps were undertaken over a period of one hour:

1. Axial load of 3 MPa, confining pressure of 2 MPa
2. Axial load of 6 MPa, confining pressure of 5 MPa
3. Axial load of 8 MPa, confining pressure of 7 MPa
4. Introduction of pore-water pressure of 1 MPa to drain circuits (central filter first followed by outer guard-rings). All circuits successfully drained.
5. Axial load of 10 MPa, confining pressure of 9 MPa
6. Pore-pressure raised to 2 MPa
7. Axial load of 12.5 MPa, confining pressure of 11.5 MPa
8. Pore-pressure raised to 4.5 MPa on both the injection and back-pressure circuits.

The slow progression to the starting pressure meant that the sample was not overloaded or damaged; or at least damage was minimised. Once the starting stress had been achieved this was considered to be time zero.

Table 3-5 shows the test history. The supplied Hoek-Brown failure envelope shows that COx should fail at a confining pressure of 5.5 MPa and axial load of 20 MPa (with 4.5 MPa porewater pressure); step 15 in Table 3-5. The designated stress-path has one additional stage to ensure that failure is achieved. The Andra dossier argile (Andra 2005[a,b]) shows that COx has a variable strength. A total of 23 steps were defined that would take the stress-path beyond the Hoek-Brown failure criterion to achieve failure of the sample; during testing it was seen that failure occurred at stage 16.

The original plan allowed three to four days per step. It was anticipated that steps could be progressed at 9am on Monday morning and 5:30pm on Thursday; approximately 3.5 days. This would allow two steps a week and a total test of 8 weeks. However, as will be shown, four days per step was not sufficient and after the first few steps it was decided to allow seven days per step. It should be noted that this time was insufficient, but was a balance between achieving equilibrium and completing the test within a satisfactory timescale.

Step	Confining pressure (MPa)	Pore-pressure (MPa)	Axial load (MPa)	Differential load (MPa)	Differential stress Q (MPa)	Effective mean stress P' (MPa)	Start time (day)	End time (day)
Swell	11.5	4.5	12.5	1.0	1.0	7.33	0	15.1
1	12.5	4.5	13.0	0.5	0.5	8.17	15.1	17.9
2	12.0	4.5	13.5	1.5	1.5	8.00	17.9	22.1
3	11.5	4.5	14.0	2.5	2.5	7.83	22.1	26.9
4	11.0	4.5	14.5	3.5	3.5	7.67	26.9	35.1
5	10.5	4.5	15.0	4.5	4.5	7.50	35.1	41
6	10.0	4.5	15.5	5.5	5.5	7.33	41.0	15.9
7	9.5	4.5	16.0	6.5	6.5	7.17	45.9	50.1
8	9.0	4.5	16.5	7.5	7.5	7.00	50.1	60.9
9	8.5	4.5	17.0	8.5	8.5	6.83	60.9	67.9
10	8.0	4.5	17.5	9.5	9.5	6.67	67.9	73.9
11	7.5	4.5	18.0	10.5	10.5	6.50	73.9	80.9
12	7.0	4.5	18.5	11.5	11.5	6.33	80.9	88.0
13	6.5	4.5	19.0	12.5	12.5	6.17	88.0	94.9
14	6.0	4.5	19.5	13.5	13.5	6.00	94.9	101.9
15	5.5	4.5	20.0	14.5	14.5	5.83	101.9	108.9
16	5.0	4.5	20.5	15.5	15.5	5.67	108.9	123.2

Table 3-5 Summary of experimental history for test SPP_CoX-1 showing step number, axial stress and confining stress.

3.1 SWELLING STAGE

The first step of testing lasted 15 days and was designed to allow the test to equilibrate with the synthetic porewater fluid and naturally swell. The system was setup with a confining pressure of 11.5 MPa, axial load of 12.5 MPa and porewater pressure of 4.5 MPa. The results of this stage can be seen in Figure 3-1. As shown in Figure 3-1a, it can be seen that radial strain of the COx sample is heterogeneous; with radial 1 showing the most deformation and recording more than twice the displacement seen of radial 2, which showed the least strain. Figure 3-1b compares the strains recorded (axial, radial and volumetric). It can be seen that the small strains recorded are comparable and confirm that the SPP apparatus performs well. The sign of the strain shows that the overall sample volume is increasing as the sample swelled.

Figure 3-1c shows the flow of the four ISCO pumps of the SPP apparatus (confining, axial, injection and back-pressure circuits). It can be seen that all four pumps took approximately 8 days to achieve the usual low flows (<5 µl.h^{-1}) expected for stable conditions. Initially the flow from the porewater pressure system shows an outflow of fluid. The asymptote of these curves suggest that the outflow of water is related to the time-dependent compression seen in the sample.

The two highlighted events (Day 8.1 and Day 10.95) correspond to a weekend where power to BGS Keyworth was shutdown and the laboratory was switched to a generator supply. This had a consequence on the air-conditioning in the environmental room of the laboratory, which can be seen to have an effect on the flow of the confining and axial flows. However, there is no indication of any effect on the test sample.

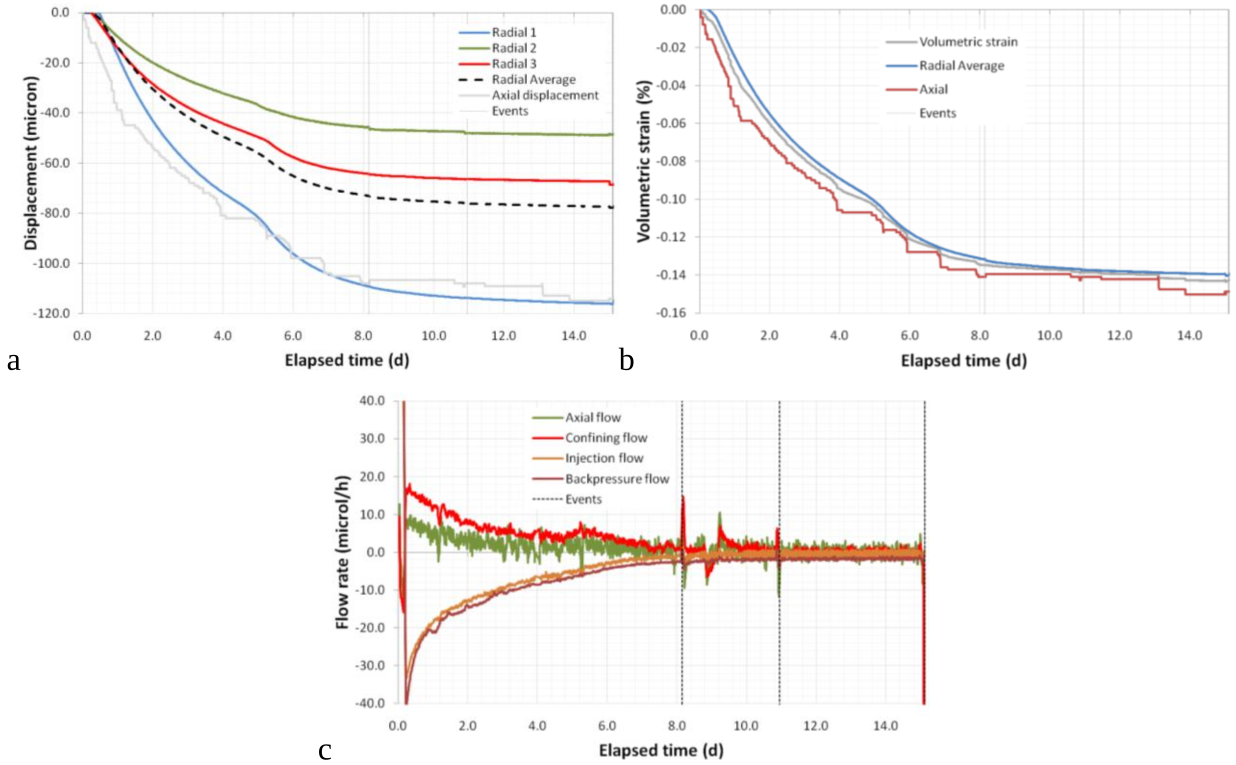

Figure 3-1 Swelling stage of the experiment. A) radial and axial displacements. B) Comparing strains. C) Flow of all four ISCO pumps during the swelling of the sample.

3.2 COMPLETE TEST HISTORY

Figure 3-2 shows the stress-path followed during the complete test history for SPP_COx-1. As can be seen a straight stress-path has been achieved with 16 steps following the swelling stage up to failure, which resulted in deviation of the stress-path. The position of the Hoek-Brown failure envelope shows the expected stress conditions for inducing failure.

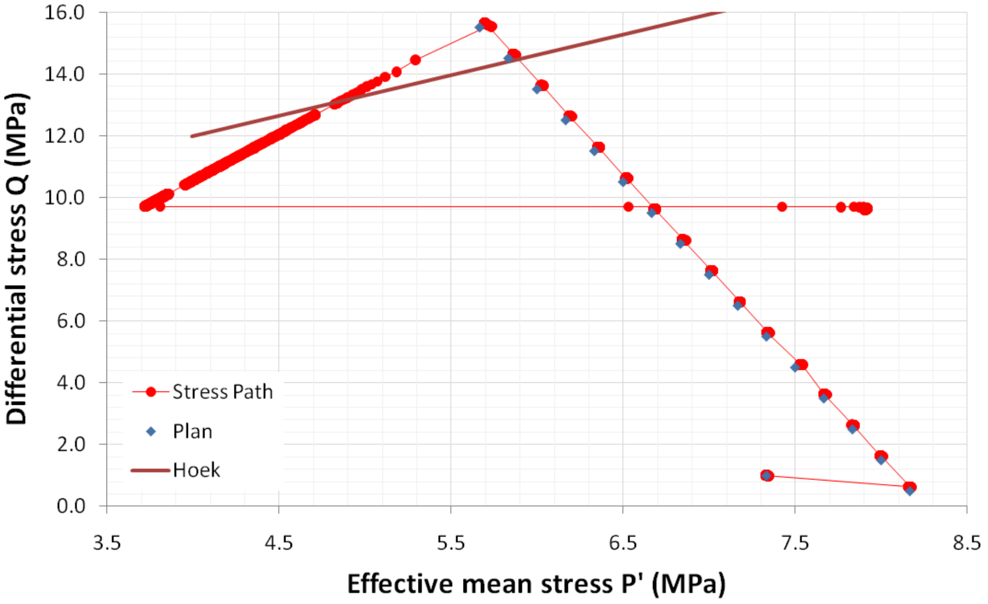

Figure 3-2 Stress-path followed during test SPP_COx-1.

3.2.1 Observations of strain measured directly

The SPP apparatus has been designed to more accurately measure the strain of the sample in the apparatus during deformation. Figure 3-3 shows the displacements of the axial and three radial displacement sensors. As can be seen, following the dilation of the sample during the swelling stage, the first step of the stress-path resulted in time dependent contraction of the sample in all three radial displacements. The second step of testing showed very little displacement in the radial plane. From step 3 onwards (Day 22.07), each successive step showed an increasing time-dependent characteristic with increasing dilation seen of the radial plane. The anisotropy seen in the radial displacements during swelling continues throughout the test history with radial 1 showing twice the displacement of radial 3.

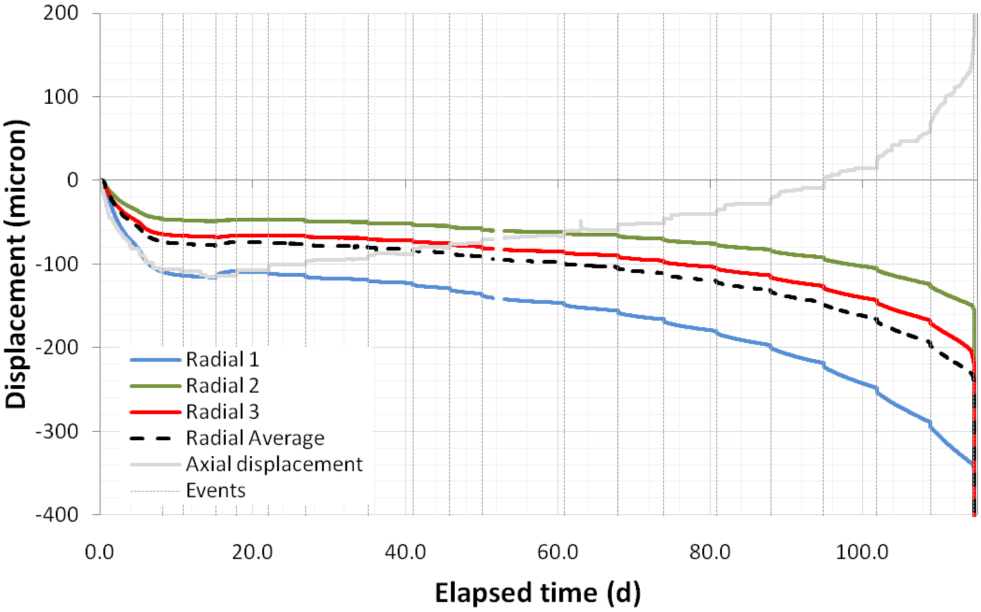

Figure 3-3 Axial and radial displacements measured during test SPP_COx-1.

Following the swelling stage, where the sample was seen to lengthen, the overall change in axial displacement was a sample shortening (see Figure 3-3 and Figure 3-4). The resolution of the axial displacement LVDT meant that the detail was not as well defined as for radial displacements. The axial displacement setup was prone to "stick-slip", which is believed to be a characteristic of the apparatus and not representative of sample deformation. The axial measurement system was also more sensitive to temperature variations within the laboratory, as seen about Day 63.

Figure 3-5 shows the strain recorded for the complete test history. Volumetric strain (ε_v) was calculated from the average of the three radial strains (ε_{rad}) and axial strain (ε_{ax}) [$\varepsilon_v = 2\ \varepsilon_{rad} + \varepsilon_{ax}$]. Good agreement is seen between the strains recorded in the axial and radial directions during the swelling stage of the test, showing that swelling was homogeneous. The first two steps of the test resulted in an overall contraction of the sample volume. From stage three onwards it is seen that radial deformation dominates and that the overall sample volume increased.

It is evident that the recorded displacements were highly time-dependent. Figure 3-6a and Figure 3-6b show the time dependent nature of all displacements and average of radial displacement respectively. For each step change in the stress-path displacements have been reset to zero to highlight the time-dependency. As can be seen, step one and two were anomalous compared with the rest of the steps. During step 1 radial displacement shows that the sample contracted, while no change in axial displacement was seen. During step 2 very little time-dependent deformation was observed and the sample did not contract or expand in response to this stress change.

Following step 2, all consecutive steps were seen to have an increasing time-dependent component in radial displacement and consistent axial component. It can be clearly seen that asymptote had not been reached in any of the steps and would take a considerable time to be achieved.

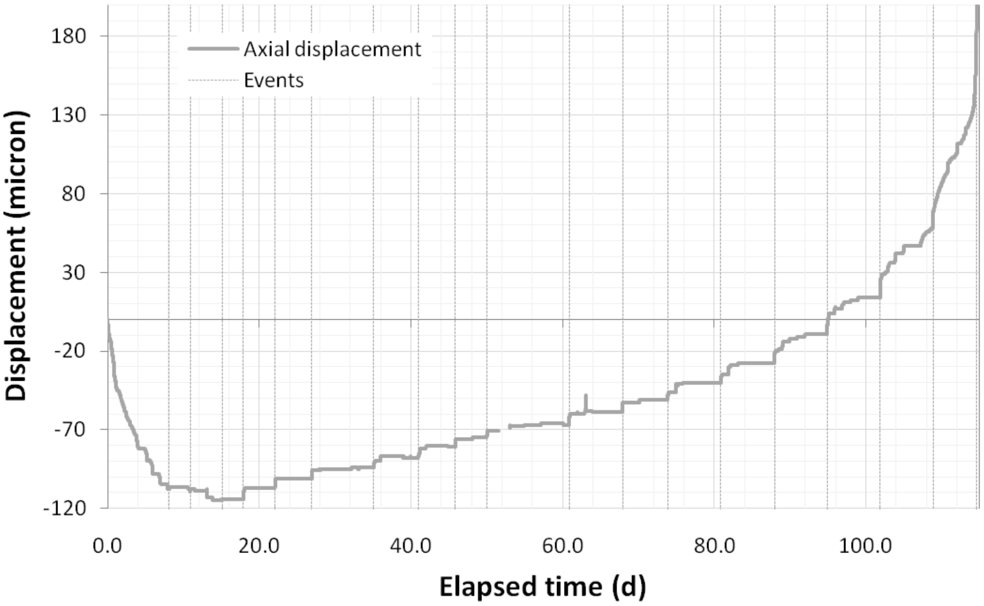

Figure 3-4 Axial displacement in more detail for test SPP_COx-1.

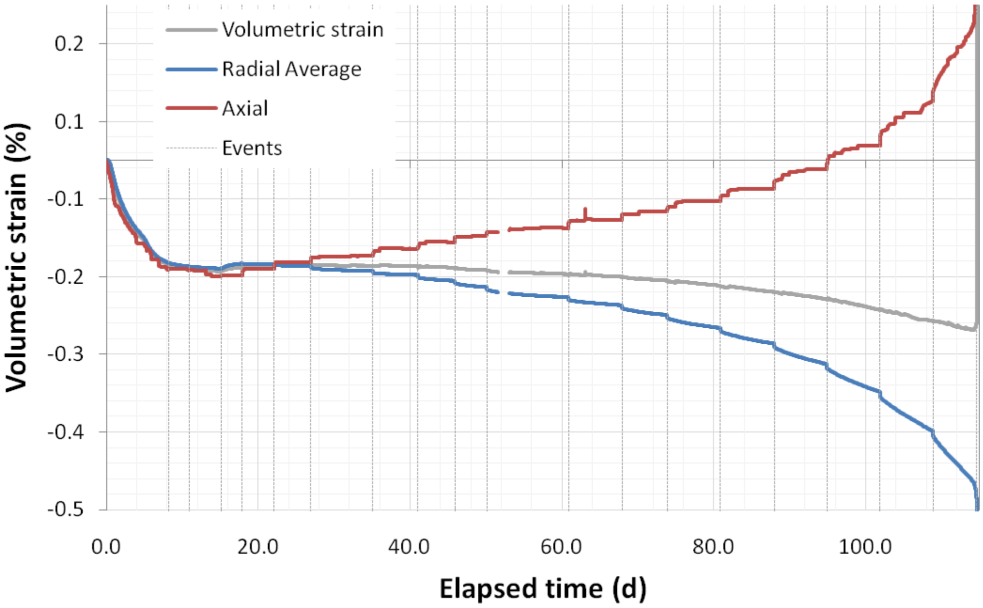

Figure 3-5 Strain observed during test SPP_COx-1.

Figure 3-6c shows the average radial displacement for all steps plotted as a function of the elapsed time of each step. This clearly shows that the time-dependent component of deformation generally increased as the stress-path developed. However, this was not always the case; it was decided to hold step 7 for an increased 11 days to observe the influence this would have on the time-dependency. All steps up to 7 have an increasing curve; the extended duration of step 7 means that step 8 has a decreased curvature. Steps 8 to 10 showed increasing curves. This suggests that the increasing curve is a consequence of the non-attainment of an asymptote, at least in part.

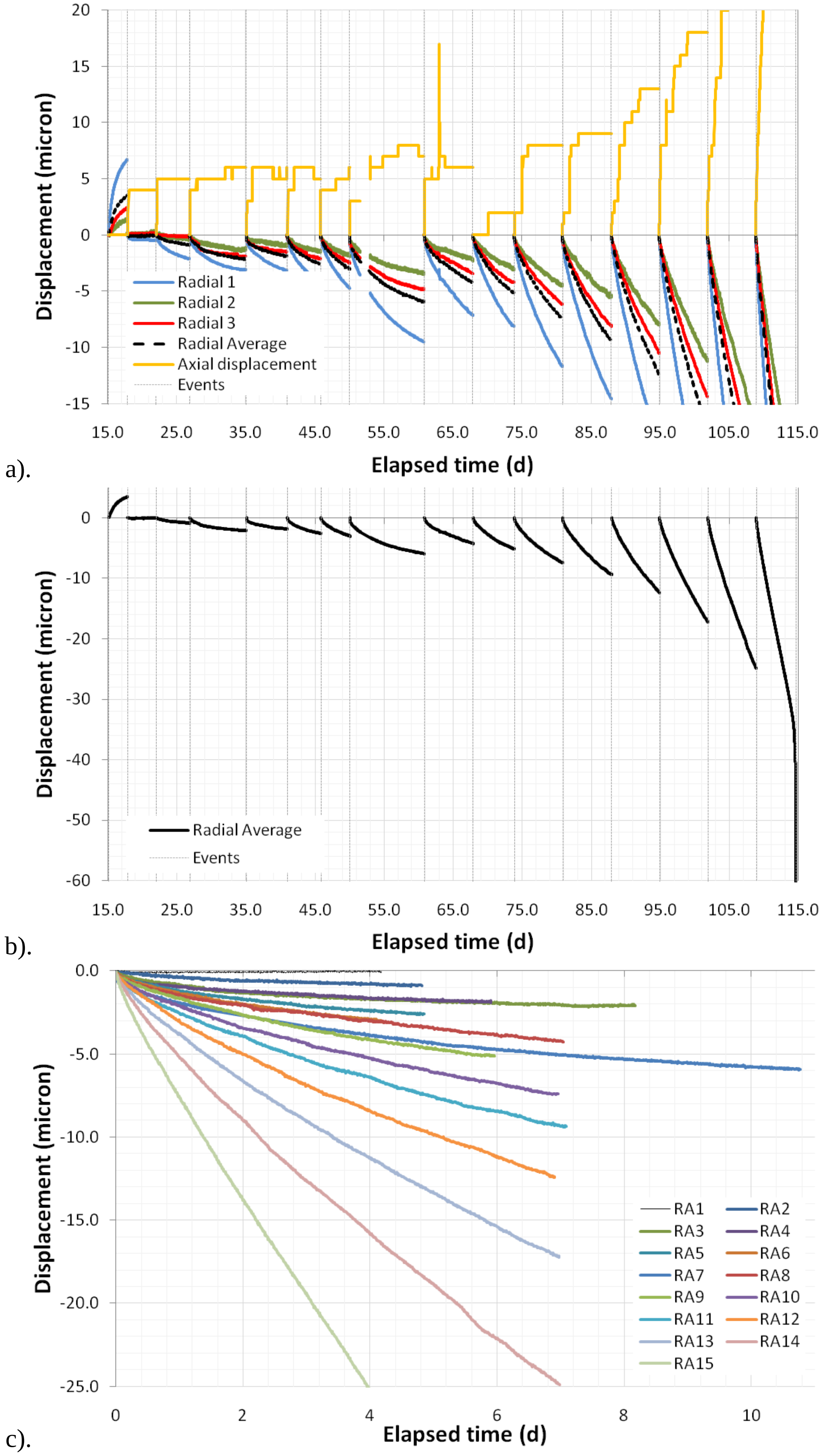

Figure 3-6 Radial displacement observed during test SPP_COx-1. A) Time-dependent radial and axial displacement. B) Time-dependent average radial displacement. C) Time-dependent radial displacement for each step shown for the elapsed time of each step.

3.2.2 Observations of pump flow

Figure 3-7 shows the flow-rate of all four ISCO pumps that operate the SPP rig. As can be seen, all four pumps took approximately 10 days to equilibrate at the start of the test. The injection and back-pressure flow systems showed an outflow as the sample swelled. This soon equilibrated to a low flow smaller than 5 µl.h^{-1}. It can be noted that axial flow, which generally has the greatest degree of "noise", becomes more noisy after a temperature fluctuation within the environmental room of the laboratory at Day 62. Following this time, the temperature of the room was less stable than usual and this was reflected in the noisy flow data.

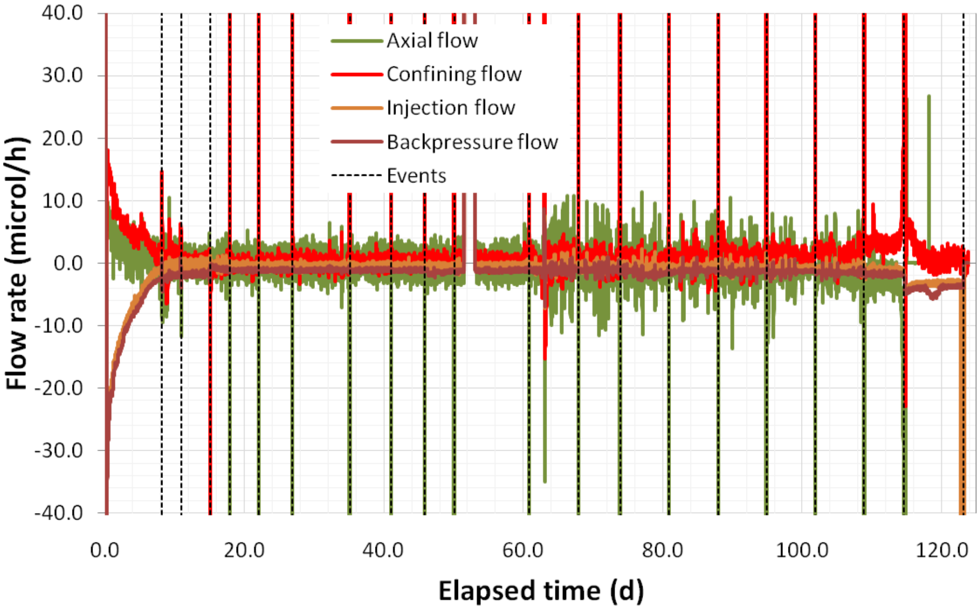

Figure 3-7 Flow rate of all four ISCO pumps used to operate the SPP.

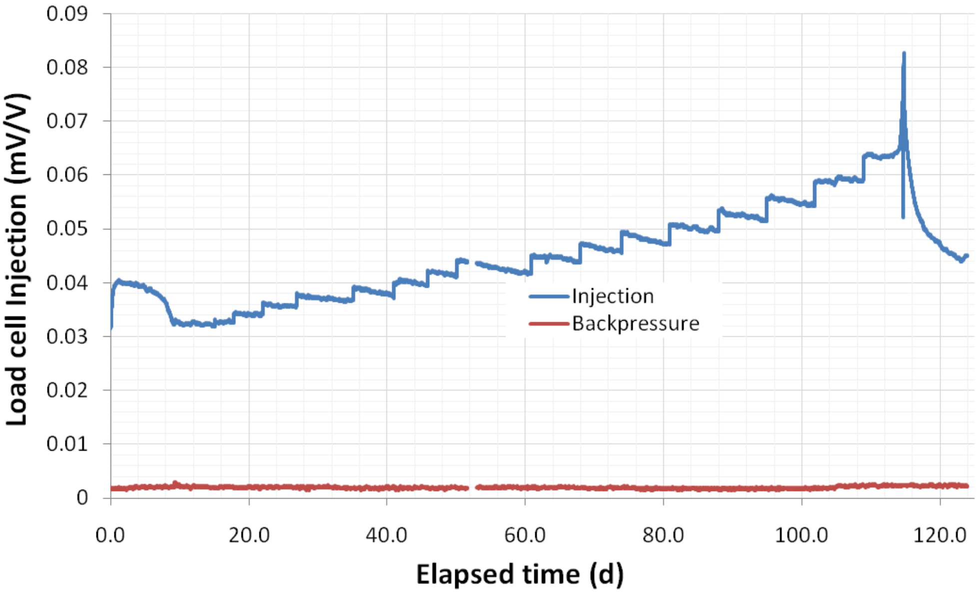

Figure 3-8 Result of axial load cells located at either end of the sample.

3.2.3 Observations of axial load cells

The SPP apparatus had two load cells located in both load platens and these were in direct contact with the sample. Figure 3-8 shows the result for the load cells; it should be noted that this is uncalibrated data in mV.V^{-1}. It is immediatly obvious that the load cell of the back-pressure system is not working. It is expected that the load cells would show a constant and stepped load in keeping with the constant load delivered by the axial load system. However, during the swelling phase of the experiment it can be seen that the load increased and then slowly decayed to the original starting load of 0.032 mV.V^{-1}. The cause of this is not known. During the stress-path it can be seen that load generally increased. However, this had occured in a "saw-tooth" manner, with each successive load increase being followed by a slow load decline. The cause of this feature is not known and may be associated with the time-dependent nature of fluid flow through the sample.

3.2.4 Observations of porewater pressure

Following the success of the guard-ring pore-pressure sensors in the long-term test of COx (Harrington & Noy, 2010), pore-pressure sensors were added to the injection and back-pressure guard-rings following the swelling phase of the experiment. It was not possible to calibrate the pressure sensors at that time, so the pressure that both sensors were recording were assumed to be the same as the pore-pressure measured in the injection and back-pressure pumps (4.5 MPa). Once the transducers were added to the circuit the guard-rings were isolated (Figure 3-9). The pressure in the back-pressure ring increased and peaked 300 kPa above the pressure seen at the point of isolation. The injection circuit increased by over 1.5 MPa and peaked before decaying.

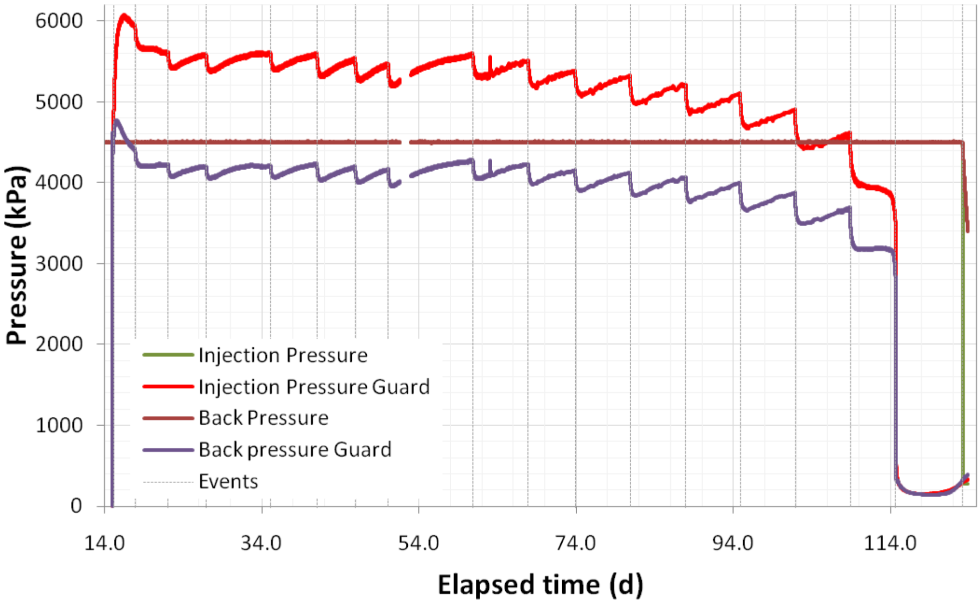

Figure 3-9 Results of the guard-ring porewater pressure during test SPP_COx-1.

What can be seen is that from step 3 onwards (Day 22.07) the behaviour of the guard-ring pressure had been consistent. For each pressure step confining pressure decreased and axial load increased, this resulted in a rapid lowering of pore-pressure of 200 – 300 kPa over several hours, which was followed by a slow increase of pressure. In all steps it can be seen that the pore-pressure had not reached asymptote and so it is not clear as to what level the pore-pressure would have stabilised. It can be seen that as the time-dependent strain became more pronounced this resulted in longer times for pore-pressure to equilibrate. It is an interesting observation that pore-pressure initially dropped as axial load increased and confining pressure decreased. This could be the result of pore fluid being drawn into the sample by dilation, or possibly into the guard-ring itself. The lowering of confining pressure may have resulted in the expansion of volume of available pore space between the sample and the jacket, resulting in a pressure drop. Therefore the exact cause of this pressure response is unclear.

3.2.5 Observations of temperature

The temperature within the environmental room of the laboratory (Figure 3-10) had been kept within the specified ± 0.5° C throughout the experiment. There had been two temperature spikes caused by maintenance of the air-conditioning unit of the laboratory at Day 9 and 62. The latter of these had caused fluctuations in axial displacement and following this time the variation of temperature had become slightly noisy. It should be noted that the greatest variation was observed in the SPP vessel and not the laboratory room. This suggests that one or more of the ISCO pumps was operating more regularly and that this generated localised heat. The temperature fluctuations are not deemed to be problematic.

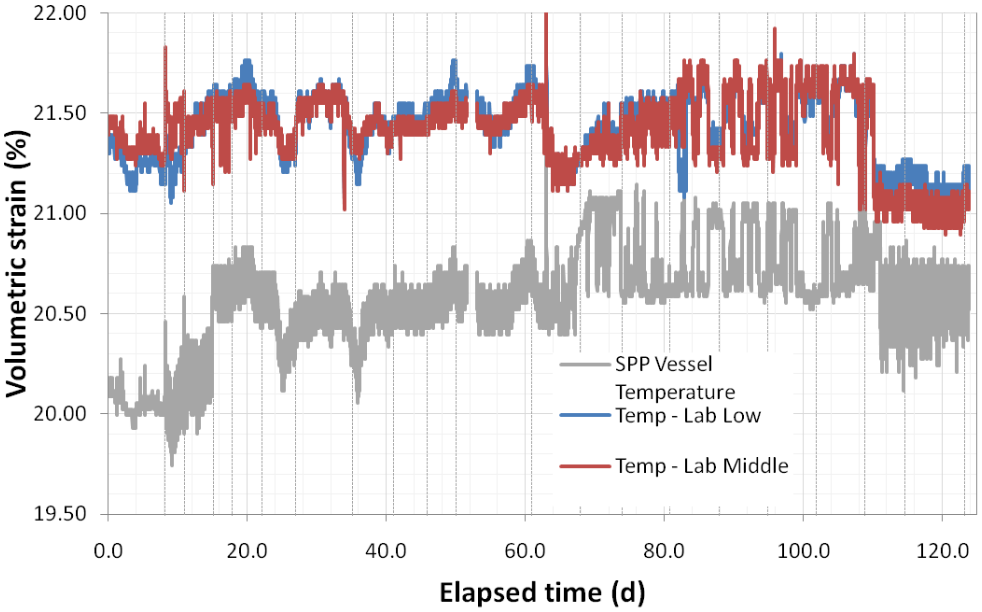

Figure 3-10 Temperature within the environmental room of the TPRL during test SPP_COx-1.

3.3 INDIVIDUAL TEST STAGES

The general observations of Section 3.2 will be further expanded upon with this section for observations of each individual test stage.

3.3.1 Step 1; Day 15.1 – 17.9; σ_1 = 13.0 MPa, $\sigma_{2,3}$ = 12.5 MPa

The first step of the stress-path began at Day 15.1 and lasted nearly 3 days; the results are shown in Figure 3-11. As can be seen in Figure 3-11b, there was no recorded axial displacement during this stage of deformation, whereas axial displacements were all showing that the sample was contracting. Considerable heterogeneity was observed in radial displacement with 6.7, 2.4 and 1.4 µm of displacement occurring in Radial 1, 3 and 2 respectively. Figure 3-11c shows the average radial displacement. This shows that initially sample contraction was linear and after 0.6 days slowly decreased. The nature of the curvature suggests that an asymptote might have been reached if the step was continued for a further 4 or 5 days. Figure 3-11d shows the evolution of pore-pressure within the guard-rings. The back-pressure guard-ring can be seen to evolve much more quickly than the injection one. A peak in pressure was achieved in less than 0.5 days for the back-pressure system, compared with approximately 1.5 days for the injection side. It can also be seen that the back-pressure reduced at a much faster rate than the injection side once peak had been achieved. The reason for these differences is unclear.

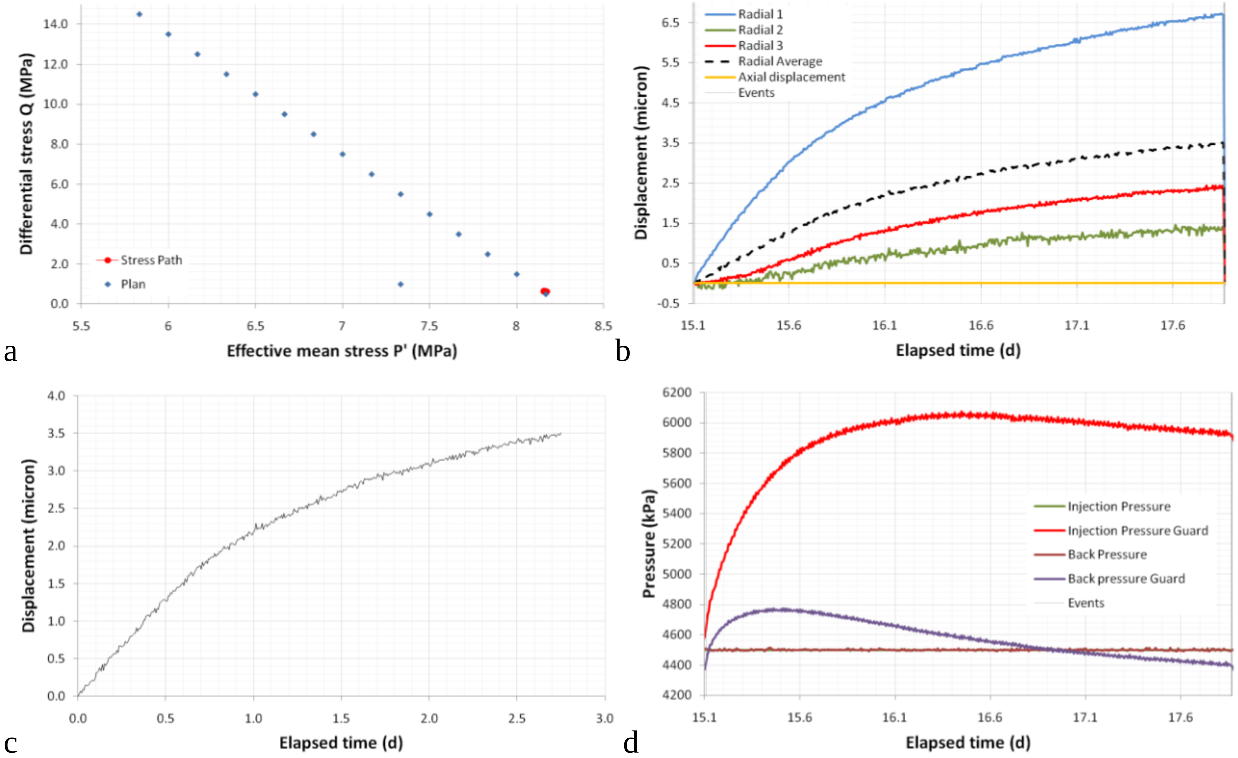

Figure 3-11 Results for step 1 of test SPP_COx-1. A). Location of the stress-path. B) Axial and radial displacement results. C) Average radial displacement. D) Evolution of porewater pressure in the guard-ring assembly.

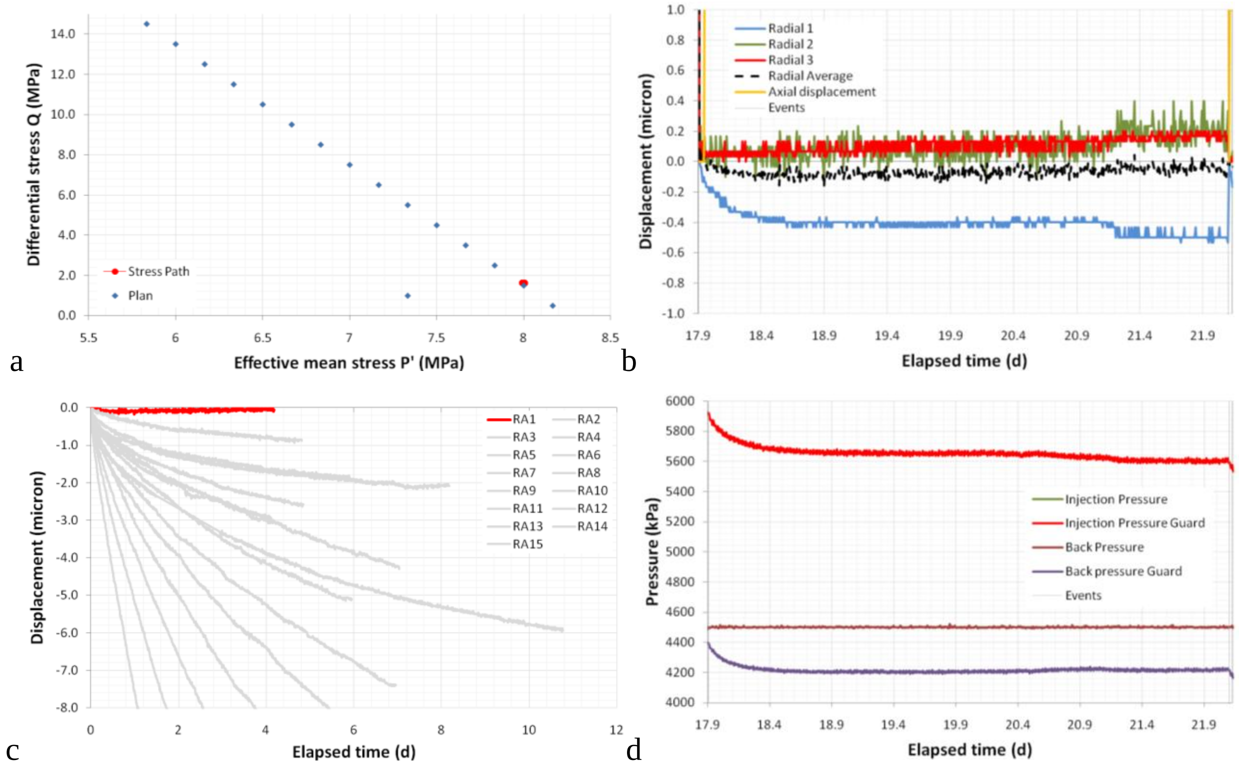

Figure 3-12 Results for step 2 of test SPP_COx-1. A). Location of the stress-path. B) Axial Radial displacement results. C) Average radial displacement in comparison to other test steps. D) Evolution of porewater pressure in the guard-ring assembly.

3.3.2 Step 2; Day 17.9 – 22.1; σ_1 = 13.5 MPa, $\sigma_{2,3}$ = 12.0 MPa

Step 2 of the stress-path lasted approximately 4.2 days and gave some interesting results, as seen in Figure 3-12. The change in stress state resulted in stable deformation, with little time-dependency observed during the stage (see Figure 3-12b). It can even be seen that the observed anisotropy of the radial displacement means that Radial 1 had resulted in dilational time-dependency, whereas radial 2 and 3 had resulted in contractional time-dependency. Generally it can be observed that average radial displacement was close to zero during this stage. The apparent lack of significant time-dependent deformation results in a rapid loss in guard-ring pore-pressure (Figure 3-12d), which was followed by a gradual decline in pressure. This is in contrast to the observations of subsequent stages.

3.3.3 Step 3; Day 22.1 – 26.9; σ_1 = 14.0 MPa, $\sigma_{2,3}$ = 11.5 MPa

The third step of the stress-path lasted nearly five days and the results are shown in Figure 3-13. It can be seen that this step was the first to show considerable time-dependent radial deformation in a dilatational sense. As with the previous stage, considerable anisotropy was observed (Figure 3-13b), with time-dependent displacements of 2.1, 0.3 and 0.1 μm in radial 1, 2 and 3 respectively. The average of radial displacement can be seen to not have achieved asymptote and would have taken considerable time to reach that state. The evolution of pore-pressure within the guard-rings (Figure 3-13d) showed that over the first 0.5 days of the stage the pore-pressure in both injection and back-pressure guard-rings decreased by approximately 200 kPa and for the remainder of the stage slowly increased to a level similar to that at the start of the stage. The fact that pore-pressure increased during this stage and did not in the previous step suggests that there is a connection between the time dependency seen in radial deformation and pore-pressure. It is uncertain whether the time dependent flow of fluid was resulting in a component of creep in deformation, or if the creep was causing the porewater to flow.

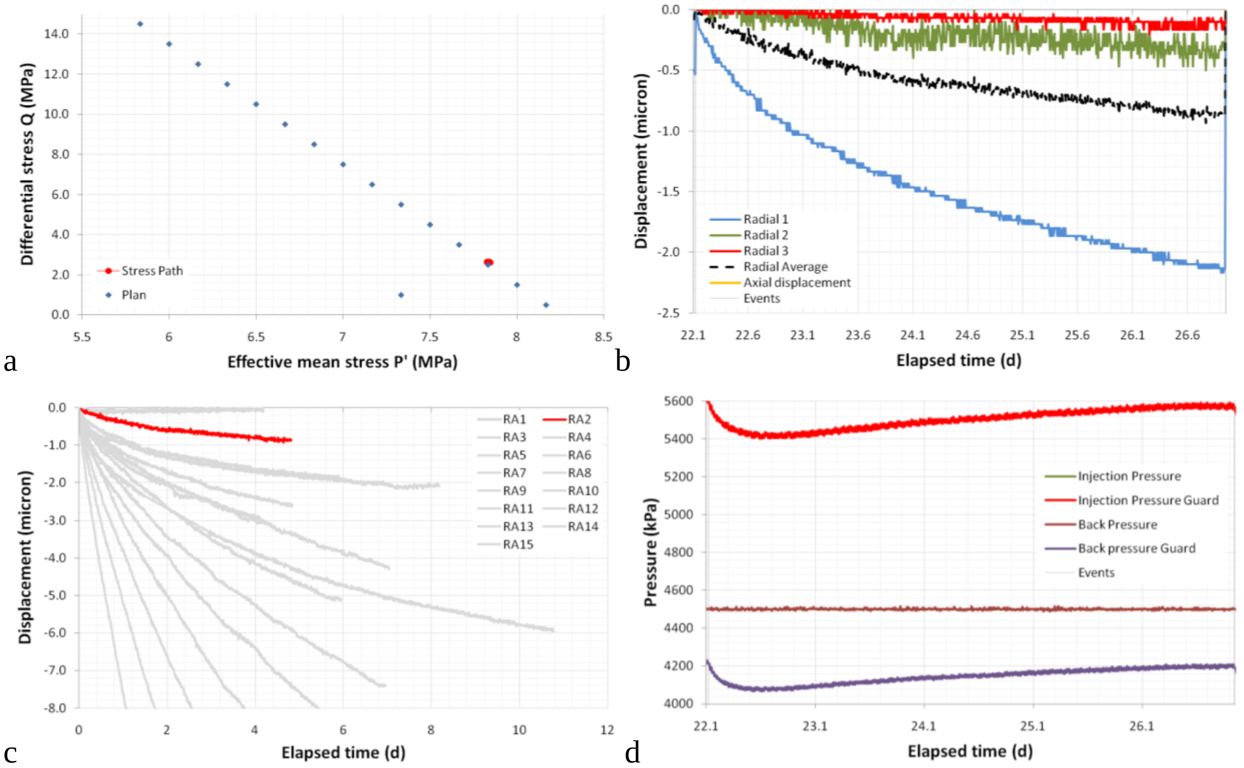

Figure 3-13 Results for step 3 of test SPP_COx-1. A). Location of the stress-path. B) Radial displacement results. C) Average radial displacement in comparison to other test steps. D) Evolution of porewater pressure in the guard-ring assembly.

3.3.4 Step 4; Day 26.9 – 35.1; σ_1 = 14.5 MPa, $\sigma_{2,3}$ = 11.0 MPa

The forth step of the stress-path was run for 8 days and the results are shown in Figure 3-14. It can be seen that once again time-dependency was seen in radial displacement, but in contrast to the previous step the degree of anisotropy had reduced; by the end of the step radial displacements were 3.1, 1.9 and 1.3 µm for radial 1, 3 and 2 respectively (Figure 3-14b). Radial 3 showed an anomalous result during this step, a behaviour that had not been seen in previous steps. At Day 28.2 a step change in radial displacement was observed and at Day 33.7 another step-change occurred; however, this step was less instantaneous than the first. It can be seen the length of the stage meant that asymptote of displacement had been achieved. The evolution of pore-pressure (Figure 3-14d) also reached asymptote. As with the previous step, the first 0.5 days showed a gradual pressure decline of approximately 200 kPa; which was followed by a slow recovery. The porewater pressure in both the injection and back-pressure guard-rings recovered to the same level as at the start of the stage. This suggests that the time-dependency was of the order of 7 – 14 days in length and was not an indication of long-term creep.

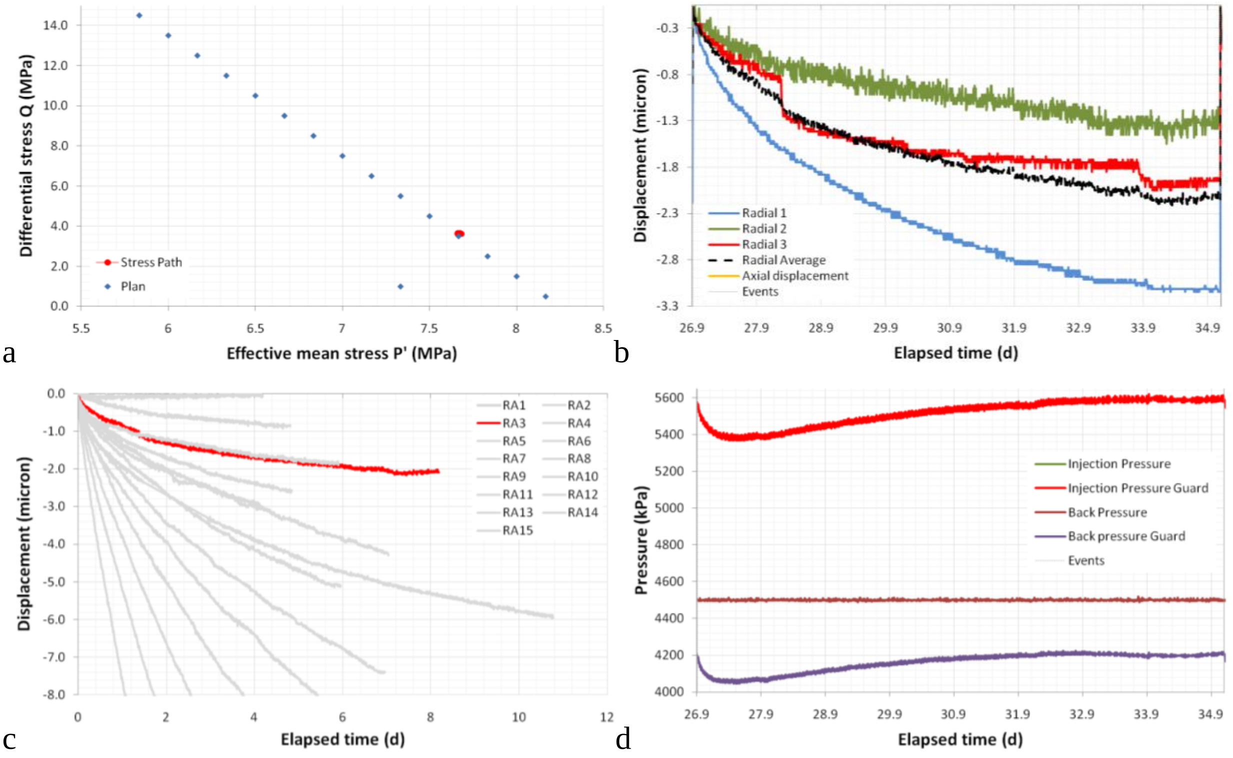

Figure 3-14 Results for step 4 of test SPP_COx-1. A). Location of the stress-path. B) Radial displacement results. C) Average radial displacement in comparison to other test steps. D) Evolution of porewater pressure in the guard-ring assembly.

3.3.5 Step 5; Day 35.1 – 41.0; σ_1 = 15.0 MPa, $\sigma_{2,3}$ = 10.5 MPa

The fifth stage was approximately 6 days long and the results are shown in Figure 3-15. The behaviour of radial 3 displacement was similar in this stage as to step 4 with three step changes. It may be observed that a step change had occurred in radial 1, although this was less clear. As with previous steps, considerable anistropy is observed with radial displacement of 3.2, 1.5 and 0.9 µm of displacement in radial 1, 3 and 2 respectively (see Figure 3-15b). It can be seen that asymptote had not been achieved by the end of the step and it could be a considerable time until radial 1 reached steady-state. Figure 3-15c shows a very important result. It can be seen that the time-dependent deformation of radial displacement plots on top of the previous step. This suggests that a certain amount of the time dependent deformation is as a result of the slow expulsion of fluid from the sample. If asymptote was not achieved then the next step had a greater curvature. This suggests that the time-dependent deformation was created by slow fluid expulsion as well as creep of the COx.

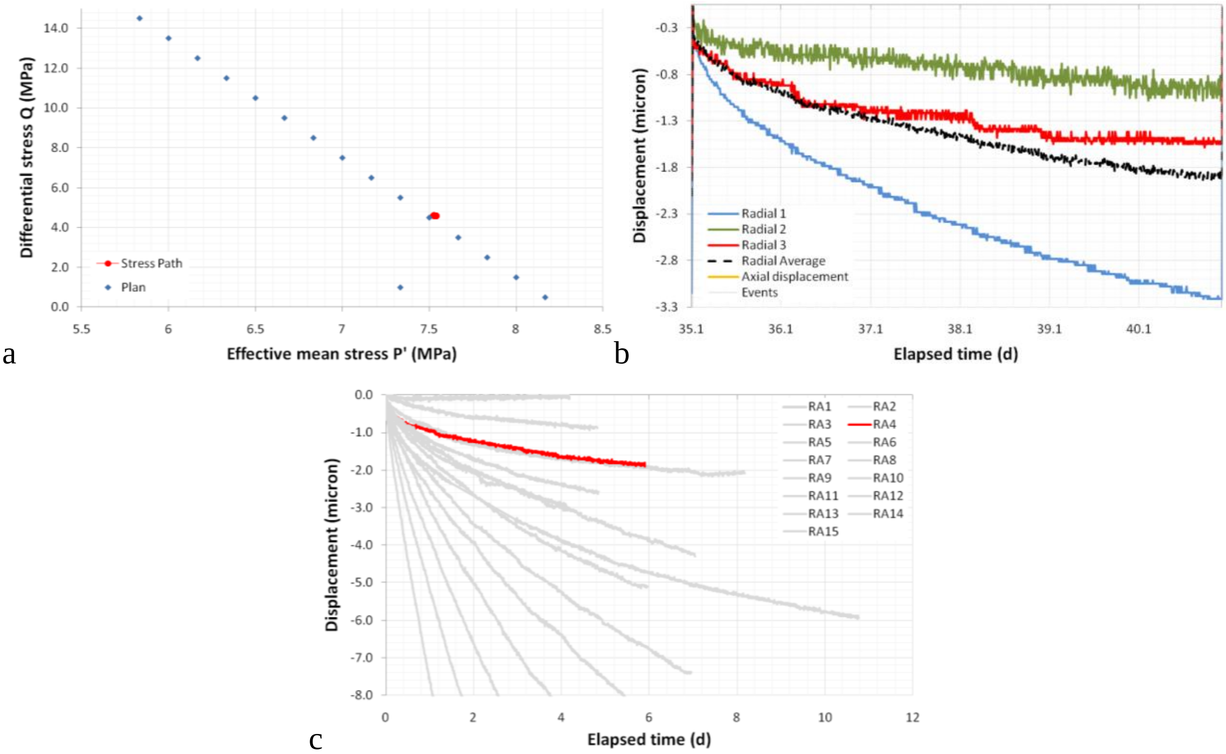

a b

c

Figure 3-15 Results for step 5 of test SPP_COx-1. A). Location of the stress-path. B) Radial displacement results. C) Average radial displacement in comparison to other test steps.

3.3.6 Step 6; Day 41.0 – 45.9; σ_1 = 15.5 MPa, $\sigma_{2,3}$ = 10.0 MPa

The sixth stage was approximately 4 days long and the results are shown in Figure 3-16. As with the previous two steps, radial displacement 1 showed a step change. Overall the sample showed considerable anisotropy with 4.2, 2.1 and 1.4 µm of displacement in radial 1, 3 and 2 respectively (see Figure 3-16b). Figure 3-16c shows that the curvature of time-dependent displacement had increased compared with the previous step, which strengthens the hypothesis that if asymptote was not achieved it influences the following step. Figure 3-16d shows the evolution of porewater pressure in the guard-rings and as with previous steps, showed a 300 kPa drop in the first 0.5 days, followed by a slow recovery. By the end of the step the two pressure transducers were approximately 50 – 100 kPa below their starting level.

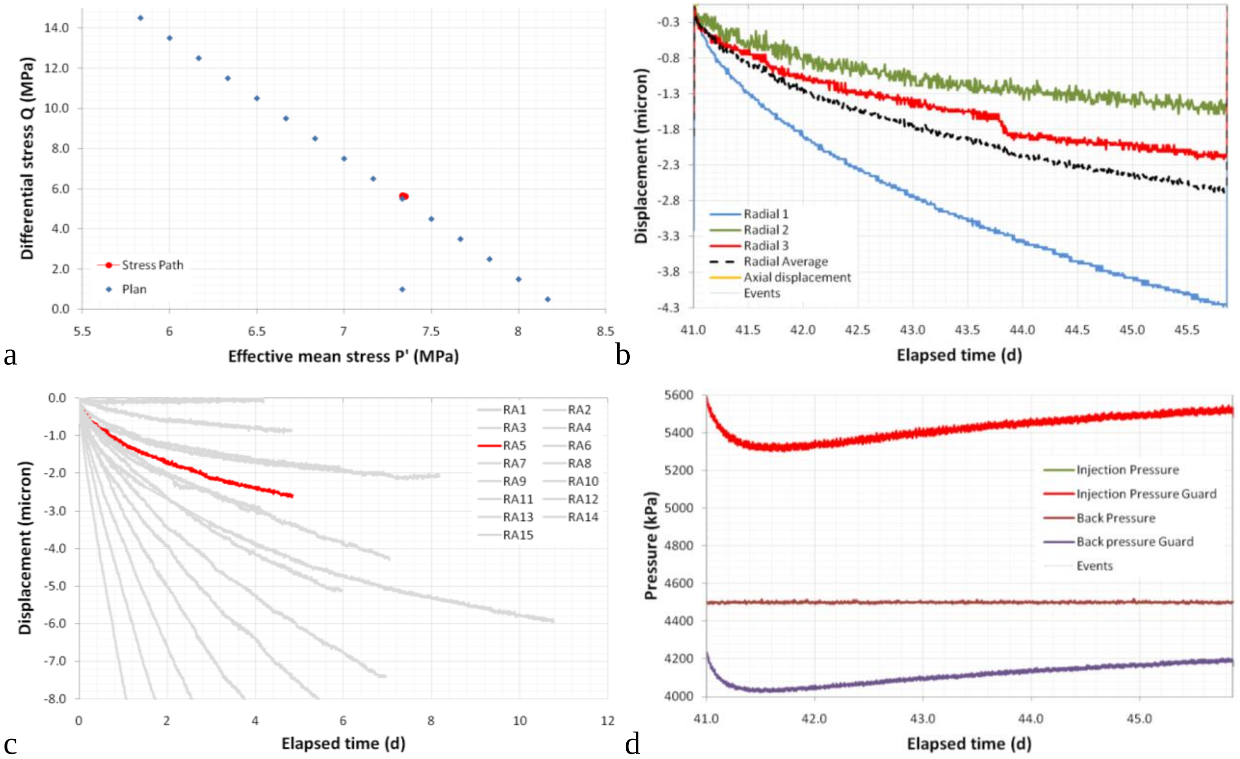

Figure 3-16 Results for step 6 of test SPP_COx-1. A). Location of the stress-path. B) Radial displacement results. C) Average radial displacement in comparison to other test steps. D) Evolution of porewater pressure in the guard-ring assembly.

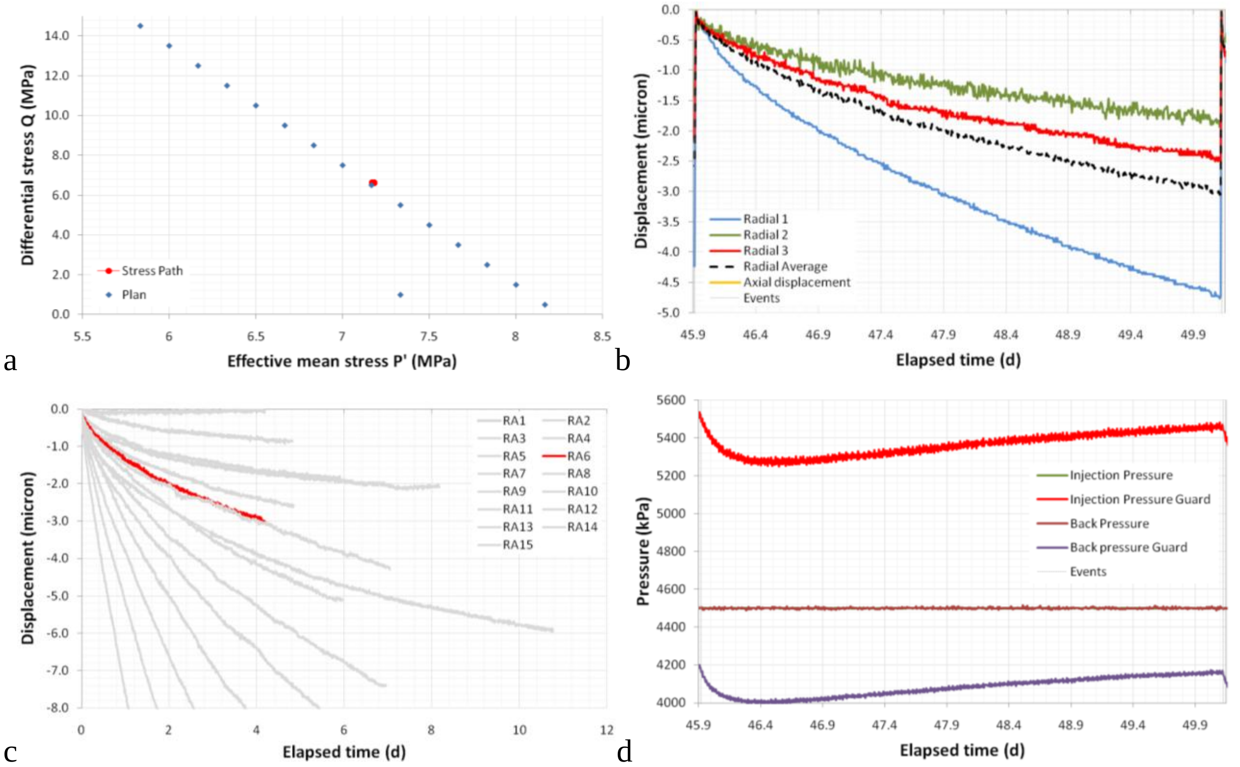

Figure 3-17 Results for step 7 of test SPP_COx-1. A). Location of the stress-path. B) Radial displacement results. C) Average radial displacement in comparison to other test steps. D) Evolution of porewater pressure in the guard-ring assembly.

3.3.7 Step 7; Day 45.9 – 50.1; σ_1 = 16.0 MPa, $\sigma_{2,3}$ = 9.5 MPa

The seventh stage was approximately 4 days long and the results are shown in Figure 3-17. It can be seen that no stepped changes in radial 3 occurred, but anisotropy had continued in radial displacement (see Figure 3-17b) with 4.7, 2.5 and 1.9 µm of displacement in radial 1, 3, and 2 respectively. Figure 3-17c shows that step 7 had an increased slope compared to step 6. The evolution of porewater pressure showed similar results to the previous steps, with 200 kPa loss in back-pressure and 300 kPa in injection pressure (Figure 3-17d). At the end of the stage the porewater pressure had still not recovered and was approximately 50 kPa lower than when the step began.

3.3.8 Step 8; Day 50.1 – 60.9; σ_1 = 16.5 MPa, $\sigma_{2,3}$ = 9.0 MPa

The eighth stage was approximately 11 days long and the results are shown in Figure 3-18. This step was prolonged so that full asymptote and steady-state was achieved. However, as the results show even after 11 days the sample was far from reaching steady-state. As seen in Figure 3-18 there was a problem with the logging computer which failed to log data for approximately two days; this had no effect on the experiment and was just a loss of data logging. Figure 3-18b shows that the sample showed time-dependency in radial displacement and considerable anisotropy, with 9.5, 4.8 and 3.4 µm of displacement in Radial 1, 3 and 2 respectively. Figure 3-18c shows that the curvature of time-dependency for step 8 had increased since step 7 and that symptote has not been achieved, and would not be reached within 5 – 7 days. Figure 3-18d shows the evolution of porewater pressure in the guard-rings. Common to the previous steps a 200 kPa drop was seen within 0.5 days, followed by a slow recovery. As this step was much longer than the previous step the pore-pressure at the end of the step is greater than at the start in both injection and back-pressure guard-rings. This highlights that in previous steps the failure to reach asymptote resulted in only partial recovery of pressure in the guard-ring.

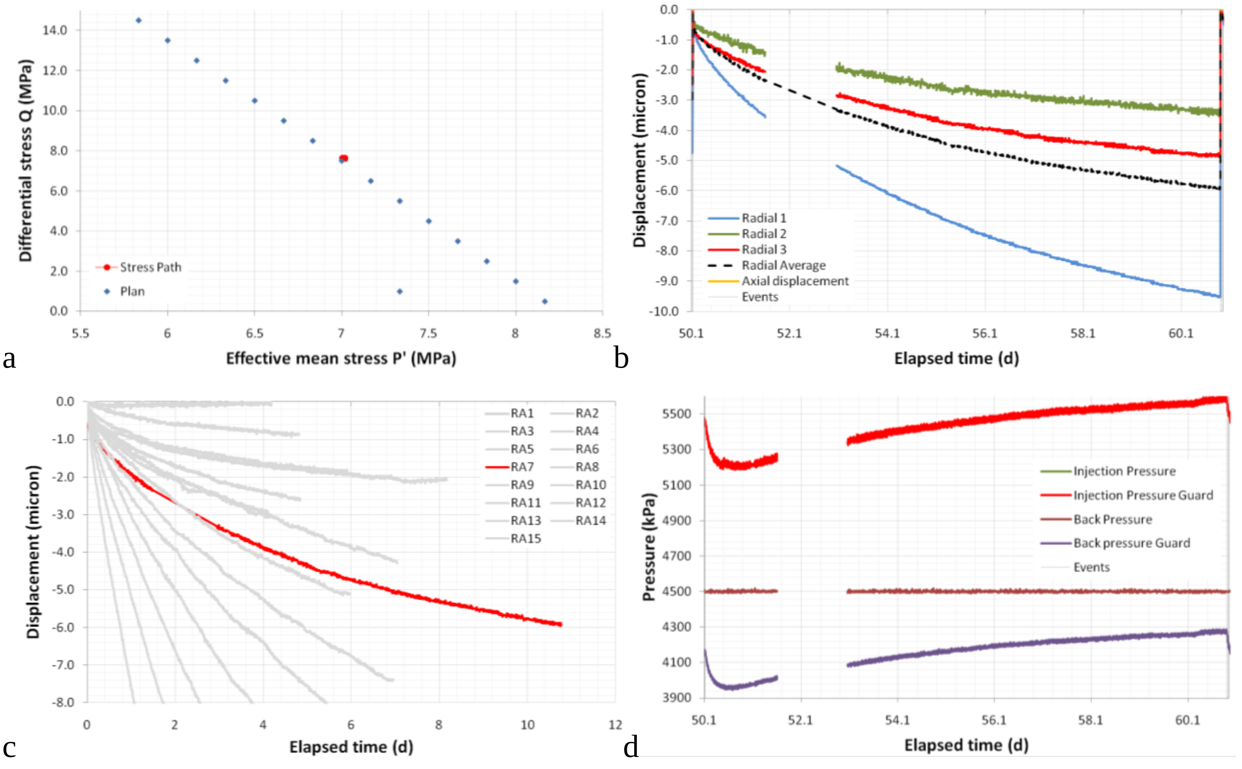

Figure 3-18 Results for step 8 of test SPP_COx-1. A). Location of the stress-path. B) Radial displacement results. C) Average radial displacement in comparison to other test steps. D) Evolution of porewater pressure in the guard-ring assembly.

3.3.9 Step 9; Day 60.9 – 67.9; σ_1 = 17.0 MPa, $\sigma_{2,3}$ = 8.5 MPa

The nineth stage was approximately 7 days long and the results are shown in Figure 3-19. The data for step 9 when compared to the previous steps shows much less stability following a temperature spike of 1° C at Day 63.1. The variation in temperature of the pressure vessel has influenced many of the recorded channels. The temperature spike had effected the radial displacement readings. It is noted that Radial 1 showed a positive influence, but Radial 2 and 3 both show a negative spike (Figure 3-19b). Radial displacement had not reached asymptote by the end of the step and showed anisotropy. Radial 1, 2 and 3 showed 7.1, 2.3, and 3.5 μm of displacement respectively. Figure 3-19c shows that the curvature of the time-dependent displacement had reduced following the extended operation of the previous step. The curvature had resulted in the same level as step 7.

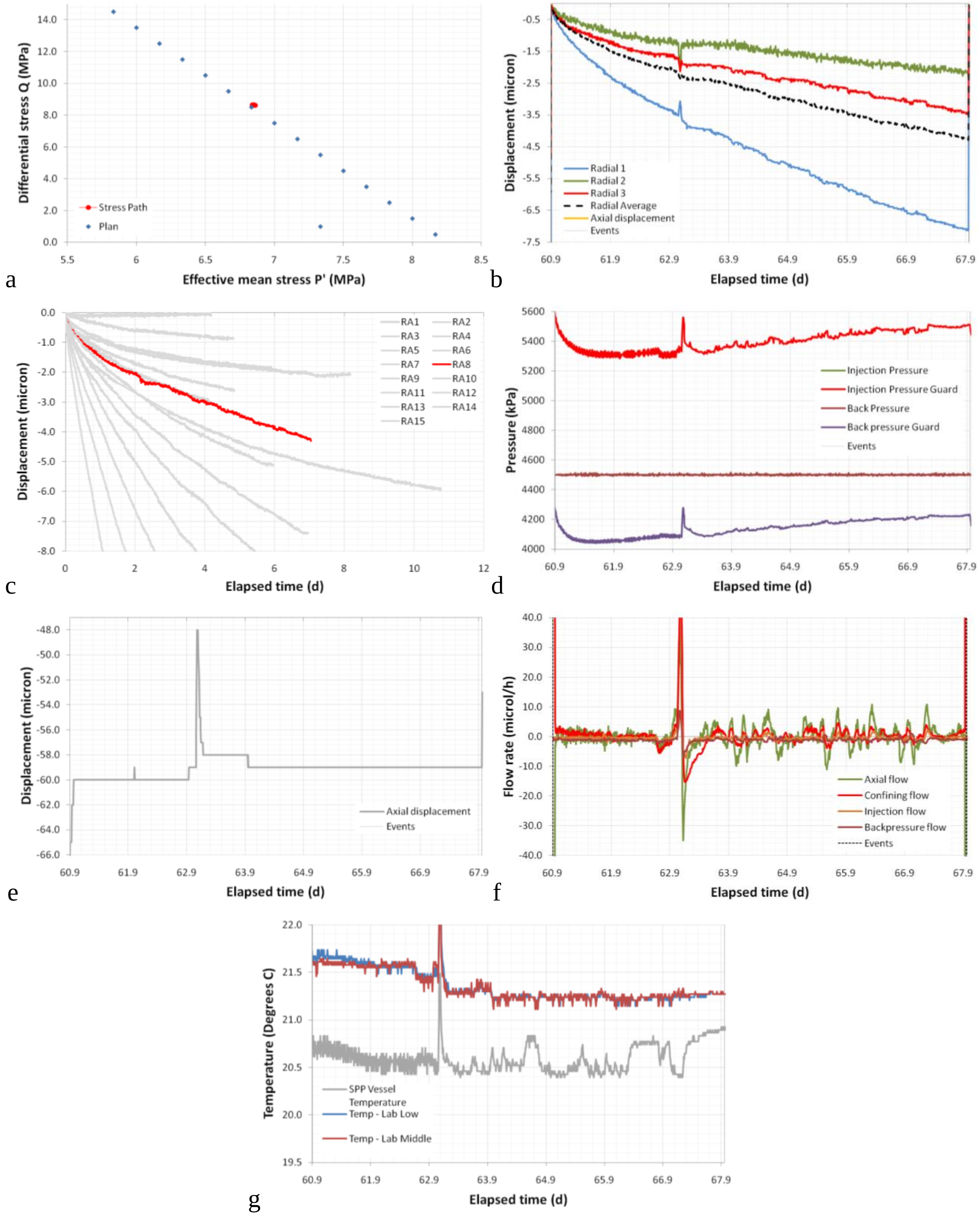

Figure 3-19 Results for step 9 of test SPP_COx-1. A). Location of the stress-path. B) Radial displacement results. C) Average radial displacement in comparison to other test steps. D) Evolution of porewater pressure in the guard-ring assembly. E) Axial displacement. F) Flow rate of all four ISCO pumps. G). Laboratory temperature.

The evolution of porewater pressure in the guard-rings (Figure 3-19d) showed similar behaviour as the previous steps. A 200 kPa drop occurred in the first 0.5 days of the step, followed by a slow recovery. The pressure of the guard-rings was affected by the temperature disturbance and the result following this time was not as steady as previously achieved. Figure 3-19e and Figure 3-19f show the influence the temperature disturbance had on axial displacement and flow respectively.

3.3.10 Step 10; Day 67.9 – 73.9; σ_1 = 17.5 MPa, $\sigma_{2,3}$ = 8.0 MPa

The tenth stage was approximately 6 days long and the results are shown in Figure 3-20. All channels showed similar results to previous steps. Considerable anisotropy was seen in radial displacement with 8.1, 4.2 and 3.1 µm of displacement observed in Radial 1, 3 and 2 respectively. Figure 3-20c shows that the curvature of displacement for step 10 had increased in comparison with step 9. The evolution of porewater pressure in the guard-rings (Figure 3-20d) showed the characteristic pressure drop followed by pressure recovery. Figure 3-20e shows the result for laboratory temperature which showed instability in SPP vessel temperature. The variations in temperature correlate with disturbances seen in guard pressures and radial displacements.

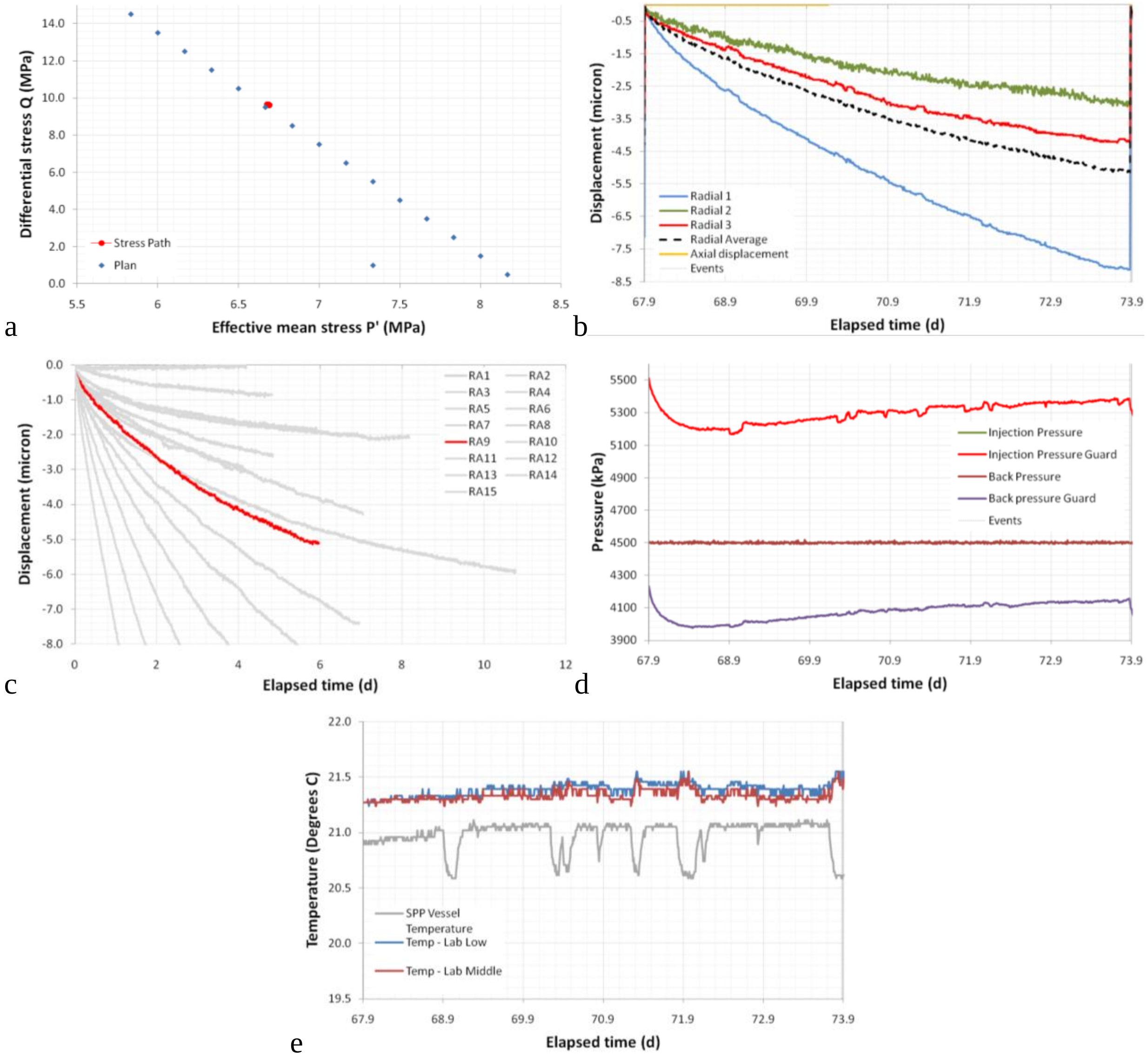

a b c d e

Figure 3-20 Results for step 10 of test SPP_COx-1. A). Location of the stress-path. B) Radial displacement results. C) Average radial displacement in comparison to other test steps. D) Evolution of porewater pressure in the guard-ring assembly. E) Temperature readings within the laboratory.

3.3.11 Step 11; Day 73.9 – 80.9; σ_1 = 18.0 MPa, $\sigma_{2,3}$ = 7.5 MPa

The eleventh stage was approximately 7 days long and the results are shown in Figure 3-21. All channels showed similar results to previous steps. Considerable anisotropy was seen in radial displacement with 11.7, 6.1 and 4.5 µm of displacement observed in Radial 1, 3 and 2 respectively (Figure 3-21b). Figure 3-21c shows that the curvature of displacement for step 11 had increased in comparison with step 10. The evolution of porewater pressure in the guard-rings (Figure 3-21d) showed the characteristic pressure drop followed by pressure recovery. As with previous steps, the porewater pressure had not fully recovered and had not reached asymptote.

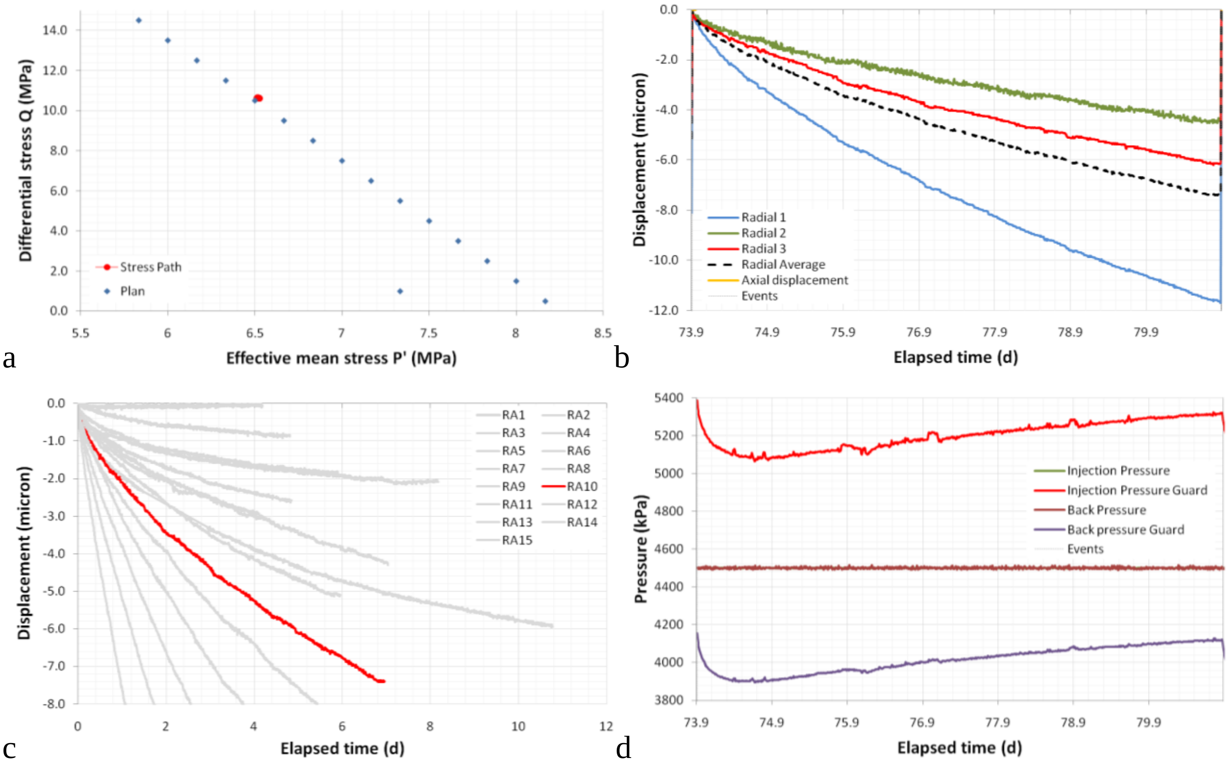

Figure 3-21 Results for step 11 of test SPP_COx-1. A). Location of the stress-path. B) Radial displacement results. C) Average radial displacement in comparison to other test steps. D) Evolution of porewater pressure in the guard-ring assembly.

3.3.12 Step 12; Day 80.9 – 88.0; σ_1 = 18.5 MPa, $\sigma_{2,3}$ = 7.0 MPa

The twelth stage was approximately 7 days long and the results are shown in Figure 3-22. All channels showed similar results to previous steps. Considerable anisotropy was seen in radial displacement with 14.5, 8.1 and 5.5 µm of displacement observed in Radial 1, 3 and 2 respectively (Figure 3-22b). Figure 3-22c shows that the curvature of displacement for step 12 had increased in comparison with step 11. The evolution of porewater pressure in the guard-rings (Figure 3-22d) showed the characteristic pressure drop followed by pressure recovery. As with previous steps, the porewater pressure had not fully recovered and had not reached asymptote.

3.3.13 Step 13; Day 88.0 – 94.9; σ_1 = 19.0 MPa, $\sigma_{2,3}$ = 6.5 MPa

The thirteenth stage was approximately 7 days long and the results are shown in Figure 3-23. All channels showed similar results to previous steps. Considerable anisotropy was seen in radial displacement with 18.5, 10.4 and 8 µm of displacement observed in Radial 1, 3 and 2 respectively (Figure 3-23b). Figure 3-23c shows that the curvature of displacement for step 13 had increased in comparison with step 12. The evolution of porewater pressure in the guard-rings (Figure 3-23d) showed the characteristic pressure drop followed by pressure recovery. As with previous steps, the porewater pressure had not fully recovered and had not reached asymptote.

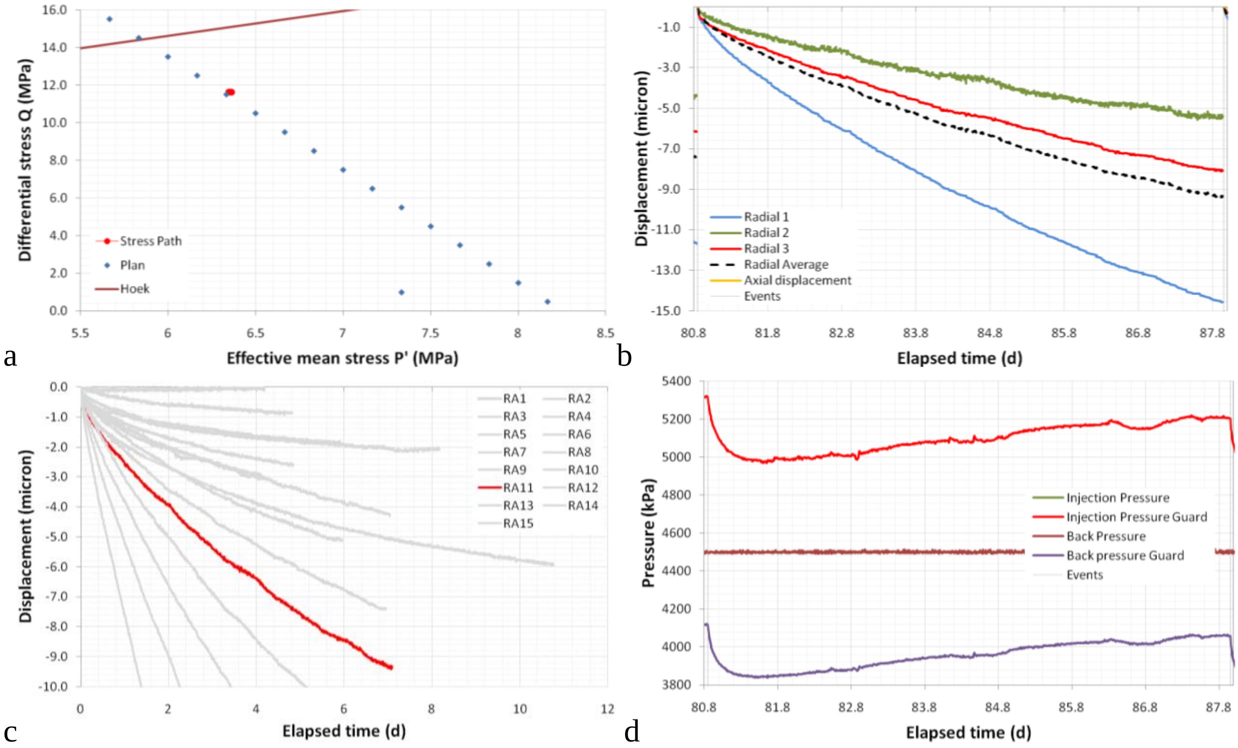

Figure 3-22 Results for step 12 of test SPP_COx-1. A). Location of the stress-path. B) Radial displacement results. C) Average radial displacement in comparison to other test steps. D) Evolution of porewater pressure in the guard-ring assembly.

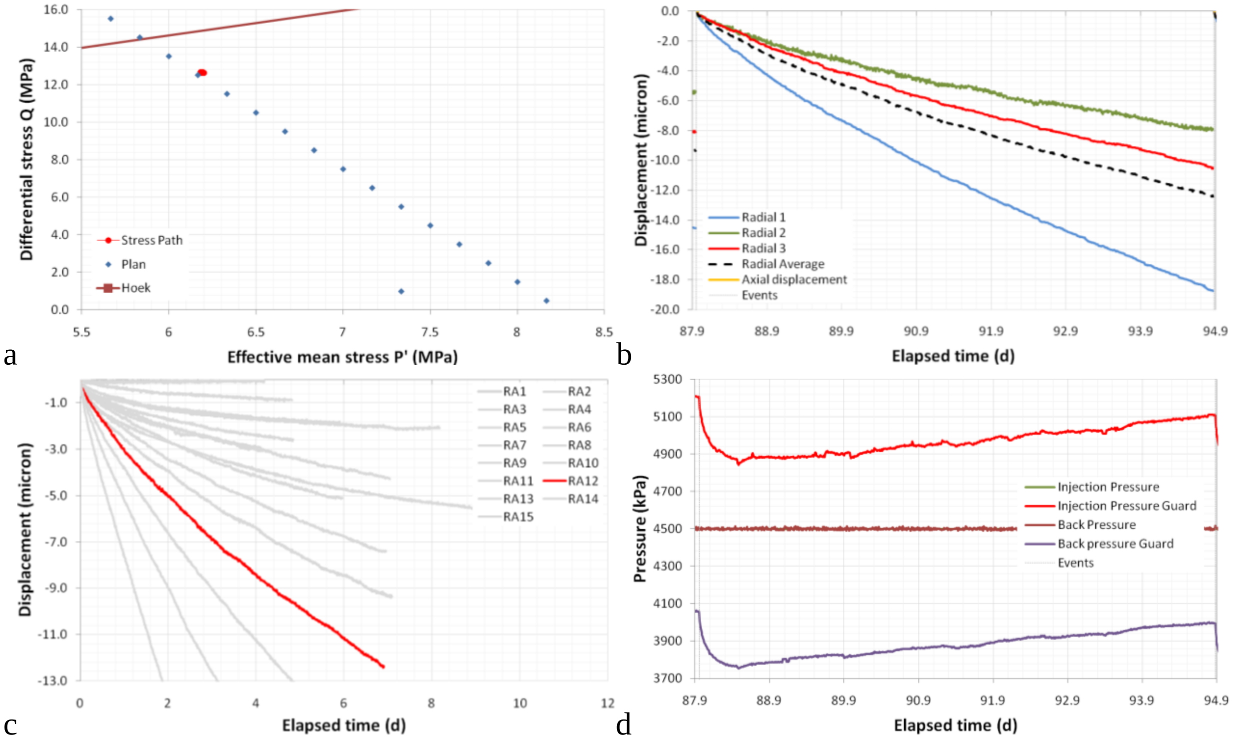

Figure 3-23 Results for step 13 of test SPP_COx-1. A). Location of the stress-path. B) Radial displacement results. C) Average radial displacement in comparison to other test steps. D) Evolution of porewater pressure in the guard-ring assembly.

3.3.14 Step 14; Day 94.9 – 101.9; σ_1 = 19.5 MPa, $\sigma_{2,3}$ = 6.0 MPa

The fourteenth stage was approximately 7 days long and the results are shown in Figure 3-24. All channels showed similar results to previous steps. Considerable anisotropy was seen in radial displacement with 25.5, 14.1 and 11 µm of displacement observed in Radial 1, 3 and 2 respectively (Figure 3-24b). Figure 3-24c shows that the curvature of displacement for step 14 had increased in comparison with step 13. The evolution of porewater pressure in the guard-rings (Figure 3-24d) showed the characteristic pressure drop followed by pressure recovery. As with previous steps, the porewater pressure had not fully recovered and had not reached asymptote.

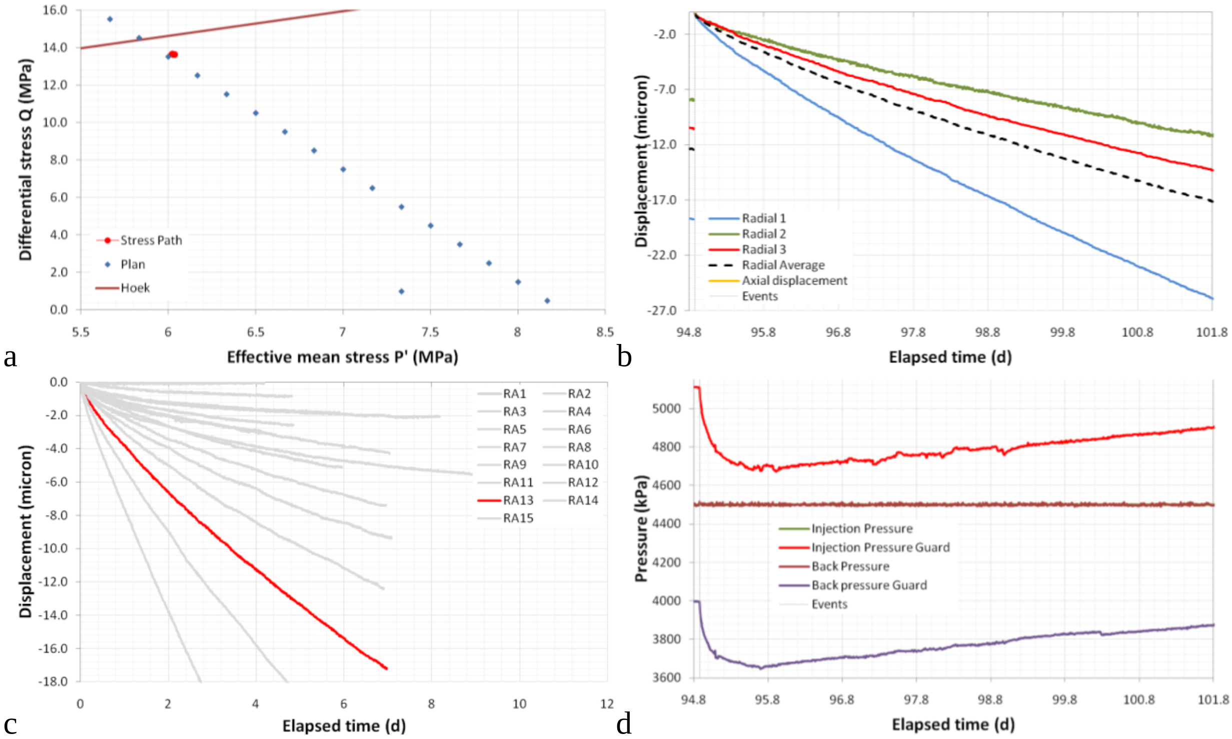

Figure 3-24 Results for step 14 of test SPP_COx-1. A). Location of the stress-path. B) Radial displacement results. C) Average radial displacement in comparison to other test steps. D) Evolution of porewater pressure in the guard-ring assembly.

3.3.15 Step 15; Day 101.9 – 108.9; σ_1 = 20.0 MPa, $\sigma_{2,3}$ = 5.5 MPa

The fifteenth stage was approximately 7 days long and the results are shown in Figure 3-25. All channels showed similar results to previous steps. Considerable anisotropy was seen in radial displacement with 36.4, 21.1 and 16.5 µm of displacement observed in Radial 1, 3 and 2 respectively and 36 µm of displacement seen in axial displacement (Figure 3-25b). Figure 3-25c shows that the curvature of displacement for step 15 had increased in comparison with step 14. The evolution of porewater pressure in the guard-rings (Figure 3-25d) showed the characteristic pressure drop followed by pressure recovery. As with previous steps, the porewater pressure had not fully recovered and had not reached asymptote. After Day 107.3 the pressure response in the pressure guard changed characteristic with high frequency oscillations, this may have been in response to 0.3° C oscillations observed in the temperature of the pressure vessel. However, the frequency of the pressure oscillations was much higher than that seen in the temperature.

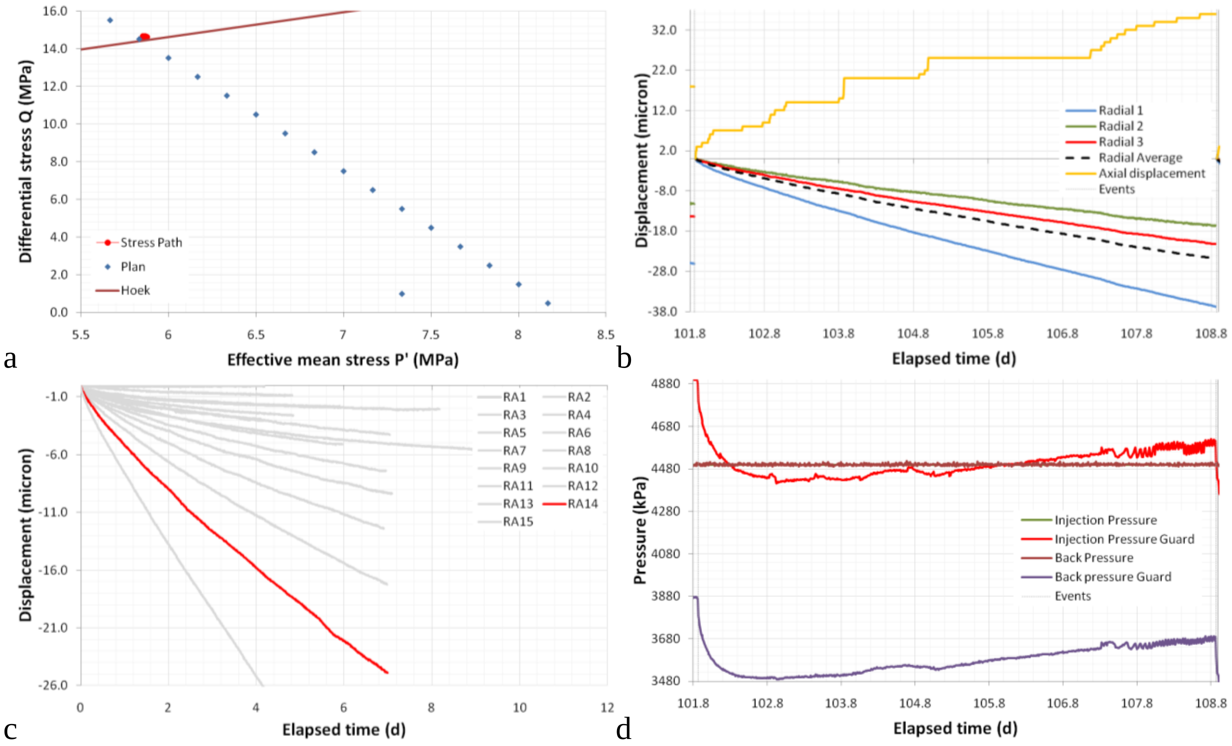

Figure 3-25 Results for step 15 of test SPP_COx-1. A). Location of the stress-path. B) Axial and radial displacement results. C) Average radial displacement in comparison to other test steps. D) Evolution of porewater pressure in the guard-ring assembly.

3.3.16 Step 16; Day 108.9 – 123.2; σ_1 = 20.5 MPa, $\sigma_{2,3}$ = 5.0 MPa

The sixteenth and final stage was approximately 14 days long and the results are shown in Figure 3-26. It can be seen that up to Day 114 the deformation response was similar to previous steps. Considerable anisotropy was seen in radial displacement with 43, 31.4 and 21.8 µm of displacement observed in Radial 1, 3 and 2 respectively and 64 µm of displacement seen in axial displacement at Day 114 (Figure 3-26b). After this time the deformation accellerated and by Day 114.5 all displacement sensors had reached their maximum displacement. Figure 3-26c shows that the curvature of displacement for step 16 had increased in comparison with step 15. The evolution of porewater pressure in the guard-rings (Figure 3-26) showed the characteristic pressure drop; However this was followed by a plateau in pressure, with pressure reducing as the deformation accellerated. Figure 3-26e shows the response recorded in the injection load cell. As displacement started to accellerate the load increased. At the point of sample failure the load reduced and quickly rose again and reached a peak. At this point the hydraulic ram stopped and the response after this time was the slow reduction of load as a result of creep along the formed fracture.

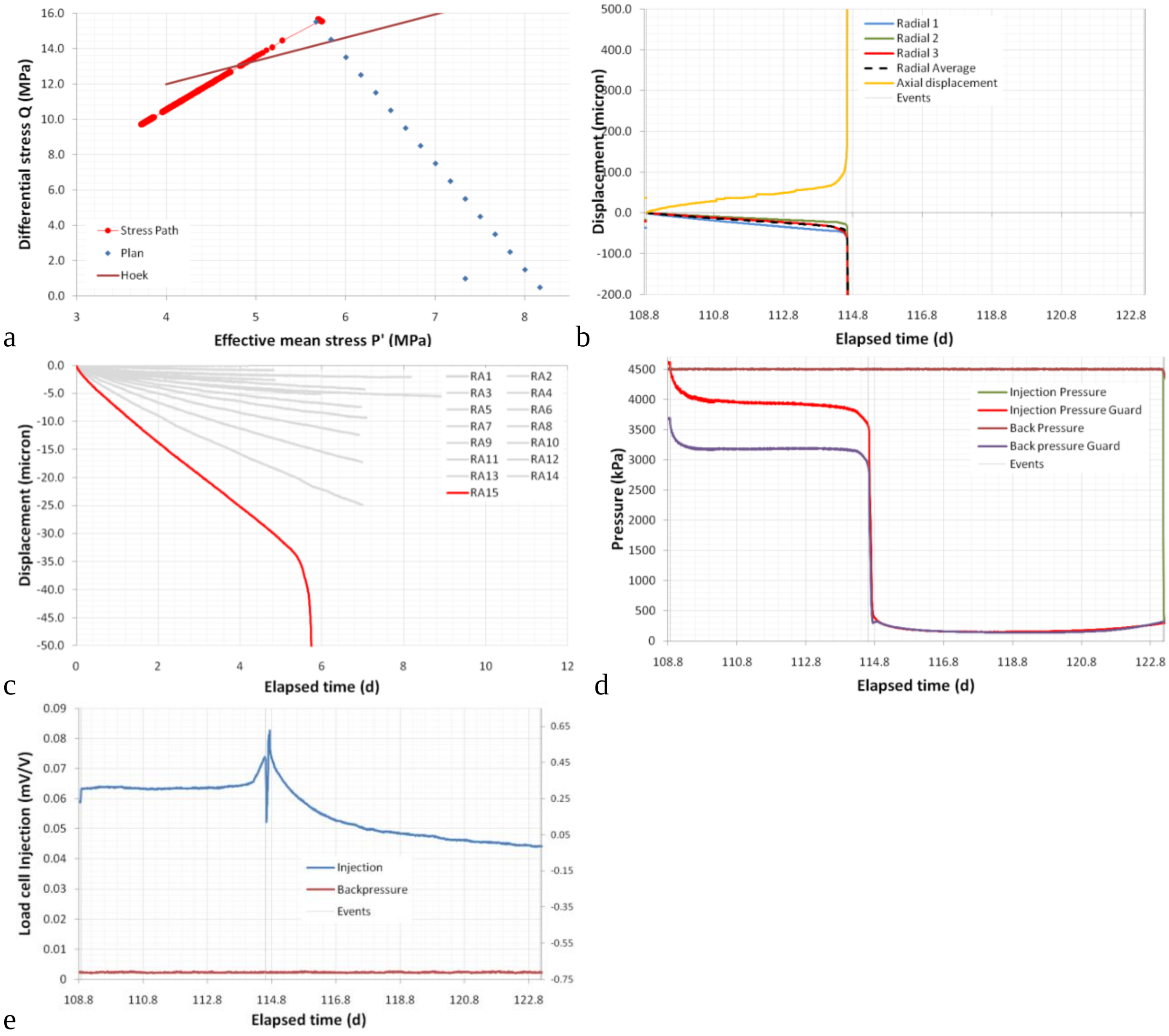

Figure 3-26 Results for step 16 of test SPP_COx-1. A). Location of the stress-path. B) Axial and radial displacement results. C) Average radial displacement in comparison to other test steps. D) Evolution of porewater pressure in the guard-ring assembly. E) Axial load recorded at the end of the test sample during deformation.

3.3.17 Step 16 up to failure; Day 108.9 – 114.6; $\sigma_1 = 20.5$ MPa, $\sigma_{2,3} = 5.0$ MPa

Figure 3-27 shows in detail the 5.5 days of results up to the point of sample failure for stage 16. Considerable anisotropy was seen in radial displacement with 43, 31.4 and 21.8 µm of displacement observed in Radial 1, 3 and 2 respectively (Figure 3-27a) and 64 µm of displacement seen in axial displacement at Day 114 (Figure 3-27b). After this time the deformation accellerated; it can be seen that axial displacement showed the first increase in deformation rate, soon followed by radial 3. By Day 114.5 all displacement sensors had reached their maximum displacement. The evolution of porewater pressure in the guard-rings (Figure 3-27c) showed the characteristic pressure drop; However this was followed by a plateau in pressure, with pressure reducing as the deformation accellerated. Figure 3-27d shows the response recorded in the injection load cell. As displacement started to accellerate the load at this location increased, posibly as a result in the reduction of pore-pressure. At the point of sample failure the load reduced and quickly rose again and reached a peak. At this point the hydraulic ram stopped and the response after this time was the slow reduction of load as a result of creep along the formed fracture. Figure 3-27e shows the flows recorded by the pumps. At the onset of deformation the axial and confining pumps could be seen to increase in flow in order to maintain constant axial load and confining pressure. No marked change in flow of pore fluid was seen at either the injection or back-pressure sides.

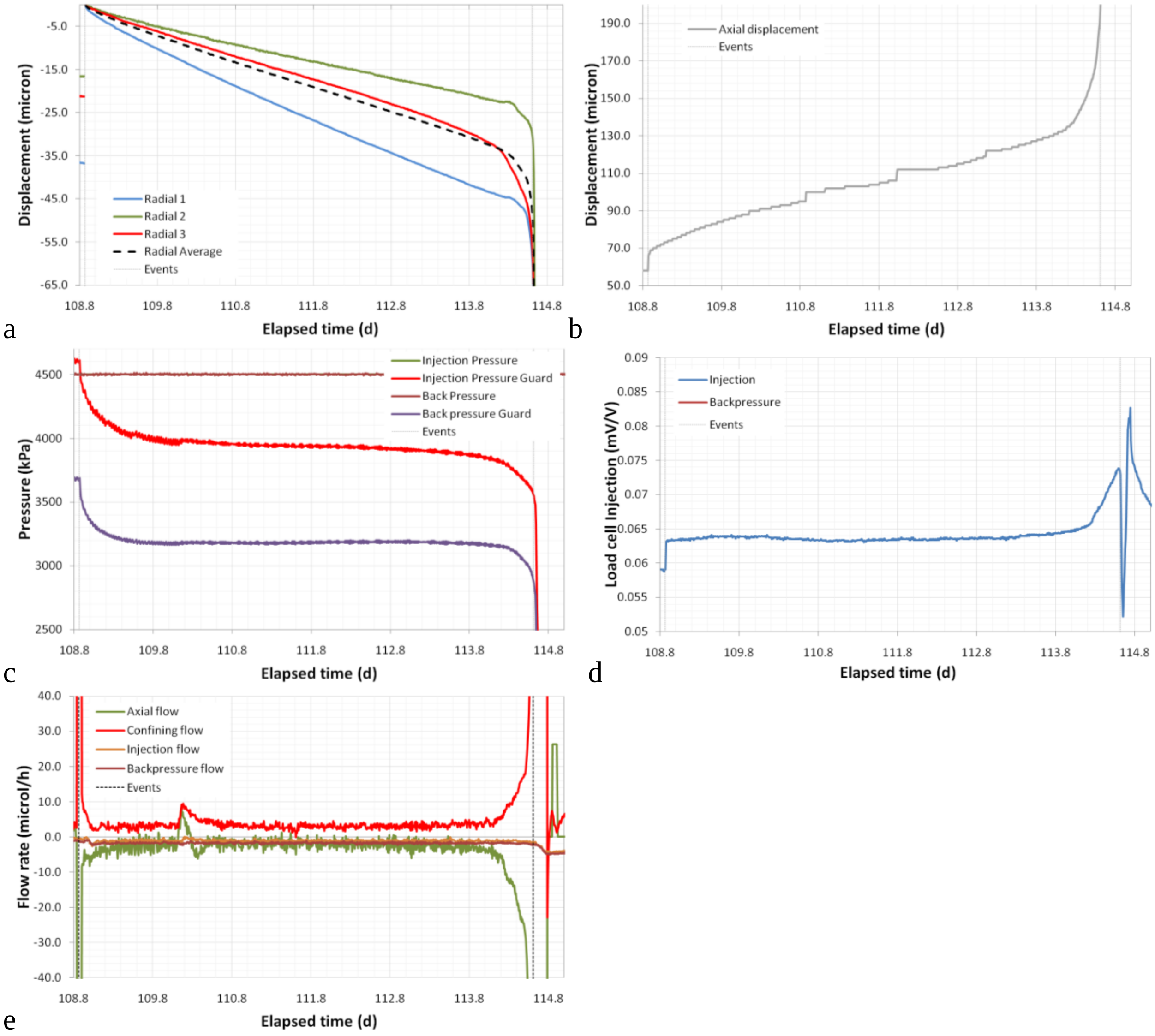

Figure 3-27 Results for step 16 of test SPP_COx-1 up to the point of sample failure. A). Radial displacement results. B) Axial displacement results. C) Evolution of porewater pressure in the guard-ring assembly. E) Axial load recorded at the end of the test sample during deformation.

3.3.18 Step 16 post failure; Day 114.6 – 123.2; $\sigma_1 = 20.5$ MPa, $\sigma_{2,3} = 5.0$ MPa

Considerable changes were seen after sample failure. At the point of failure the axial ram was advanced by the ISCO pump operating at constant pressure. Once the full stroke of the pump had been achieved the axial system stopped and the sample slowly reacted to the constant strain and confining pressure. Pore-pressure was continued at constant pressure of 4.5 MPa.

As seen in Figure 3-28a, the axial load on the sample reduced slowly with time from 20.6 MPa to 14.7 MPa over nearly 9 days. This resulted in the stress-path modifying as seen in Figure 3-28b. The slow reduction in load was also shown in the load cell at the injection end of the sample, as seen in Figure 3-28c. This showed that slow creep was occuring. This could possibly be through time-dependent volumetric strain, but was likely to be slow creep along the formed fracture surface. Figure 3-28d shows the change in volume of the confining pressure system and was an indicator of volumetric strain of the sample; suggesting that the sample underwent time-dependent volumetric strain.

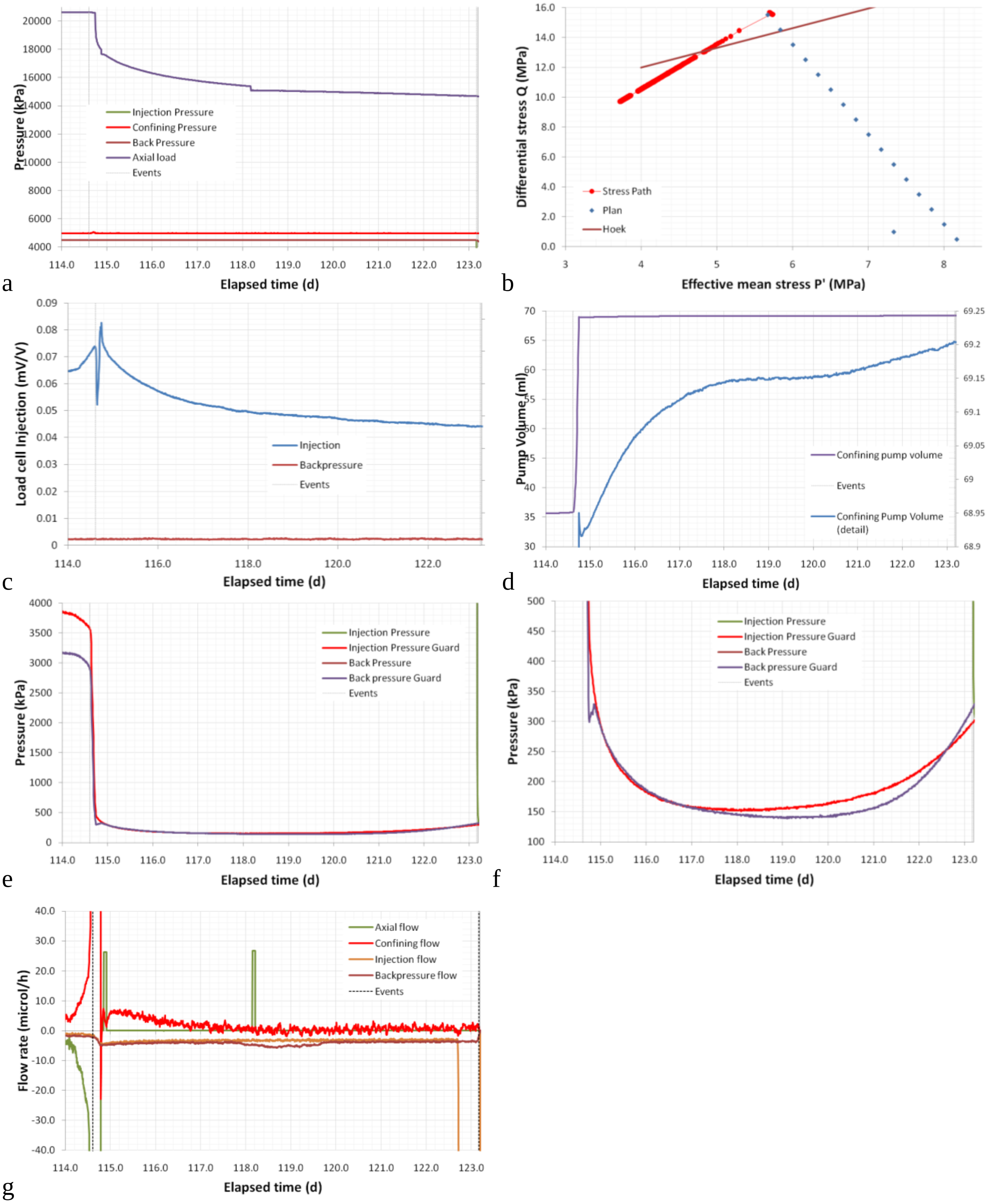

Figure 3-28 Results for step 16 of test SPP_COx-1 after the sample had failed. A). Axial load on the sample can be seen to reduce once the axial ram had stopped. B). Location of the stress-path. C). Slow reduction in load recorded on the injection platen. D). Change in volume of the confining pressure system suggesting volumetric creep of the sample. E) and F). Pore-pressure measured in guard-rings at both end of the samples. G). Flow rate as measured by the four ISCO pumps that operate the SPP.

Figure 3-28e and f show the change in pore-pressure as measured at the guard-rings. The onset of failure saw the pressure at these points reduce and rapidly drop as the sample failed. However, it can be seen that the initial drop of 3-4 MPa was followed by a slow decrease, with a minimum pressure achieved in 2.5 and 5.5 days for the injection and back-pressure guard-rings respectively. Unexpectadely it can be seen that pore-pressure at the guard-ring started to rise after reaching minimum. The injection guard-ring reached a minimum of 145 MPa and recovered to 295 MPa by the end of the experiment. The back-pressure guard-ring reached a minimum of 140 MPa and recovered to 325 MPa at the end of the test. Sadly there was not time to continue the experiment, therefore it is not known how much pressure would have recovered. The initial drop in pressure was likely to be the result of the dilatancy created by the fracture/fault running through the sample. The pore fluid at the guard-rings drained into this increased porosity network resulting in a reduction in pore-pressure. This effect was very localised as there was not a significant increase in flow at the nearby injection and back-pressure filters (Figure 3-28g). The flow into the formed fault zone resulted in a highly anisotropic pore-pressure distribution within the sample, which in time started to recover.

3.4 POST-TEST OBSERVATIONS

The stress-path permeameter (SPP) apparatus was designed with a 56 mm diameter end that should allow samples to be loaded and removed without the dismantling of the apparatus. However, considerable strain was experienced by the sample and it was not possible to extract the sample from the apparatus without loosening the tie-rods and dismantling the apparatus. On removing the sample it was evident that it had undergone considerable deformation (see Figure 3-29a).

The Hoek sleeve that jacketed the test sample within the apparatus did not split and accommodated considerable deformation. The test sample can be seen to have deformed through the formation of a fracture/fault oriented approximately 30° to the length of the sample. It is observed that this fracture appeared to intersect both corners of the sample (Figure 3-29b and c) and this may be the result of edge effects created by friction acting along the ends of the sample between rock and steel platten. On closer inspection a series of fractures parallel to the main fracture could be seen, as well as a series of conjugate fractures (see Figure 3-29d). This suggests that the deformation was complex.

The test sample was measured using the BGS built SHRINKiT (Hobbs *et al.*, 2010; Figure 3-30); an apparatus designed to measure soil shrinkage. The apparatus consisted of a rotating turntable, on which the test specimen was mounted, and a vertical height gauge, on which a laser rangefinder was mounted. Both are controlled by stepper motors. A third stepper motor operated a release mechanism to allow weighing of the specimen. The system effectively ‘scans’ the surface of the specimen allowing its co-ordinates to be accurately recorded, along with its weight. From this information the volume of the specimen can be determined, the accuracy being a function of the number of points measured. Test specimens in the diameter range 60mm to 100mm and the height range 60mm to 130mm may be tested; however the equipment worked successfully on the 56 mm diameter samples used in this experiment. The apparatus was able to measure up to 3,600 xyz points on the specimen’s surface. SHRINKiT works by measuring xyz along the length of the sample, the sample was then rotated and re-measured. For the test sample xyz data was recorded for 25 intervals along the sample length every 3° around the sample circumference. Due to limitations in rotation it was not possible to measure between 354 - 360°. Therefore SHRINKiT was able to measure 3,025 discrete xzy locations on the sample surface. The sample was also weighed by SHRINKiT.

The results from SHRINKiT are output as a text file, which was inported into Microsoft Excel and reformatted so as to plot the circumference of the sample at 25 intervals along the sample length, nine circumferences are shown in Figure 3-31. These plots show that for all 25 intervals the sample had increased in diameter. It is clear to see the fracture that runs through the sample and either side of this feature two circular samples are observed, as expected.

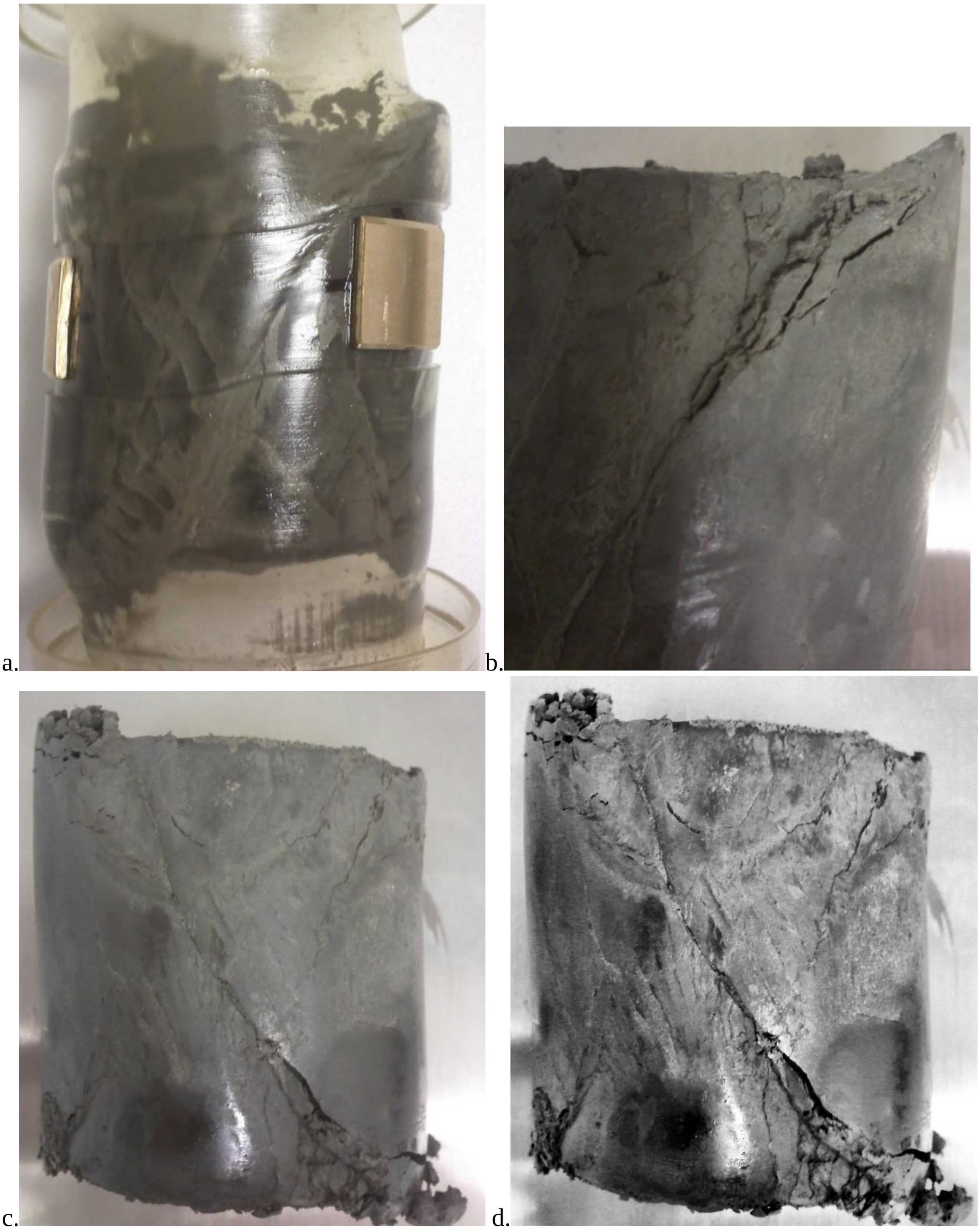

Figure 3-29 Post-test photos of test sample SPP_COx-1. A). Jacketed sample, showing considerable deformation. B) Detail of the fracture, clearly showing that the formed fracture intersected the corner of the sample. C) Photograph of the entire test sample clearly showing the main fracture surface. D) Enhanced image of photo (c) clearly showing a series of parallel features on the sample surface and a conjugate series of fractures.

Figure 3-30 The automated SHRINKiT, shrinkage limit apparatus.

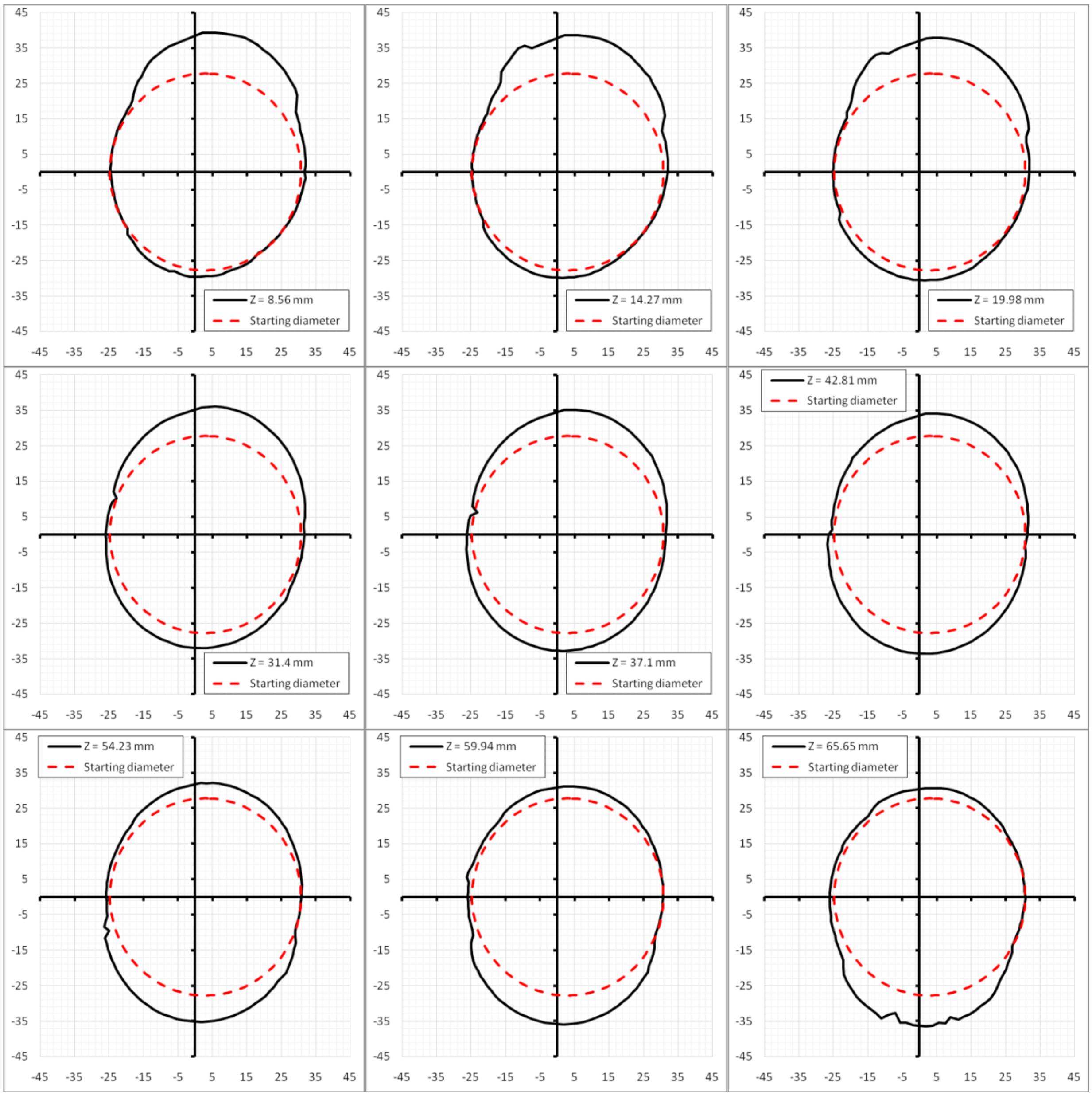

Figure 3-31 Results from SHRINKiT giving the dimensions of the final sample at 25 different levels through the sample (9 shown). Elevation of Z = 0 was the top of the sample. These plots show the deformation at each level when compared with the size of the starting material.

4 Test SPP_COx-2 (gas flow test)

4.1 COMPLETE TEST HISTORY

Test SPP_COx-2 lasted a total of 566 days, with Figure 4-1 showing the test result data for the complete test history and Table 4-6 summarising the individual test stages. The four stages of the test can be seen (initial swelling stage, equilibration at *in situ* conditions, hydraulic testing and gas injection testing). The gas injection testing can be further split into stages of (i) gas flow initiation, (ii) gas flow shut-off, (iii) attempted gas flow re-initiation by raising injection pressure, and (iv) attempted gas flow re-initiation by lowering back-pressure. Results for each section are introduced in the following sections.

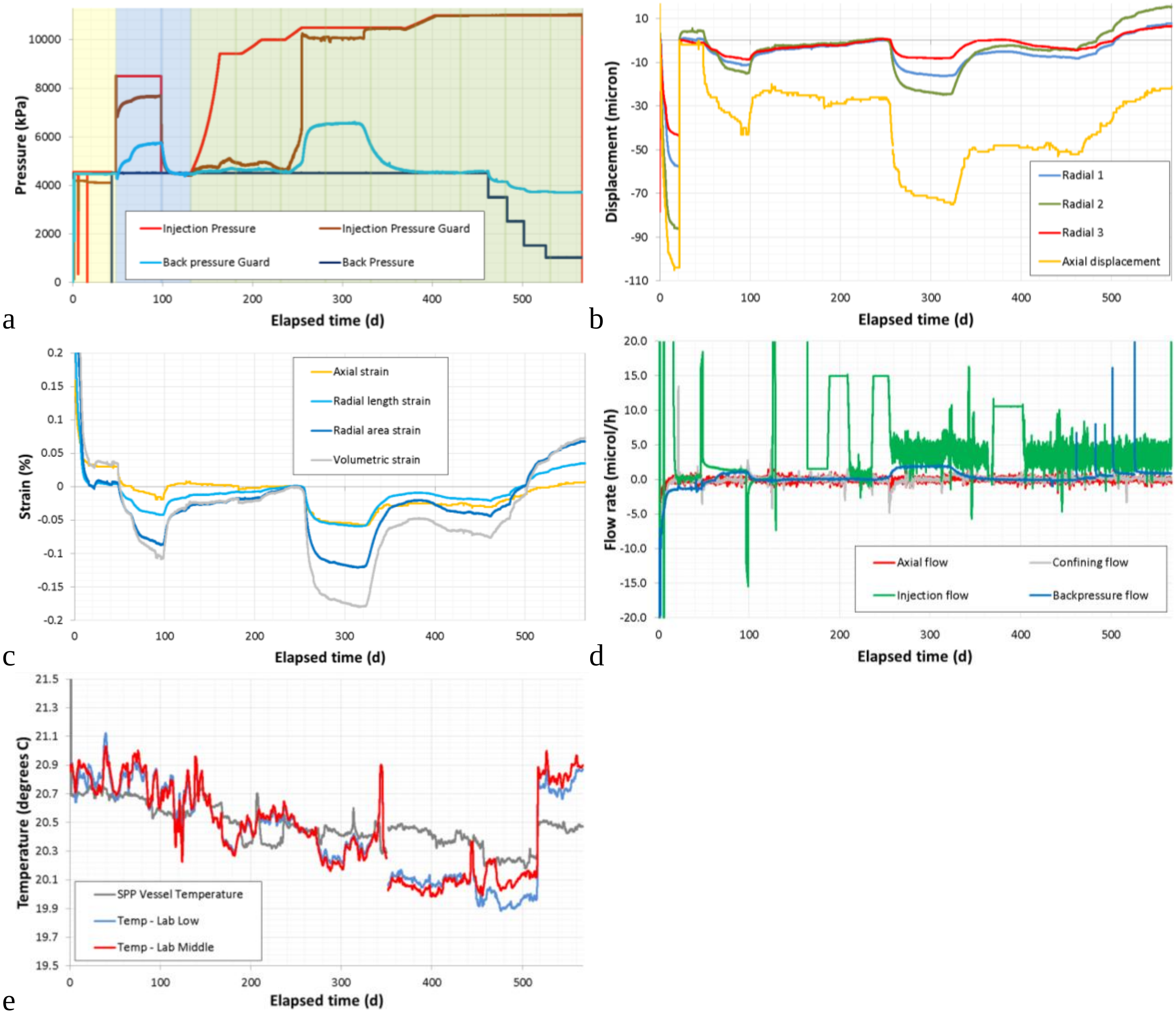

a b c d e

Figure 4-1 Data for the complete test history of test SPP_COx-2. A) Pressure history, b) radial and axial displacement, c) sample strain, d) flow data and e) temperature.

Stage	Description	Axial stress (MPa)	Confining stress (MPa)	Injection pore-pressure (MPa)	Back pore-pressure (MPa)	Test time at start (days)	Length of stage (days)
1	Saturation and swelling	12.5	11.5	4.5	4.5	0.1	21.7
2	Equilibration	13.0	12.5	4.5	4.5	21.8	26.1
3a	Hydraulic testing	13.0	12.5	8.5	4.5	47.9	50.1
3b	Hydraulic testing	13.0	12.5	4.5	4.5	98.0	29
4a	Gas injection ramp (constant flow)	13.0	12.5	4.5 – 9.5	4.5	127.0	35.3
4b	Gas injection at constant pressure	13.0	12.5	9.5	4.5	162.3	25.5
4c	Gas injection ramp (constant flow)	13.0	12.5	9.5 – 10.0	4.5	187.8	22.2
4d	Gas injection at constant pressure	13.0	12.5	10.0	4.5	210.0	26.1
4e	Gas injection ramp (constant flow)	13.0	12.5	10.0 – 10.5	4.5	236.1	18.9
4f	Gas injection at constant pressure	13.0	12.5	10.5	4.5	255.0	~65
4g	Gas shut-off	13.0	12.5	10.5	4.5	~320	~49
4h	Gas injection ramp (constant flow)	13.0	12.5	10.5 – 11.0	4.5	368.8	34.3
4i	Gas injection at constant pressure	13.0	12.5	11.0	4.5	403.1	58.8
4j	Lowering of back-pressure step 1	13.0	12.5	11.0	3.5	461.9	21.1
4k	Lowering of back-pressure step 2	13.0	12.5	11.0	2.5	483.0	18.8
4l	Lowering of back-pressure step 3	13.0	12.5	11.0	1.5	501.8	24.2
4m	Lowering of back-pressure step 4	13.0	12.5	11.0	1.0	526.0	40.8
End	Test end	0	0	0	0	566.8	/

Table 4-6 Summary of experimental history showing stage number, description of stage, axial stress and confining stress.

4.2 SWELLING HISTORY

The first stage of testing imposed stress conditions similar to the *in situ* conditions for the borehole the test sample was taken from (σ_1 = 13 MPa, σ_2 = σ_3 =12.5 MPa, P_p = 4.5 MPa). Chemically balanced water (see section 2.3) was injected at both ends of the sample in order to re-establish full sample saturation and to minimise chemically driven swelling of the sample. During extraction, storage and sample preparation the sample will have undergone small amounts of desaturation and this stage of the test counteracts this effect. During this initial resaturation stage, the inlet/outlet and guard-rings were used to hydrate the sample and ensured that the air content of all pipework and pressure transducers was negligible. A pore-pressure of 4.5 MPa was generated at both the injection and back-pressure ends of the sample and the swelling was observed for 21 days. The stress conditions were then altered to *in situ* conditions and the sample response was monitored for a further 26 days. The results are shown in Figure 4-2.

The initial strains were difficult to determine. The generation of confining pressure resulted in the closure of the Hoek sleeve around the sample onto the sample face. This appeared as a large strain which may not be representative of the true deformation of the sample. Therefore the “initial” displacement recorded by the radial strain measurement devices has been removed.

Initially about 0.11 % volumetric strain was generated by the imposition of stress. The generation of pore-pressure and rehydration of the sample resulted in approximately 0.12 % dilational volumetric strain. By Day 21 this swelling strain had equilibrated.

Injection flow in the first 15 days of testing was seen to be considerably high compared with the back-pressure flow. Both pressure systems were at 4.5 MPa and so there was no reason for flow to be initiated. Several pressure couplings on the experimental apparatus were tightened and flow reduced to an almost zero flow condition; therefore this high flux can be attributed to leakages in the system. This is problematic in terms of mass balance and the exact amount of water injected into the sample is not known.

On Day 21 the stress conditions were altered to be that of the *in situ* stress state. As can be seen in Figure 4-2b one radial strain (Radial 2) showed contraction, whilst the other two showed no effect on changing stress state. By the end of the stage the sample had equilibrated with low flow rates being recorded and no significant time-dependent deformation.

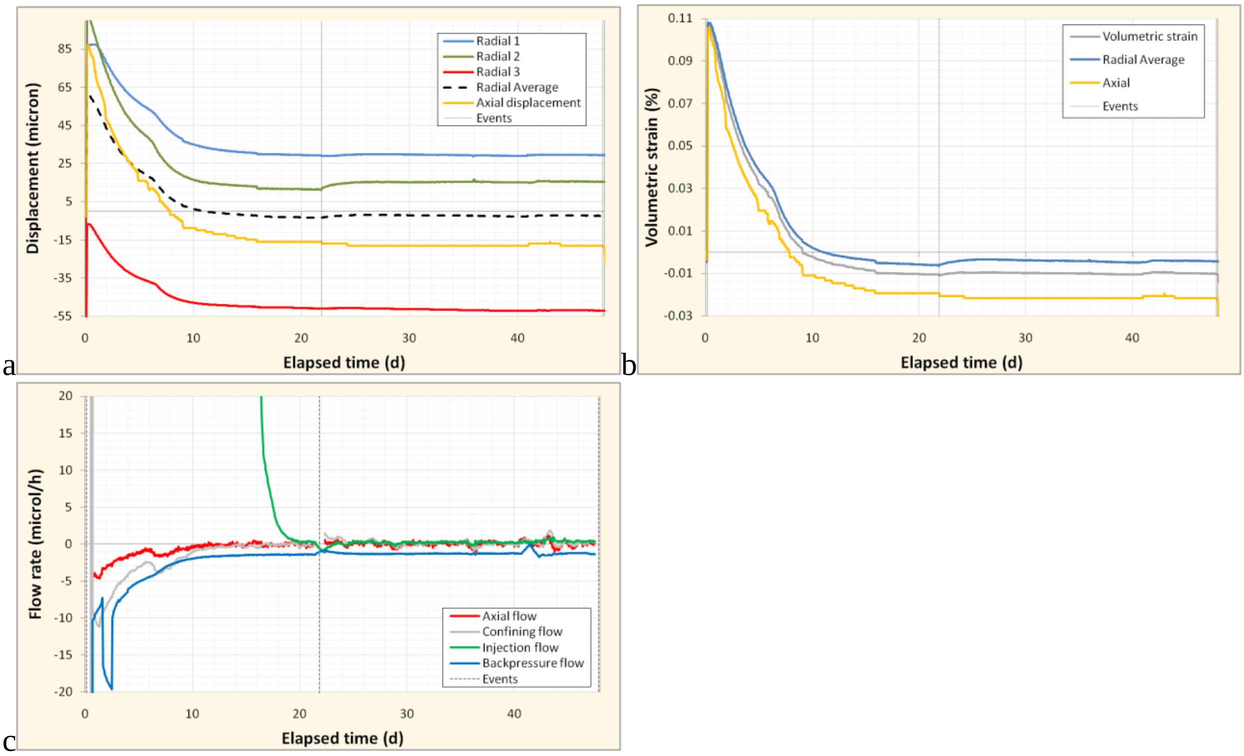

Figure 4-2 Data for the initial swelling stage of the test history. A) radial and axial displacement, b) sample strain, and c) flow data.

4.3 HYDRAULIC TWO-STAGE CONSTANT HEAD TEST

Following the swelling stage a two-stage constant head test was conducted, as shown in Figure 4-3. At the start of this test stage the injection pore-pressure was raised to 8.5 MPa and the guard-rings were isolated. Both injection (IGR) and back-pressure (BGR) end guard-rings showed an initial decrease in pore-pressure, which within a couple of days started to recover in pressure and equilibrated. The injection end stabilised approximately 1 MPa below the injection pressure, whereas the back-pressure was about 0.5 MPa above the back-pressure.

The raising of injection pressure to 8.5 MPa can be seen to induce dilational strain (radially, axially and volumetrically).

Flow data (Figure 4-3d) shows that in the first 7 days of the hydraulic test the back-pressure flow equilibrated to a flow of approximately 0 µl.h^{-1}. On Day 62 the back-pressure flow started to increase, reaching a steady-state flow of approximately 1 µl.h^{-1} by Day 87. At the onset of flow out of the sample the dilational strain of the sample started to increase (radially, axially and volumetrically). Therefore as water started to flow out of the sample the bulk sample volume increased. The onset of flow resulted in an additional 0.015 % of volumetric strain being generated (approximately 30 µl volume). The onset of flow also resulted in the guard-ring pressure changing at both ends of the sample, with the back-pressure end having a larger increase of about 0.7 MPa. It is possible that prior to Day 62 there was a leak on the injection circuit and that this stopped. The achievement of steady-state flow of 0 µl.h^{-1} on the low pressure stage of the hydraulic test shows that no leakage was occurring later than Day 100.

Injection pore-pressure was lowered to 4.5 MPa on Day 98. Over the remaining 32 days of the low pressure constant head hydraulic test stage the strain was partially recovered. This is accompanied by the slow decrease in pore-pressure in the injection and back-pressure guard-rings. The injection guard-ring decreased much slower than the back-pressure guard-ring. By the end of this test stage an additional 0.014 % of dilational strain occurred to the sample. The difference in pore-pressure over a relatively small distance suggests a high pressure gradient of approximately 100 MPa.m^{-1}, which resulted in a flow of only 2.8 × 10-13 m^3.s^{-1}.

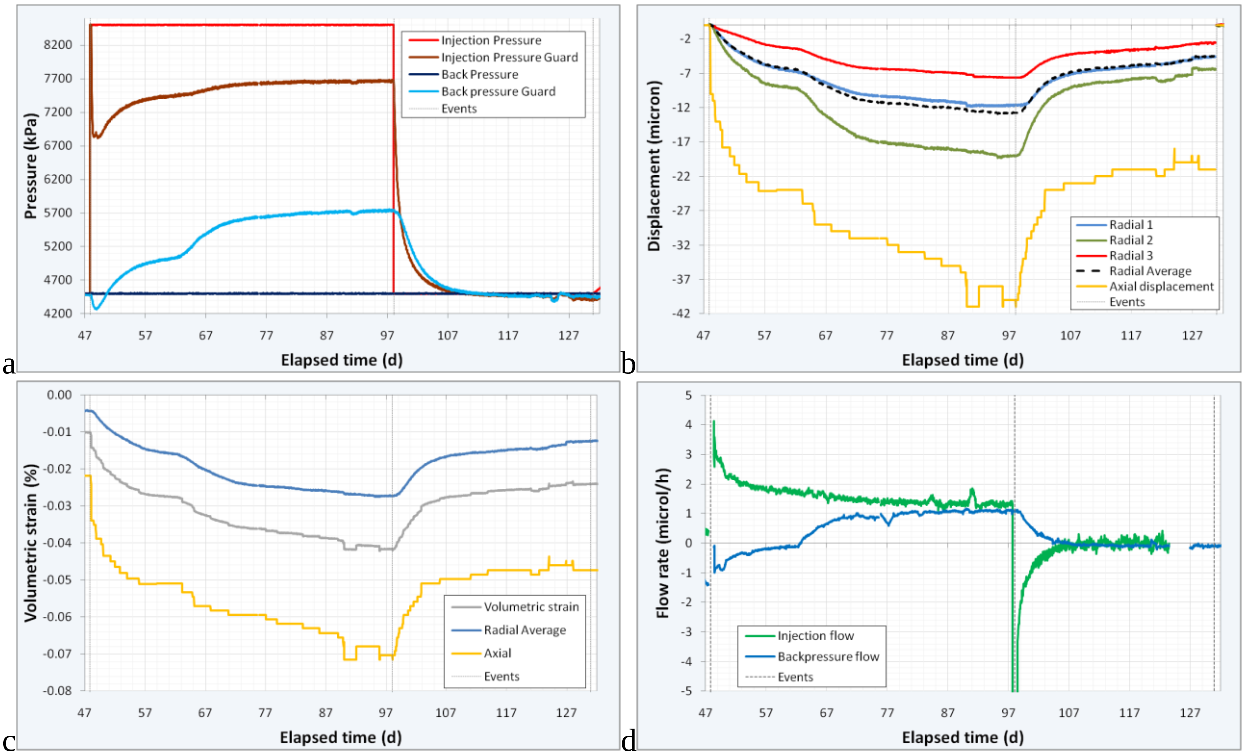

Figure 4-3 Data for the hydraulic testing stage of the test history. A) Pressure history, b) radial and axial displacement, c) sample strain, and d) flow data.

4.3.1 Computed hydraulic permeability

4.3.1.1 A 3D FLOW MODEL OF THE HYDRAULIC TEST OF SAMPLE SPP_COX-2

A 3D finite element model of porewater flow in the hydraulic test apparatus was created that included both the sample and the filters at either end. The symmetry of the experimental apparatus permits the model to consider just a quarter cylinder and flows into and out of the full system will be four times those obtained from this model. The material components and the mesh used are shown in Figure 4-4. It was assumed that the sample's bedding lay in the X-Z plane with the Y axis perpendicular to bedding. It can be seen that elements were included in the model to represent the end surfaces between the filters. These were given very low permeabilities so that the response of the sample alone could be considered.

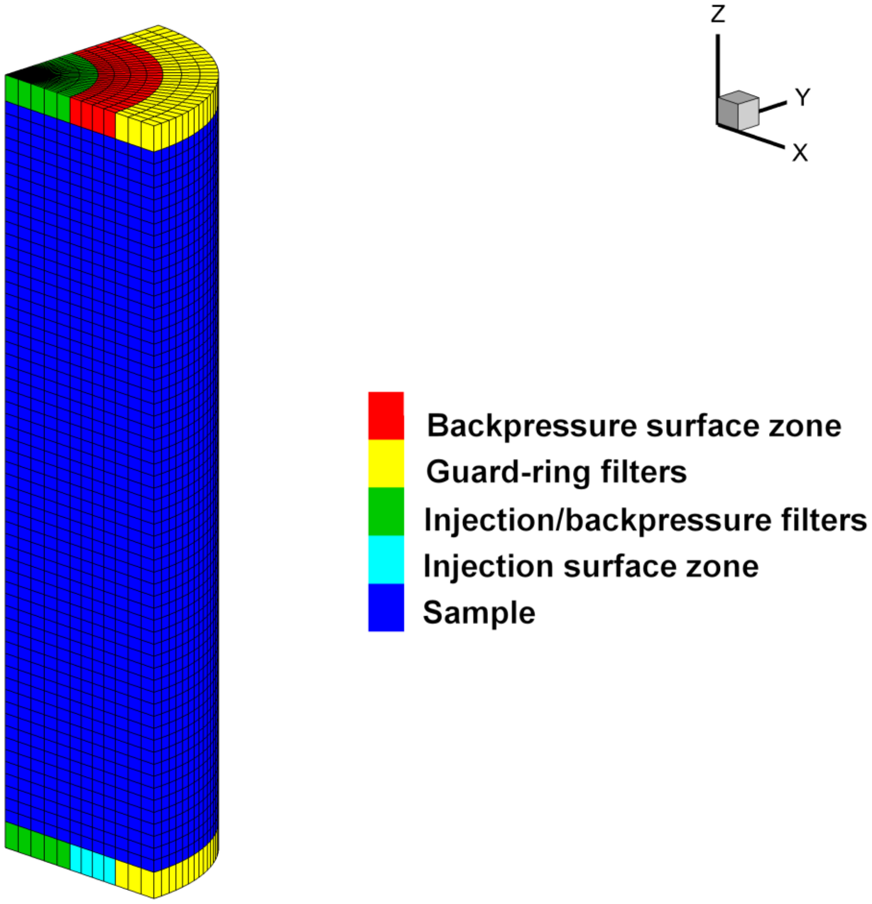

Figure 4-4 The material components and mesh of the quarter cylinder flow model used for simulation of the hydraulic test.

4.3.1.2 Model with isotropic permeability fitted to flow data

An initial model was run in which the clay sample was assumed to have an isotropic permeability and the value was adjusted to fit the data for flows into and out of the sample. The fit shown in Figure 4-5 was obtained using a permeability of 5.8×10^{-21} m^2 and a specific storage of $1.3 \times 10^{-5}.m^{-1}$. It can be seen that a rather poor fit has been obtained to the data. The model's predictions for the guard-ring pressures are also quite poor as shown in Figure 4-6. It may be noted that some features of the data suggest that experimental conditions were not quite as assumed for this model. In particular, the outflow data for the period from the start of the test at 47 days until about 63 days show flow is into the sample, an effect that is impossible to achieve with this model. The guard-ring data also indicate some sort of event occurring at around Day 63 that cannot be accommodated by this model. The model does achieve a reasonable fit to the injection guard-ring pressures by the end of the injection period, beyond 90 days, but the model's prediction for the pressure at the back-pressure guard-ring is poor, possibly indicating some heterogeneity within the core. The pressure data for the injection guard-ring also appear to be anomalous early in the test when it rises to 8,500 kPa with the injection pressure, then drops rapidly to less than 7,000 kPa before starting to rise again.

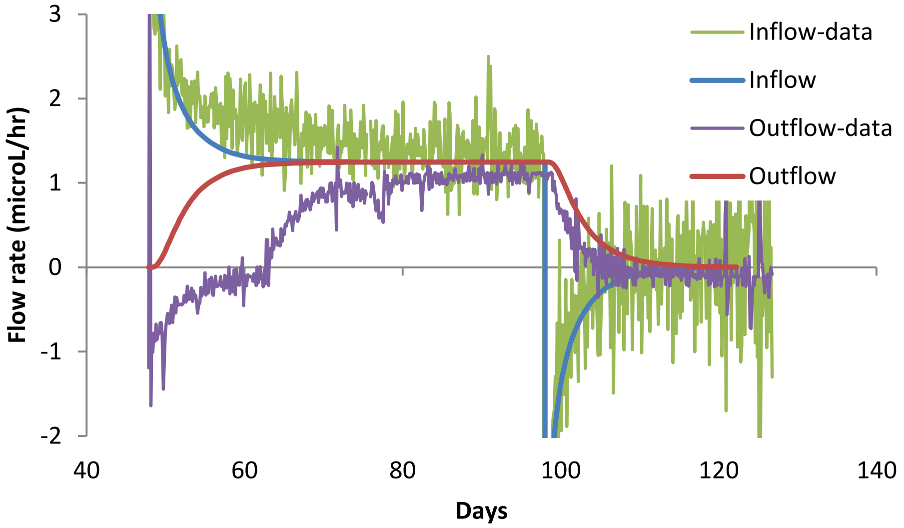

Figure 4-5 Comparison of an isotropic permeability model with flow data.

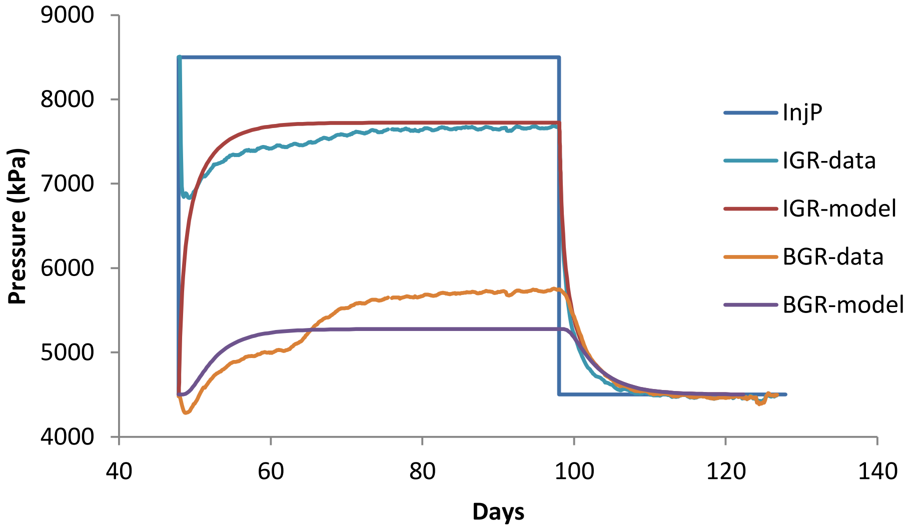

Figure 4-6 Comparison of an isotropic permeability model with guard-ring pressure data.

4.3.1.3 MODEL WITH ANISOTROPIC PERMEABILITY FITTED TO FLOW DATA

Since the sample is known to have bedding in the X-Z plane further models were run with the Y-axis component of permeability reduced to see if the fit of the guard-ring pressure response to the data could be improved. Figure 4-7 and Figure 4-8 show results from a model with an anisotropy of 10, the X-Z plane permeability having been adjusted to fit the flow rate data. Here the X-Z plane permeability is 6.7×10^{-21} m^2 and the Y-axis permeability is 6.7×10^{-22} m^2. The specific storage is 1.0×10^{-5} m^{-1}. It can be seen that the guard-ring pressure fit is not significantly better than for the isotropic model.

A model with an anisotropy of 100 produced very similar plots, the X-Z plane permeability having been increased slightly to 7.0×10^{-21} m^2 to generate the same flow rate at the end of the injection period. Thus it would seem that the test can be modelled with bedding plane permeabilities in the range 5.8 – 7.0×10^{-21} m^2 depending upon the degree of anisotropy caused by the bedding, but that anisotropy cannot be uniquely determined and there are several features of the data that cannot be understood using this purely hydraulic model, as detailed above.

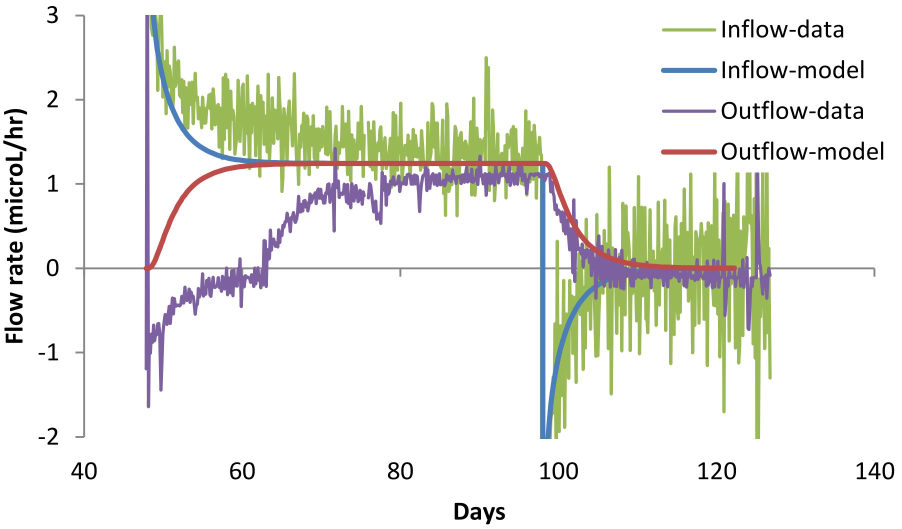

Figure 4-7 Comparison of an anisotropic permeability model with flow data.

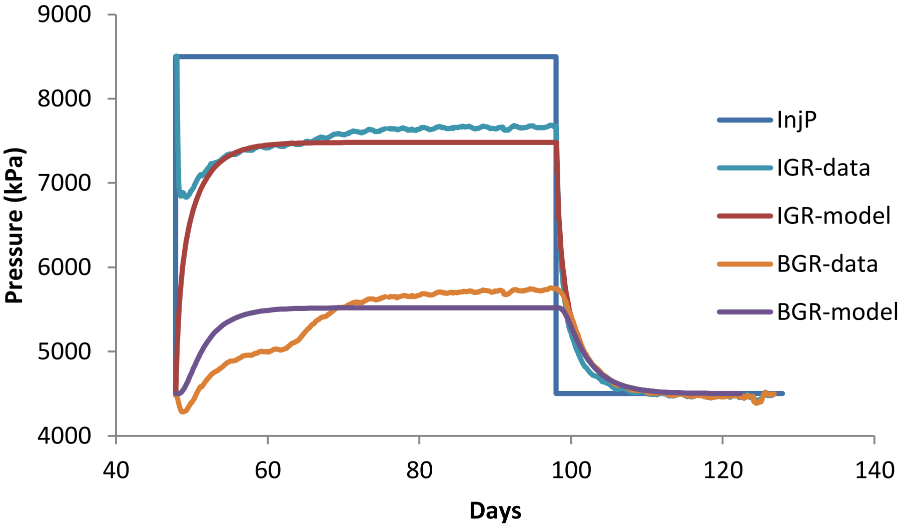

Figure 4-8 Comparison of an anisotropic permeability model with guard-ring pressures.

Harrington *et al.* (2012) report the hydraulic properties of two test samples of COx, both tests were conducted with flow perpendicular to bedding. Axial permeability was seen to be 1.6 to 2 × 10^{-21} m^2; however, radial anisotropy was needed in order to fit guard-ring pressure responses with permeabilities of 4.0 to 5.0 × 10^{-21} m^2 for test sample COx-1 and 8.8 and 22.4× 10^{-21} m^2 for sample COx-2. As samples COx-1 and COx-2 were conducted perpendicular to bedding the radial direction will correspond with the axial direction in the current test; where samples were prepared parallel with bedding. The permeability calculated for the current test (5.8 – 7.0 × 10^{-21} m^2) is similar to the radial permeabilities reported for COx-1 and COx-2 as reported by Harrington *et al.* (2012). However, it should be noted that specific storage in the current test is higher than reported for COx-1 and COx-2; 13.0 × $10^{-6}.m^{-1}$ compared with 5.4 – 6.0 × $10^{-6}.m^{-1}$. This may suggest that certain inter-beds have more storage capacity and are more permeable than others. Testing parallel to bedding makes these beds more accessible compared to tests conducted perpendicular to bedding. It can therefore be seen that the current test results are similar to those reported previously.

5 Gas testing

On Day 131 the gas testing phase was started, results are shown in Figure 5-1 up until the point of near stead-state flow. The interface vessel on the injection circuit was filled with 281 ml of helium at 4.5 MPa. A constant flow pressure-ramp was initiated with a flow rate of 190 μl.h^{-1} (STP flow of 2.24 – 4.63 × 10^{-9} m^{3}.m^{-1}) designed to raise pressure to 9.5 MPa in 30 days. As can be seen no flow was seen and so on Day 163 the injection pump was set to a low flow of 1 μl.h^{-1} and held for 24 days. Prior to the switch to constant pressure the guard-ring pressure data showed an increase. The injection guard-ring peaked at about 5.2 MPa and slowly decayed. This did not correspond to an inflow into, or outflow from, the sample. The kick seen in axial displacement was the result of temperature variation in the laboratory and was not a “real” sample strain.

The injection system was again changed to a constant flow pressure ramp on Day 187 to increase injection pressure by 0.5 MPa over a three week period. Again this was accompanied by subtle changes in guard-ring pore-pressure, however gas flow was not initiated. The test was switched to constant pressure on Day 210 and held for 26 days. During this period the pressure in both guard-rings decayed.

The final pressure ramp was initiated on Day 236 and similarly raised pore-pressure by 0.5 MPa over a 3 week period. Almost immediately prior to reaching an injection pressure of 10.5 MPa the injection guard-ring pressure greatly increased. This is introduced in more detail in the next section.

Between Day 131 and the onset of marked radial deformation (approximately Day 254) the sample showed small volumetric reduction of approximately 0.003 %.

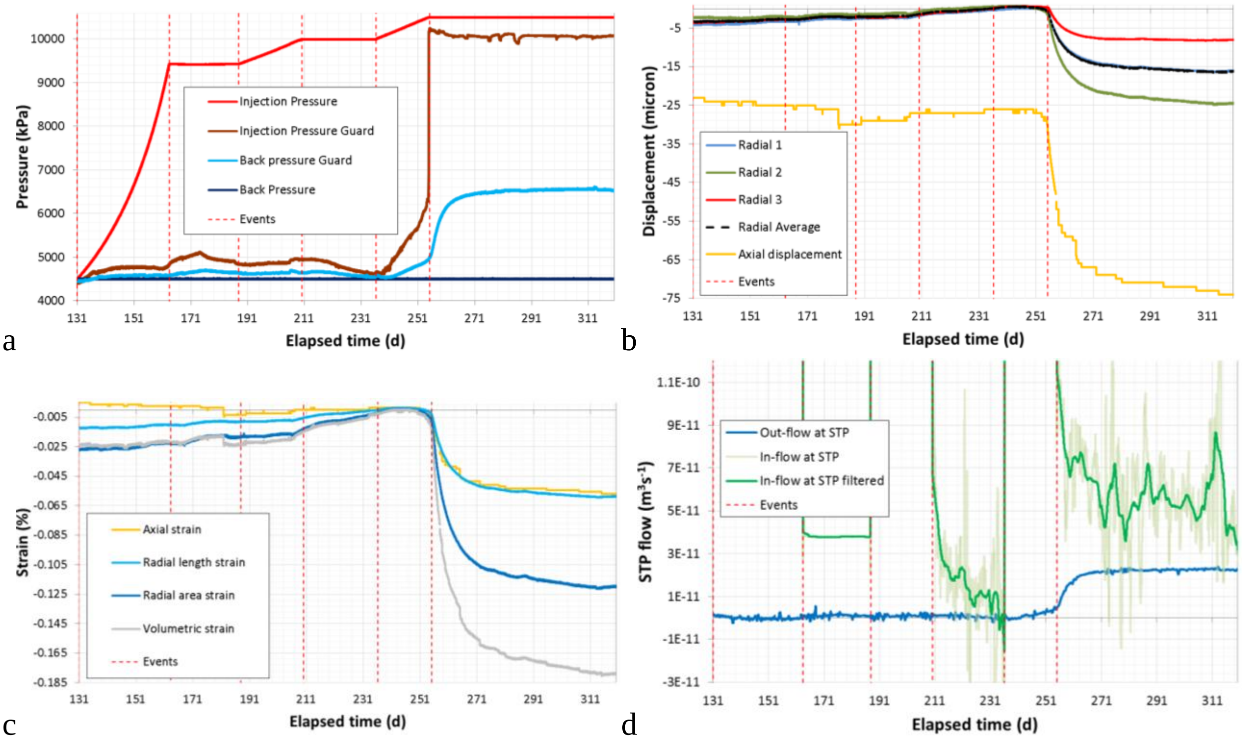

a b c d

Figure 5-1 Data for the gas testing stage of the test history up until the attainment of near steady-state flow. A) Pressure history, b) radial and axial displacement, c) sample strain, and d) flow data.

5.1 GAS FLOW INITIATION

In this section we discuss the data at the time of the onset of gas flow. Figure 5-2 to Figure 5-4 show the data in more detail between Day 230 and Day 280. In order to distinguish the subtle responses related to the onset of gas flow all data were closely examined and "events" were recorded, these are summarised in Appendix 1. These observations allow decoupling of the influence of temperature variation on any recorded results and allow the coupling between parameters to be determined. The "exact" timing of the events may include a certain degree of subjectivity. However, we have attempted to be consistent in the way events have been determined. All events are displayed on Figure 5-2 to Figure 5-4 as dotted lines.

5.2 EVENTS DURING CONSTANT-FLOW PRESSURE RAMP (DAY 236 – 256)

The test was switched to constant flow in order to increase the gas injection pore-pressure from 10 MPa to 10.5 MPa. All data suggested that flow had not initiated at 10 MPa. Figure 5-2 summarises the main events that occurred during the constant-flow pressure ramp.

During the constant pressure ramp it can be seen that pressure in the injection guard-ring started to increase from about Day 235.9 onwards (Figure 5-2a). This appears to correspond with unexplained behaviour in the load cells (Figure 5-2d). In the injection end this device, which in Cuss & Harrington (2010) was believed to be faulty, showed a slow decline in reading and at the point where the injection guard-ring started to increase a marked jump in (uncalibrated) load cell reading was observed. The exact timing of this event was Day 237.32.

It is difficult to determine precisely when pore-pressure in the back-pressure guard-ring started to increase (Figure 5-2b), but there was at least a one day lag compared with the injection guard-ring pressure event and occurred at about Day 240.5. What is clear is that the rate of increase in pressure at the back-pressure end of the sample was much less than that at the injection end. It can also be seen that the pressure increase at the injection end showed considerable instability, whereas at the back-pressure end the increase was much more smooth. This suggests that the increase at the injection end was as a result of gas migration to the guard-rings, whereas the change at the back-pressure end was a hydromechanical response to effective stress changes.

Between Day 237 and Day 254.7 the pressure in the injection guard-ring increased from approximately 4.6 MPa to 6.3 MPa, whilst in the back-pressure guard-ring the pressure increased from 4.5 MPa to 4.9 MPa. At Day 254.7 pressure in the injection guard-ring increased significantly from 6.3 MPa to a peak of 10.5 MPa (Figure 5-2a and Figure 5-2e). As can be seen in Figure 5-2e the pressure increase was rapid (2 minute interval between data points) with pressure increasing more 3.5 MPa within a period of 1 hour.

Figure 5-2c shows the deformation data during the pressure ramp stage. As can be seen, from Day 230 to 245 the radial deformation showed that the sample was slowly compacting. It should be noted that during this 15 day period the average radial deformation was approximately 1 μm. However, careful examination of this data shows several changes of slope in all three radial measurements. At Day 239.8 all three radial measurements showed a deflection in their rate of change (see Figure 5-3). This was most pronounced in Radial 2 which reached a plateau at this time. Radial 3 reached plateau at Day 243.5, a time which corresponds with the start of negative (dilatant) strain being shown by Radial 2. Radial 1 does not plateau in the same manner as Radial 2 and 3, although it did peak at Day 250. Therefore the first indication of dilatancy was observed at Day 239.8 for Radial 2, Day 243.5 for Radial 3, and Day 250.21 for Radial 1.

It can be seen in Figure 5-2c and Figure 5-3 that the onset of accellerated dilatant deformation occurred at Day 254 for Radial 2, Day 254.7 for Radial 1, Day 255.1 for Radial 3 and 265.03 for axial strain. What can also be seen is that by Day 256 the rate of change of all three radial strain sensors was similar. This suggests that initial flow through the sample was probably localised through the centre of the sample, but with time the flow homogenised and strain evenly distributed through the radial mid-plane.

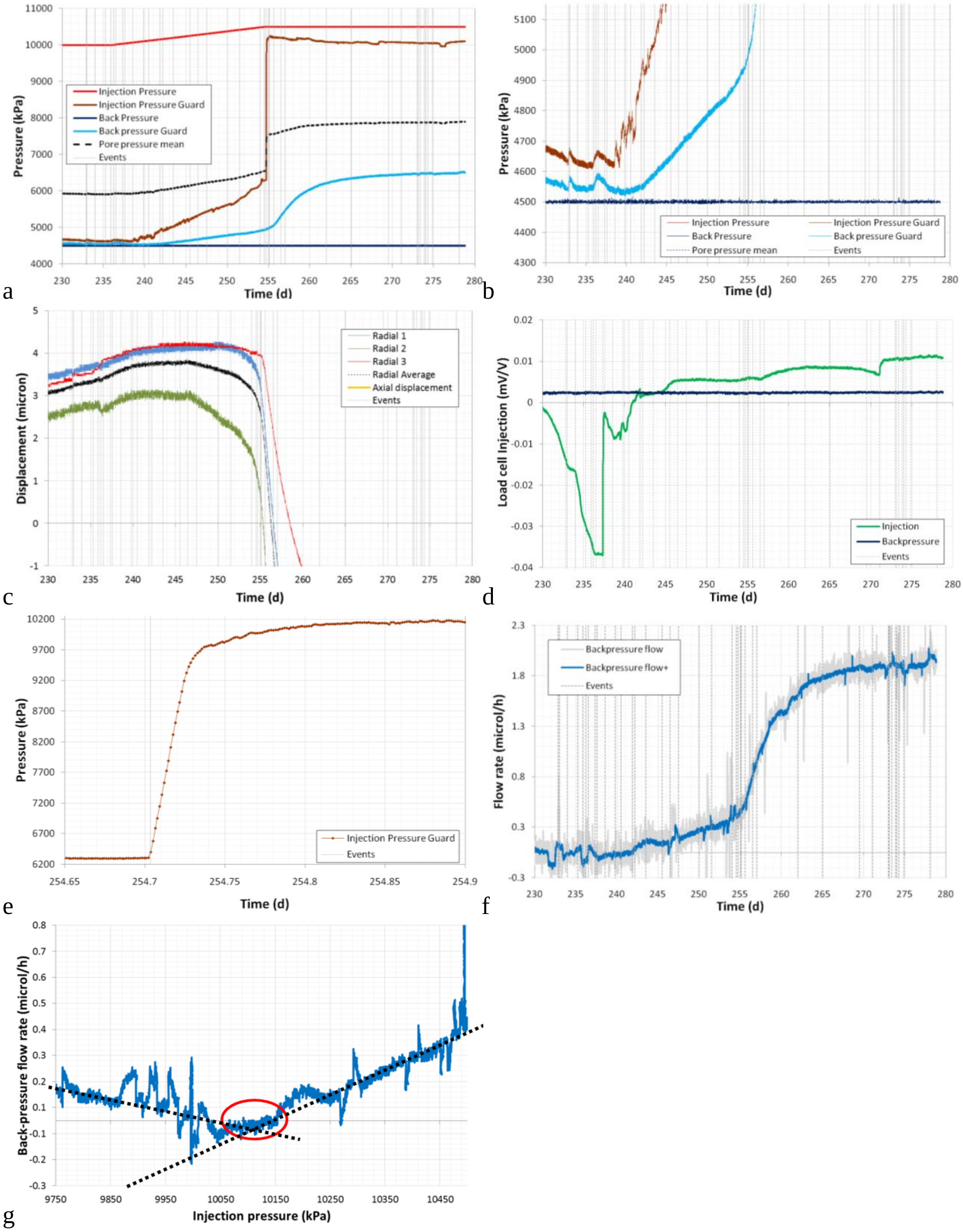

Figure 5-2 Summary of main events that occurred during the constant-pressure ramp. A & b) pressure history; c) deformation; d) axial load; e) injection pressure guard-ring; f) back-pressure flow; g) back-pressure flow versus injection pressure.

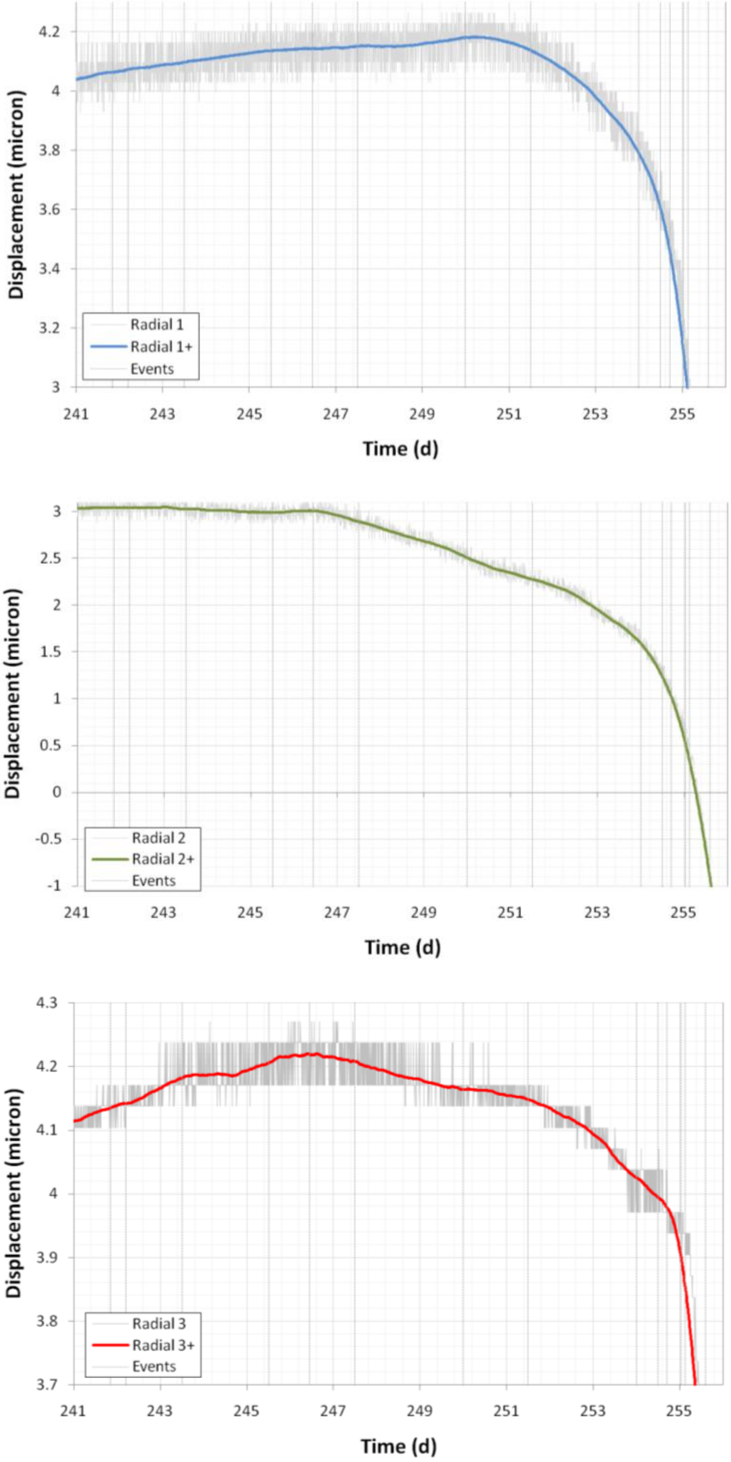

a.

b.

c.

Figure 5-3 Detail of the radial deformation recorded at the mid-plane of the sample at the onset of gas flow.

Taking all observations into account it can be suggested that gas started to flow into the COx on Day 237.32 with gas moving to the location of the load cell. This occurred at an injection pressure of 10.04 MPa. This observation fits with the timing of pressure changing in the injection guard-ring (Day 238.55). However, as both the injection-end load-cell and guard-rings are a distance from the injection point, it is suggested that gas entry occurred prior to Day 237.32. Figure 5-2g shows the relationship between injection pressure and back-pressure flow. This shows that flow started to increase at a gas pressure of 10.15 MPa (breakthrough pressure of 5.65 MPa). Therefore all observations suggest that the gas breakthrough occurred at an excess pressure of approximately 5.65 MPa.

All data were carefully examined between Day 200 and Day 237.32 for any evidence of gas entry. It should be clearly noted that the laboratory experienced several small (~0.1 ºC) temperature variations during this period. Small variations in laboratory temperature are seen to influence the response of several sensors in such a way that the effect cannot be removed by careful calibration. Therefore it is difficult to determine the onset of gas flow with a high degree of confidence. During constant flow experimentation the onset of flow can be suggested by comparing the difference between predicted gas pressure from the ideal gas law and observed gas pressure; this data is shown in Figure 5-4. It can be seen that between Day 202 and Day 211.5 was affected by a 0.25 ºC temperature variation in the laboratory. At the injection pressure the variation recorded was approximately equal to that predicted by the ideal gas law. However, Figure 5-4 shows a change in slope at Day 220, which corresponds with a significant deflection of the injection-end load cell at Day 221.875. Therefore, we suggest that Day 221.875 represents an early gas entry event.

It is suggested that gas propagated along the end of the sample, with the behaviour of pressure response at the guard-ring suggestive of the presence of gas. The pressure response at the back-pressure end of the sample also suggests that gas reached both the filter and guard-rings. The symmetry of the radial deformation suggests that gas propogated through the centre of the sample, as does the timing of pressure changes in the filter and BGR. Therefore, sidewall flow can be discounted and the observed gas propagation was through the body of the sample and the radial flow observed was as a result of bulk sample dilation and not inflation of the Hoek sleve.

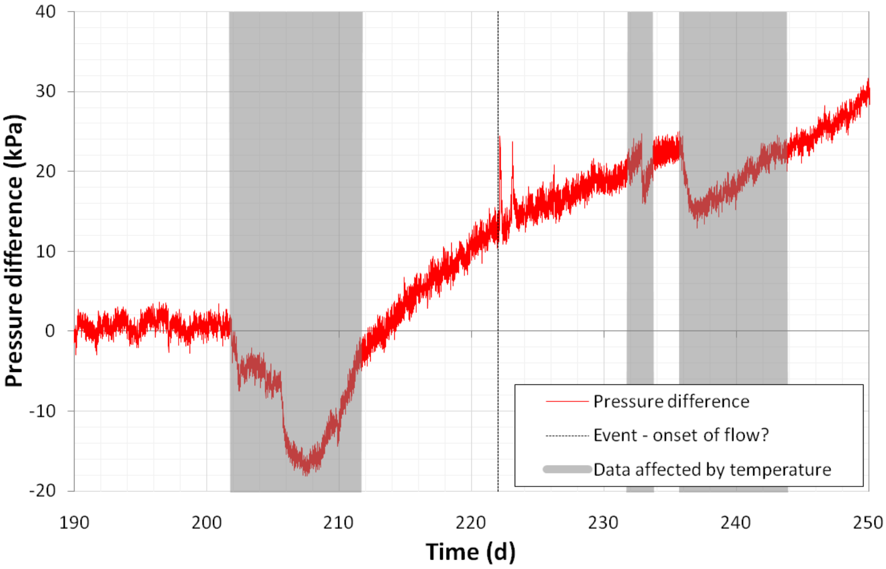

Figure 5-4 The difference between predicted gas pressure for constant flow testing and recorded pressure. Three periods within this data are seen to be affected by small temperature variations within the laboratory. However, a change in slope is seen at Day 222, which may indicate the onset of gas flow into the sample.

5.3 EVENTS DURING CONSTANT PRESSURE STAGE (DAY 256 – 320)

The injection pump was changed from constant flow to constant pressure once dilatant deformation had been identified. This change occurred at Day 255.06 soon after the significant pressure increase in the injection pressure guard-ring had occurred. Figure 5-5 summarises the main events that occurred during the constant pressure stage.

As seen in Figure 5-5a, Figure 5-5b and Figure 5-6 marked deformation occurred following the onset of gas flow. Figure 5-5a shows that a total of 48 microns of length dilation occured. The average radial dilation was approximately 16 microns. This represents a total volumetric strain of 0.18 % or 360 µl change in sample volume. The sample deformation is confirmed by examining the change in volume of the confining system during the same period (see Figure 5-6); this gives an estimate of approximately 500 µl change in sample volume. As can be seen in Figure 5-6 the change in volume of the confining pressure shows that deformation occurred earlier than the onset of deformation seen at the radial mid-plane. The confining fluid volume data also suggest that by Day 320 the sample was beginning to contract.

Figure 5-5c shows the flow data for the injection and back-pressure ends of the sample. Following the switch from constant flow to constant pressure the injection end flow decayed initially to a flow rate of 4.7 µl.h^{-1} (8×10^{-11} m^3.s^{-1}) at Day 261. However, flow slowly decreased so that by Day 320 flow had decresed to approximately 3.5 µl.h^{-1} (5×10^{-11} m^3.s^{-1}). During the same period the back-pressure flow incrased to a steady 2 µl.h^{-1} (2.2×10^{-11} m^3.s^{-1}).

Figure 5-5d to Figure 5-5f show the pressure response of the sample. As can be seen, the injection guard-ring peaked at a pressure of 10.23 MPa and slowly decayed. The nature of this decay was chaotic and indicative of unstable gas pathways. By Day 278 the pressure was 10.1 MPa. The pressure in the back-pressure guard-ring (Figure 5-5f) showed an even increase in pressure. It can be seen that the increase in pressure started to become unstable from Day 273 onwards. This may indicate that gas had migrated as far as the back-pressure guard-ring. However, we cannot determine whether pressure changes are as a result of the presence of water or gas. By Day 320 the pressure in the back-pressure guard-ring had asymptoped at a value of approximately 6,550 kPa.

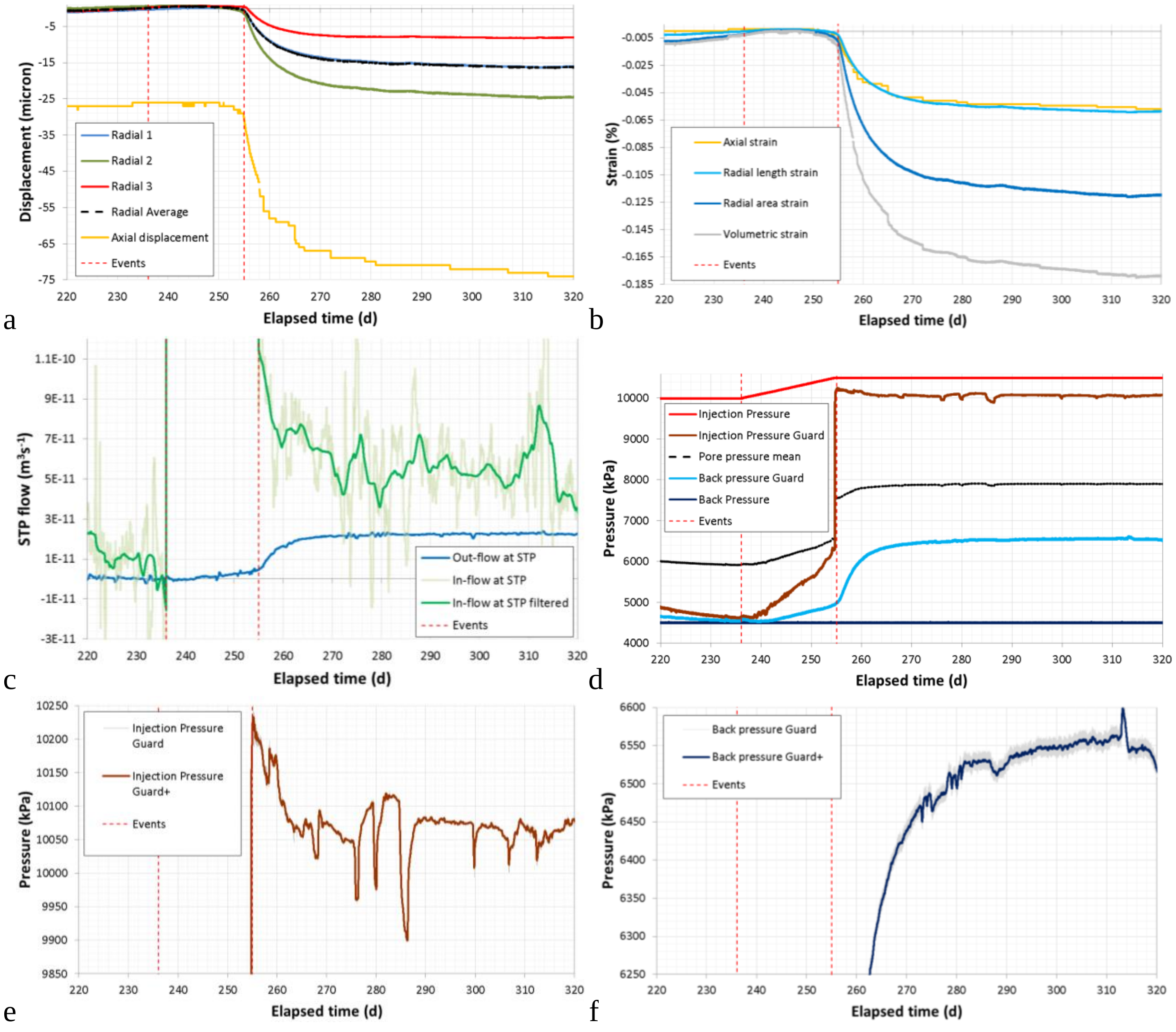

Figure 5-5 Summary of main events that occurred during the onset of gas flow. A) deformation; b) volumetric strain; c) injection and back-pressure flow; d) pressure history; e) detail of pressure at injection guard-ring; e) detail of pressure at back-pressure guard-ring.

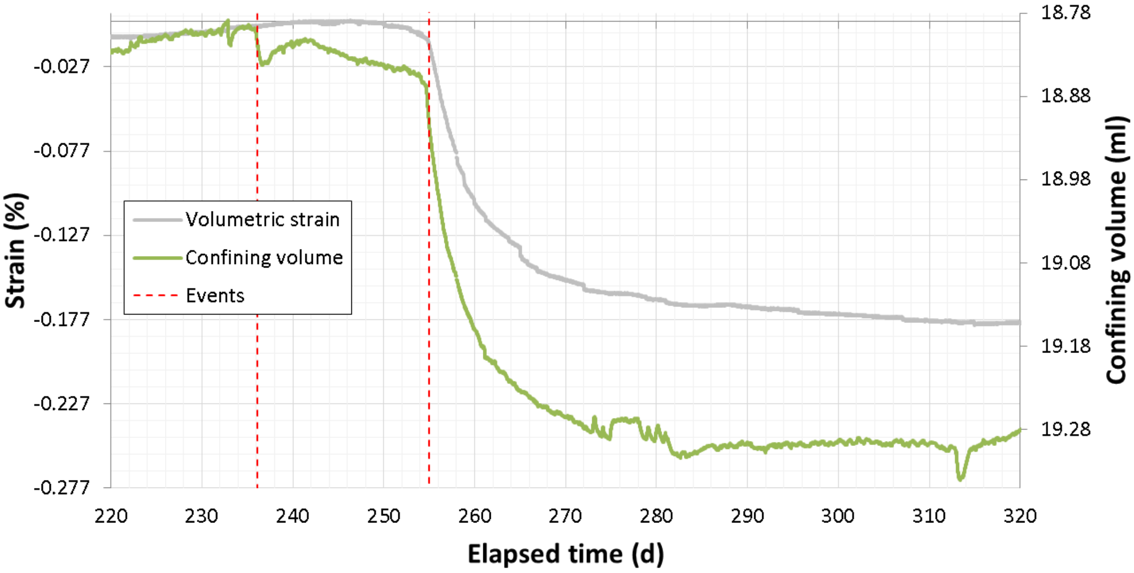

Figure 5-6 Comparison between volumetric strain recorded directly from sample deformation (grey) and changes in the volume of the confining fluid. Note that both axis have been adjusted to represent similar values.

5.4 GAS FLOW SHUT-OFF

Constant pressure conditions were prolonged in an attempt to achieve full steady-state flow conditions. Whilst the outflow from the sample can be seen to have almost reach asymptote, the sample was continuing to dilate and pressure in the guard-rings was also still developing. A decision was taken on Day 314 to allow the sample 7 more days of equilibrating before moving to the next stage of testing. However, around Day 320 the outflow from the sample started to change and so the test stage was prolonged. Figure 5-7 summarises the main events that occurred during the shut-off of gas flow and Figure 5-8 summarises events during the onset and shut-off of flow.

Figure 5-7c shows that outflow from the sample started to decrease around Day 320; the exact timing is difficult to determine. Soon after flow can be identified as reducing, the radial strain recorded at the mid-plane started to contract (Figure 5-7a). Radial 3 was the first to show signs of contraction on Day 319.6. This was followed by Radial 2, Radial 1 and axial displacement on Day 320.6, 322.2 and 325 respectively. This “order” of response of R3, R2, R1 and Axial compares with R2, R3, R1 and Axial seen during the initiation of flow. However, it should be noted that the time between responses is less during shut-off than during flow initiation. During the initiation of flow there was 11 days between the first and last radial sensor detecting dilatancy, compared with less than 3 days during shut-off.

Figure 5-8a shows the radial and axial displacement seen during the onset of flow and shut-off. It can be seen that Rradial 3 recovered all of the strain during the shut-off phase. Radial 1 and Radial 2 did not recover strain fully and by Day 369 showed 5.3 and 2.7 µm permanent deformation (32 and 9.2 % permanent deformation for Radial 1 and Radial 2 respectively). Considerable permanent deformation was also observed axially, with 25 µm permanent deformation seen; therefore only 50 % of total axial displacement was recovered during the shut-off of flow. Figure 5-9 and Figure 5-10 show the volumetric strain of the sample as recorded directly from the strain sensors and from the volume of the confining system. As seen, 0.05 % permanent dilatant strain is suggested from the strain data. However, the confining volume data suggests that more strain was recovered and suggests 0.03 % permanent dilation is more likely. The volumetric strain data suggest that between 60 and 100 µl of permanent deformation is noted following shut-off of gas flow.

The pressure response of the guard-rings show that the back-pressure guard-ring (BGR, Figure 5-7f) was the first indicator of shut-off on Day 317. Pressure in the guard-ring from this time slowly decreased and reached the back-pressure by Day 369. Pressure within the injection guard-ring (IGR) can be seen to behave quite differently (Figure 5-7e); pressure increased on Day 323.1 from 10,050 kPa to reach 10,450 kPa by Day 330. The raised pressure is close to injection pressure. A further increase was noted on Day 347.4.

One hypothesis put forward for the shut-off was leakage along the injection platen and so injection gas pressure was reduced by 50 kPa slowly between Day 353.9 and Day 368.8. As can be seen in Figure 5-7e the IGR pressure response mirrored injection pressure and it can be inferred that the two were fully connected with one another.

During the period Day 315 to 369 outflow from the sample reduced to zero flow as the sample contracted. It can be seen (Figure 5-7c) that flow into the sample also reduced during the same period.

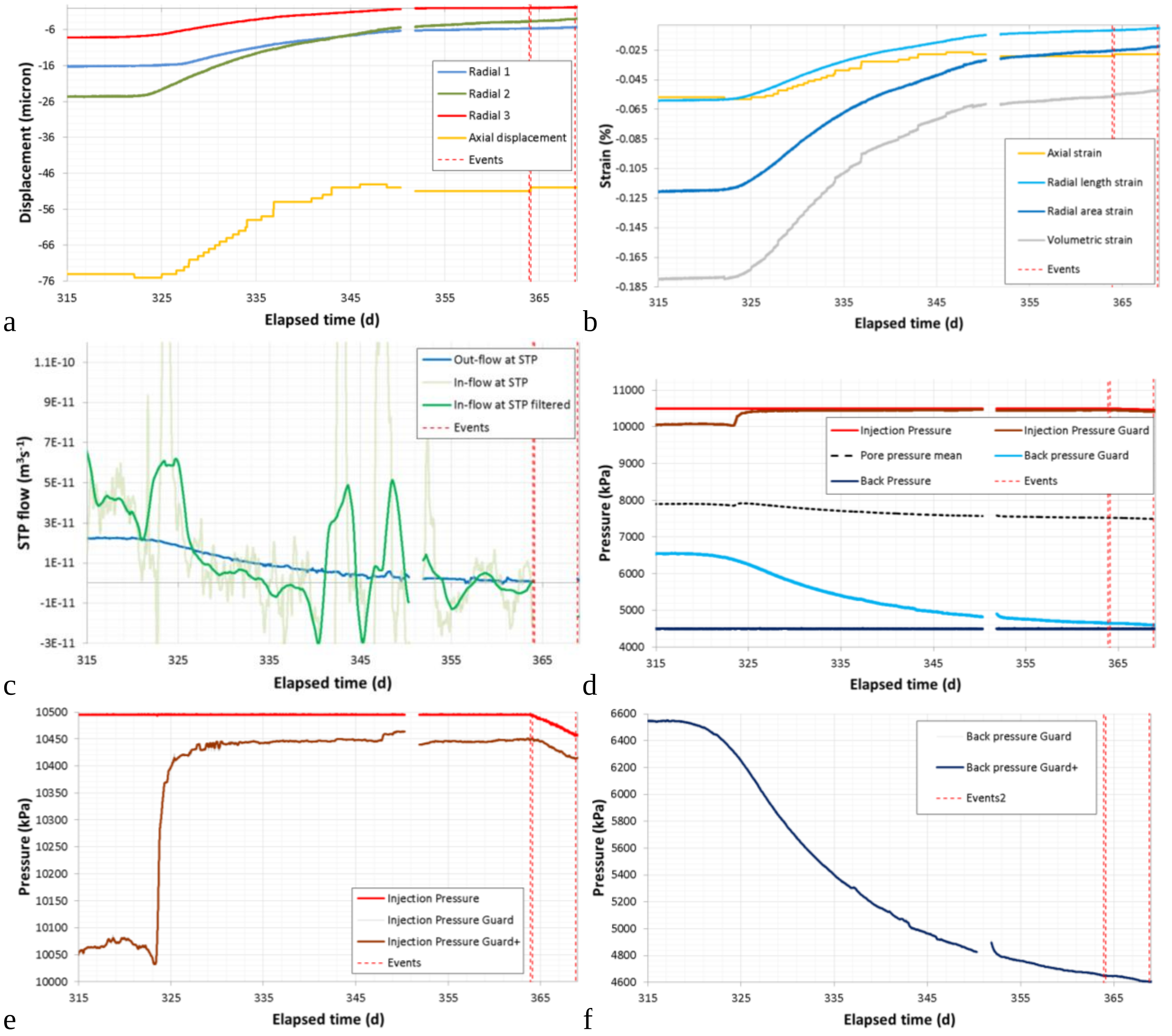

Figure 5-7 Summary of main events that occurred during the shut-off of gas flow. A) deformation; b) volumetric strain; c) injection and back-pressure flow; d) pressure history; e) detail of pressure at injection guard-ring; e) detail of pressure at back-pressure guard-ring.

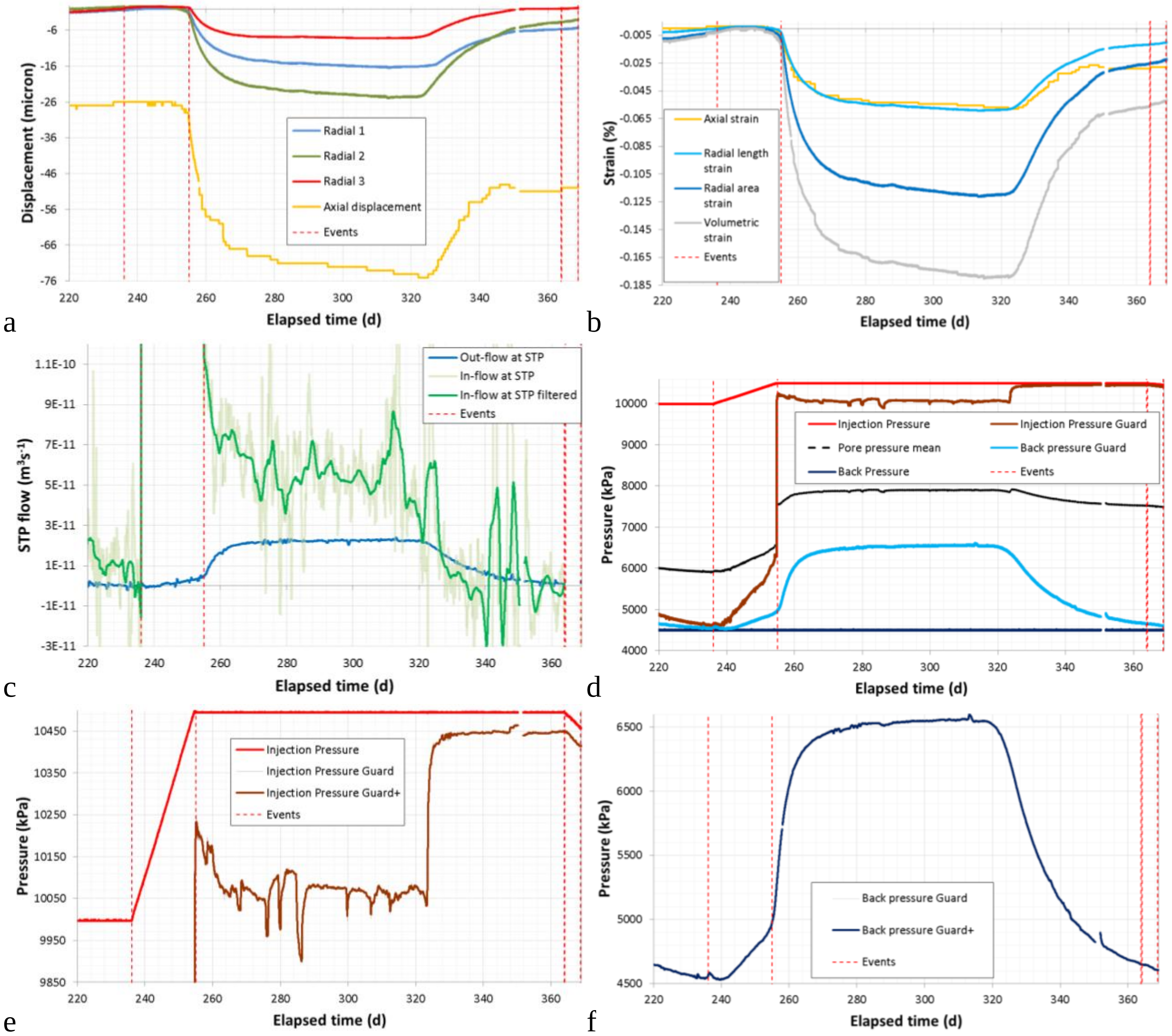

Figure 5-8 Summary of main events that occurred during the onset and shut-off of gas flow. A) deformation; b) volumetric strain; c) injection and back-pressure flow; d) pressure history; e) detail of pressure at injection guard-ring; e) detail of pressure at back-pressure guard-ring.

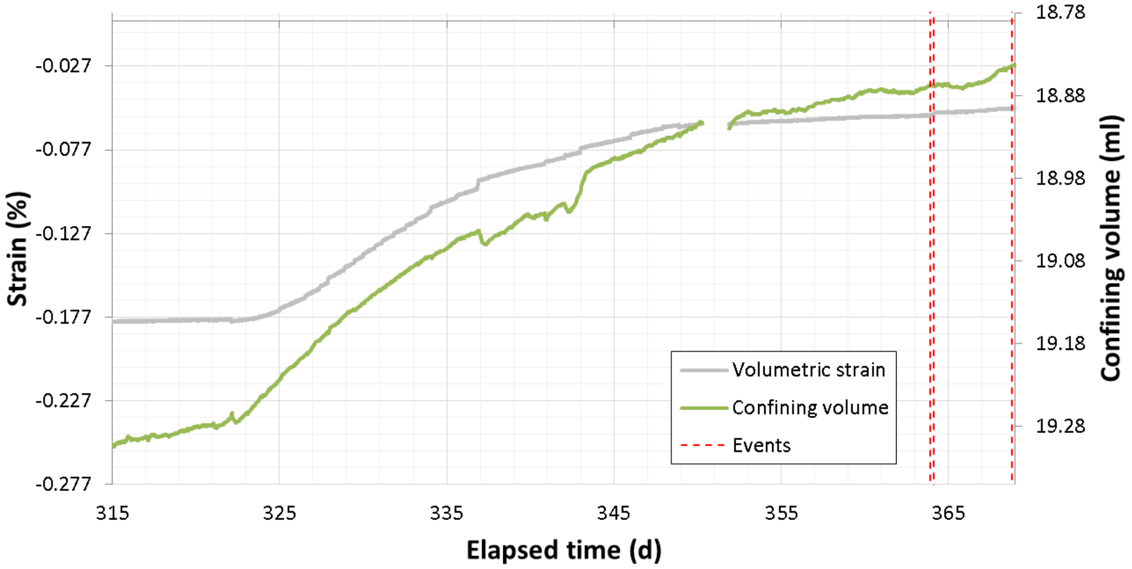

Figure 5-9 Comparison between volumetric strain recorded directly from sample deformation (grey) and changes in the volume of the confining fluid during the shut-off of flow. Note that both axes have been adjusted to represent similar values.

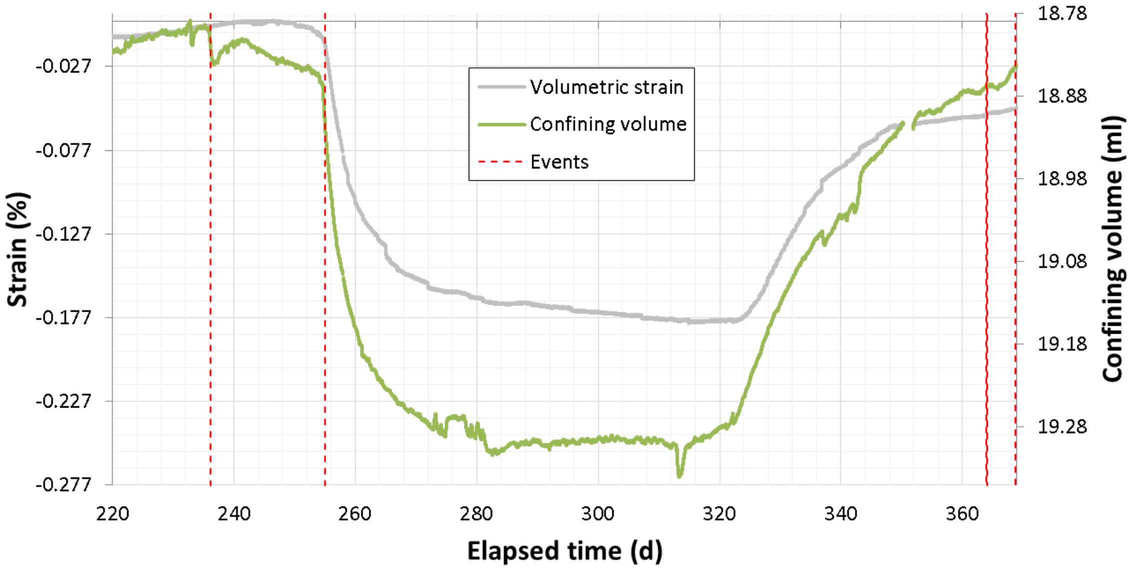

Figure 5-10 Comparison between volumetric strain recorded directly from sample deformation (grey) and changes in the volume of the confining fluid during the onset and shut-off of gas flow. Note that both axis have been adjusted to represent similar values.

5.5 RAISING OF INJECTION PRESSURE TO RE-INITIATE FLOW (DAY 368.8 TO 461.9)

Following the careful reduction of gas injection pressure by 50 kPa and the observation that the injection guard-ring appeared to be directly linked with the injection port, it was decided to raise gas injection pressure from 10.5 MPa to 11 MPa with a constant flow pressure step initiated on Day 368.8 lasting 34.3 days. Gas injection pressure was held constant for a further 58.8 days until Day 461.9.

During the stage approximately 0.025 % dilatant volumetric strain occurred, as shown in Figure 5-11a and Figure 5-11b. This represented approximately 50 µl increase in sample volume. Figure 5-12 shows a comparison between the volumetric strain recorded by the direct strain measurement devices and the change in volume of the confining system. As can be seen the direct measurements suggest sample dilation whereas the confining pressure system suggests that the sample underwent contraction during the stage.

Figure 5-11c clearly shows that outflow from the sample was zero and may possibly have seen a small inflow at the back-pressure end of the sample. A small inflow is observed and this resulted in an increase in pressure in the injection guard-ring pressure as shown in Figure 5-11e. The back-pressure guard-ring reduced in pressure to asymptote at a pressure close to the back-pressure, but marginally increased towards the end of the stage.

During this stage of experimentation it can be inferred that no end-to-end flow was re-initiated by the increased gas injection pressure. It is seen that the injection guard-ring and injection filter became very similar in pressure suggesting that the raised injection pressure has increased the connectivity of these two parts of the system. Back-pressure continued to reduce, which suggests that side-wall leakage was not occurring and that flow was continuing to “shut-off” within the sample. The net volumetric strain during this stage is not clearly determined and suggests that no meaningful volumetric strain occurred, other than the response of the sample to a change in gas injection pressure; i.e. elastic volumetric strain due to a change in effective stress.

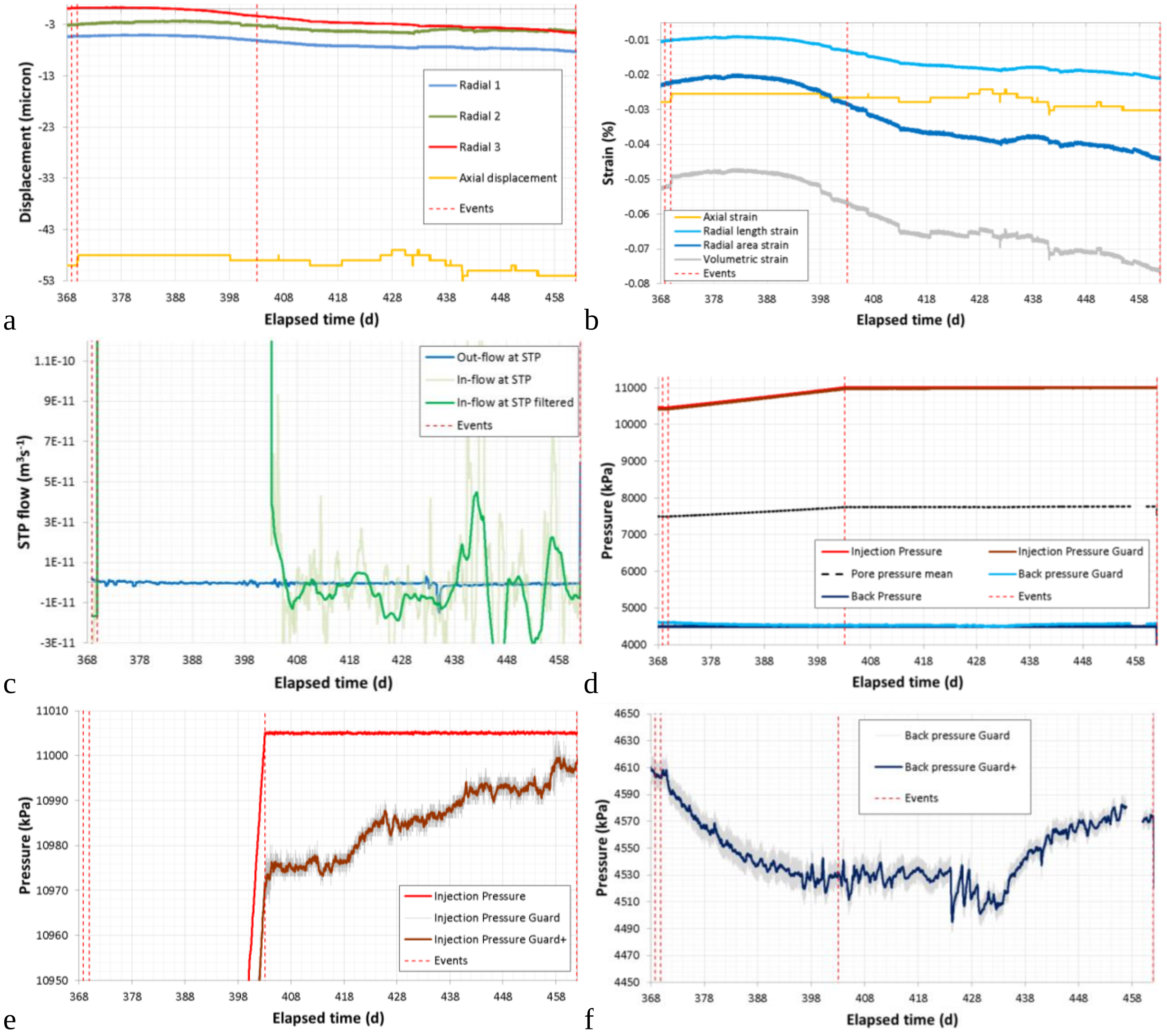

Figure 5-11 Summary of the main events that occurred during the increase in gas injection pressure. A) deformation; b) volumetric strain; c) injection and back-pressure flow; d) pressure history; e) detail of pressure at injection guard-ring; e) detail of pressure at back-pressure guard-ring.

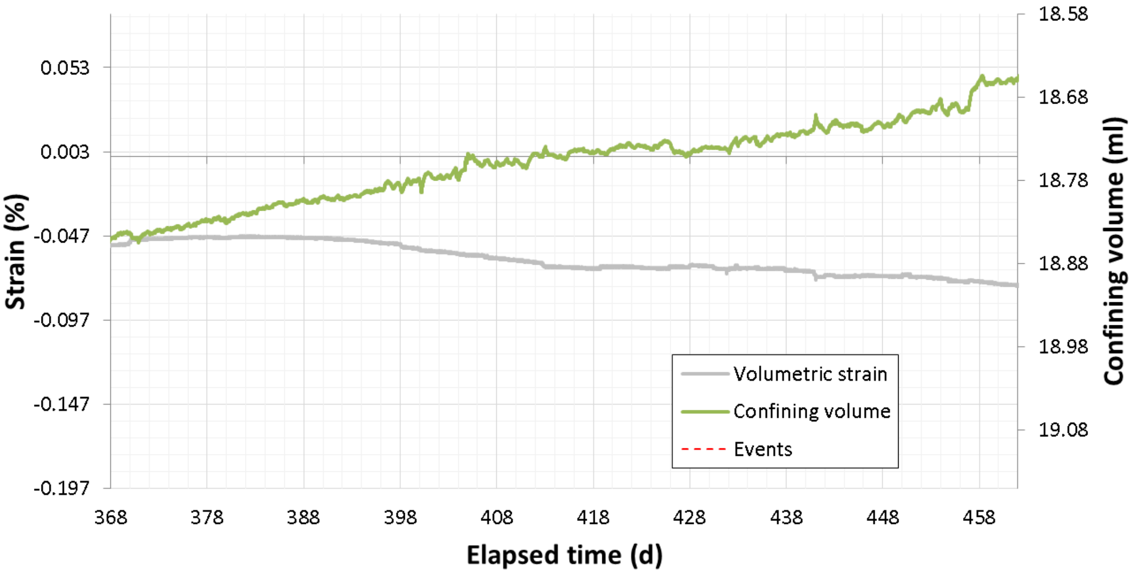

Figure 5-12 Comparison between volumetric strain recorded directly from sample deformation (grey) and changes in the volume of the confining fluid. Note that both axis have been adjusted to represent similar values.

5.6 LOWERING OF BACK-PRESSURE TO RE-INITIATE FLOW

The decision was taken to investigate whether a lowering of back-pressure could result in the re-initiation of gas flow through the sample. A four stage approach was adopted, first lowering back-pressure from 4.5 MPa to 3.5 MPa, then in steps to 2.5 MPa, 1.5 MPa, and finally 1 MPa. Figure 5-13 summarises events during the lowering of back-pressure.

As shown in Figure 5-13a, Figure 5-13b and Figure 5-15, a total of 0.125 % volumetric strain occurred (contraction), equating to a reduction in volume of 275 µl. Therefore the reduction in back-pressure resulted in the consolidation of the sample. Figure 5-15 shows a close comparison between the contraction recorded by the direct strain devices and the change in volume of the confining system. As shown in Figure 5-13f, the reduction in back-pressure of 3.5 MPa resulted in only a 0.85 MPa reduction in pressure in the back-pressure guard-ring.

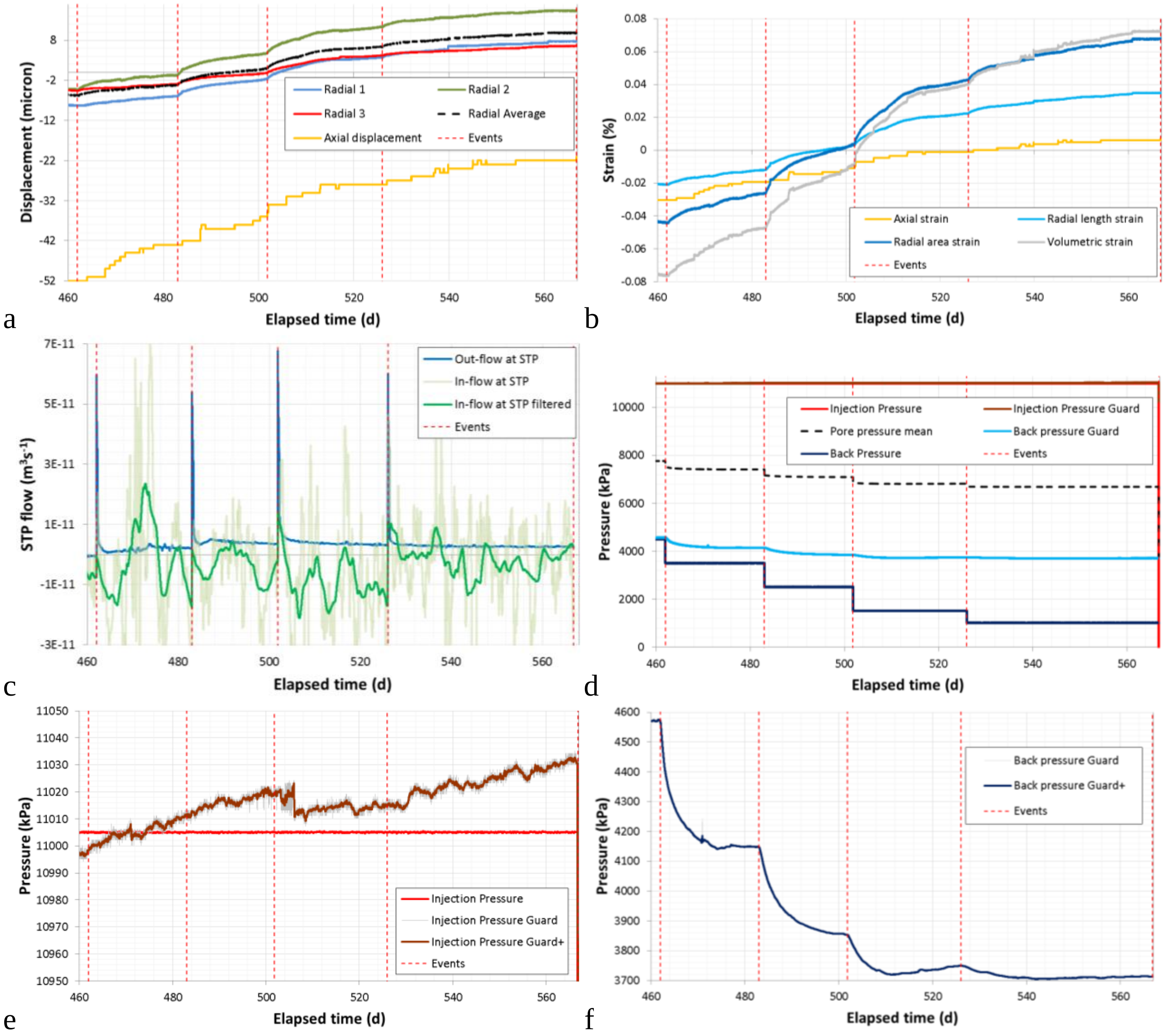

Figure 5-13 Summary of main events that occurred during the lowering of back-pressure. A) deformation; b) volumetric strain; c) injection and back-pressure flow; d) pressure history; e) detail of pressure at injection guard-ring; e) detail of pressure at back-pressure guard-ring.

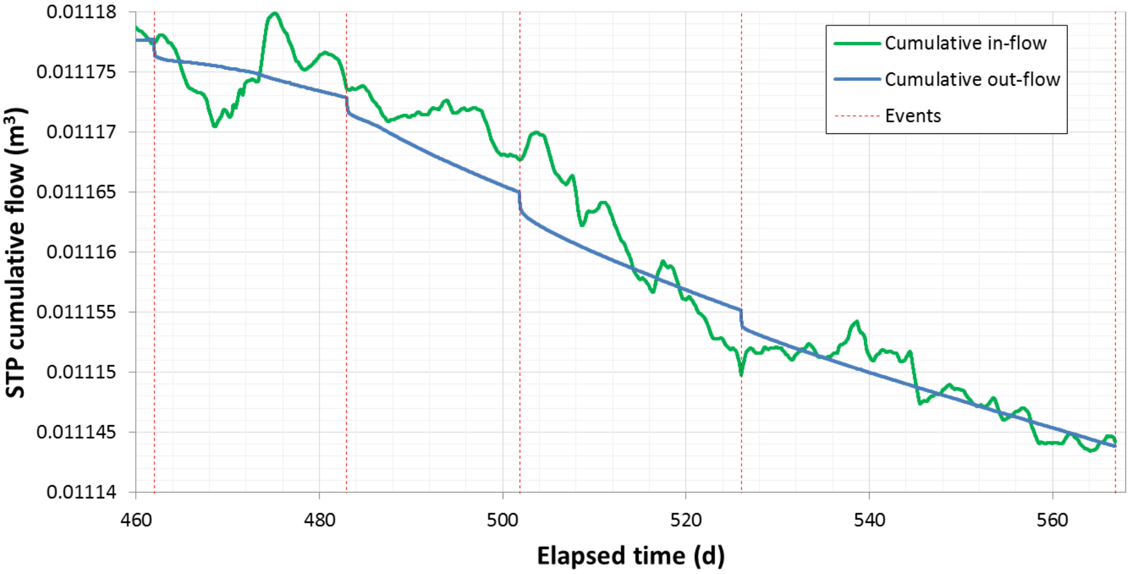

Figure 5-14 Cumulative flow during the stages of lowering back-pressure.

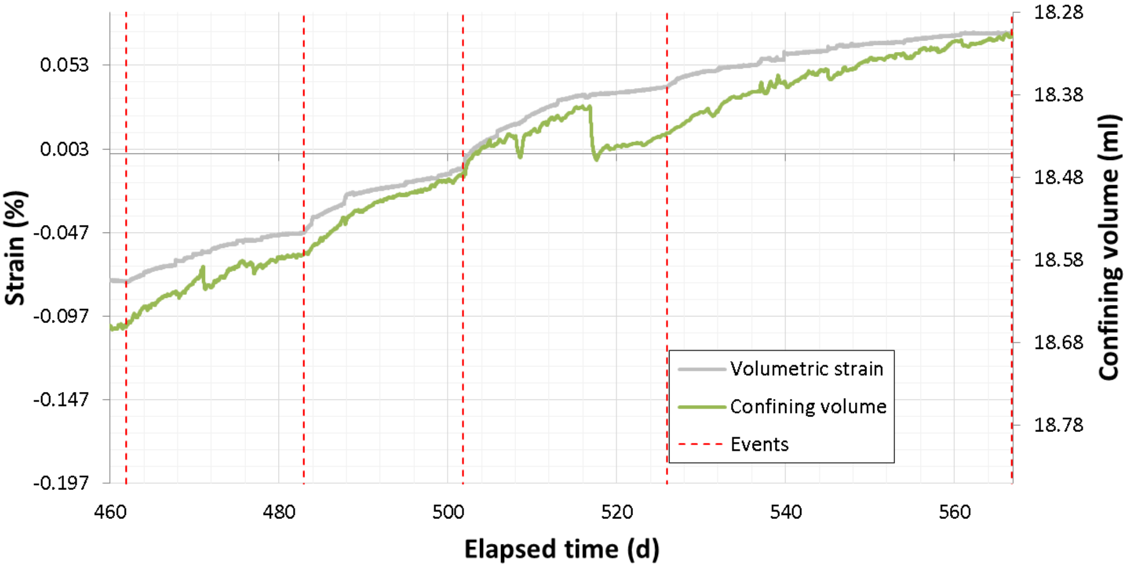

Figure 5-15 Comparison between volumetric strain recorded directly from sample deformation (grey) and changes in the volume of the confining fluid during the lowering of back-pressure. Note that both axis have been adjusted to represent similar values.

Figure 5-14 shows the cumulative flow calculated for the test stages conducted with lowering back-pressure for STP conditions. As can be seen, both the inflow and outflow from the sample match and show that fluid (be it gas and/or water) expulsion from the contracting sample is equal at both ends of the sample; this is to be expected if it solely occurs by drainage in a sample oriented parallel to bedding. Therefore it can be concluded that no gas inflow occurred during this stage of the test programme.

5.6.1 Step 1: Reducing back-pressure to 3.5 MPa

Figure 5-16 shows the detail of the first step of this stage of experimentation with the reduction in back-pressure from 4.5 MPa to 3.5 MPa. As seen, the change in back-pressure resulted in only a small (~60µl) consolidation of the sample volume. During the stage the pressure in the back-pressure guard-ring reduced from 4.55 MPa to 4.15 MPa. The time-dependent nature of the response is due to the drainage of the sample. As a result of drainage, outflow of the sample increased initially and reduced to an asymptote of flow rate of 0.22 µl.h^{-1} (2.2 × 10^{-12} m^3.s^{-1}). It can be seen that the initial increase in flow was followed by a reduction to almost no-flow conditions before recovery to the flow rate of 0.22 µl.h^{-1} (2.2 × 10^{-12} m^3.s^{-1}). During the period inflow into the sample remained constant.

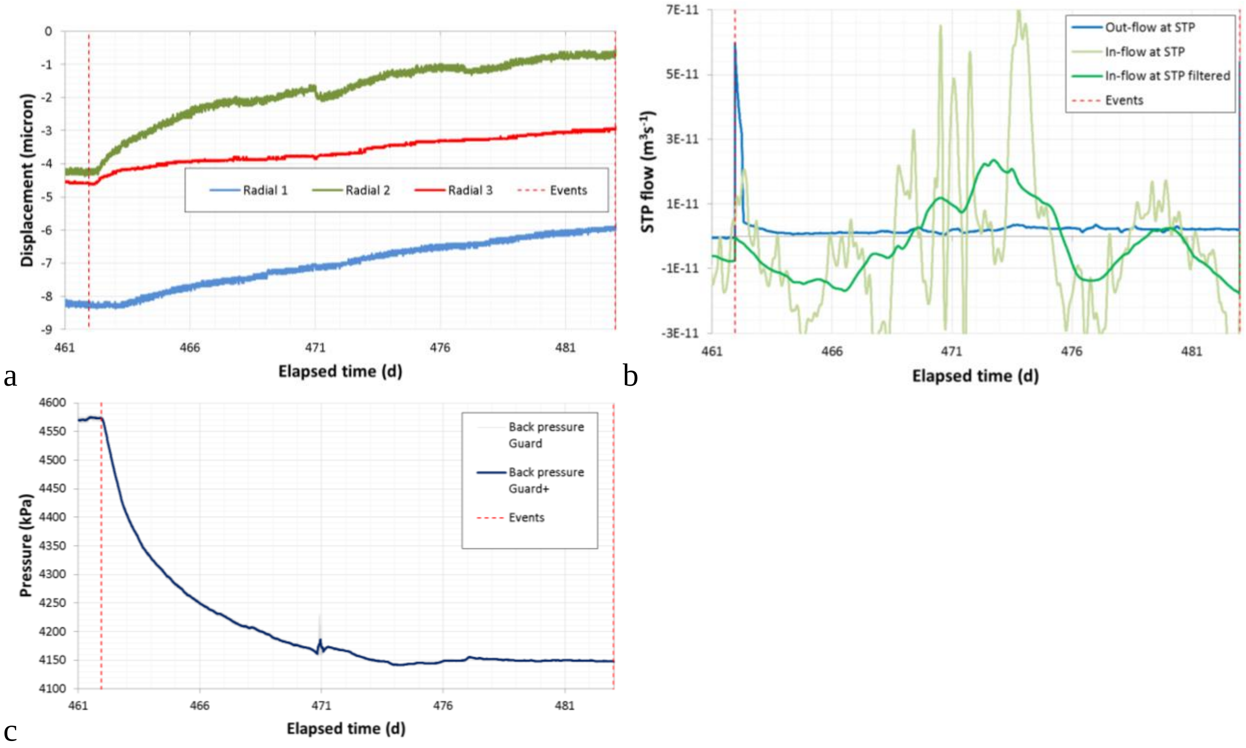

Figure 5-16 Detail of Step 1 of the back-pressure reduction from 4.5 MPa to 3.5 MPa. A) radial strain, b) flow, c) back-pressure guard-ring.

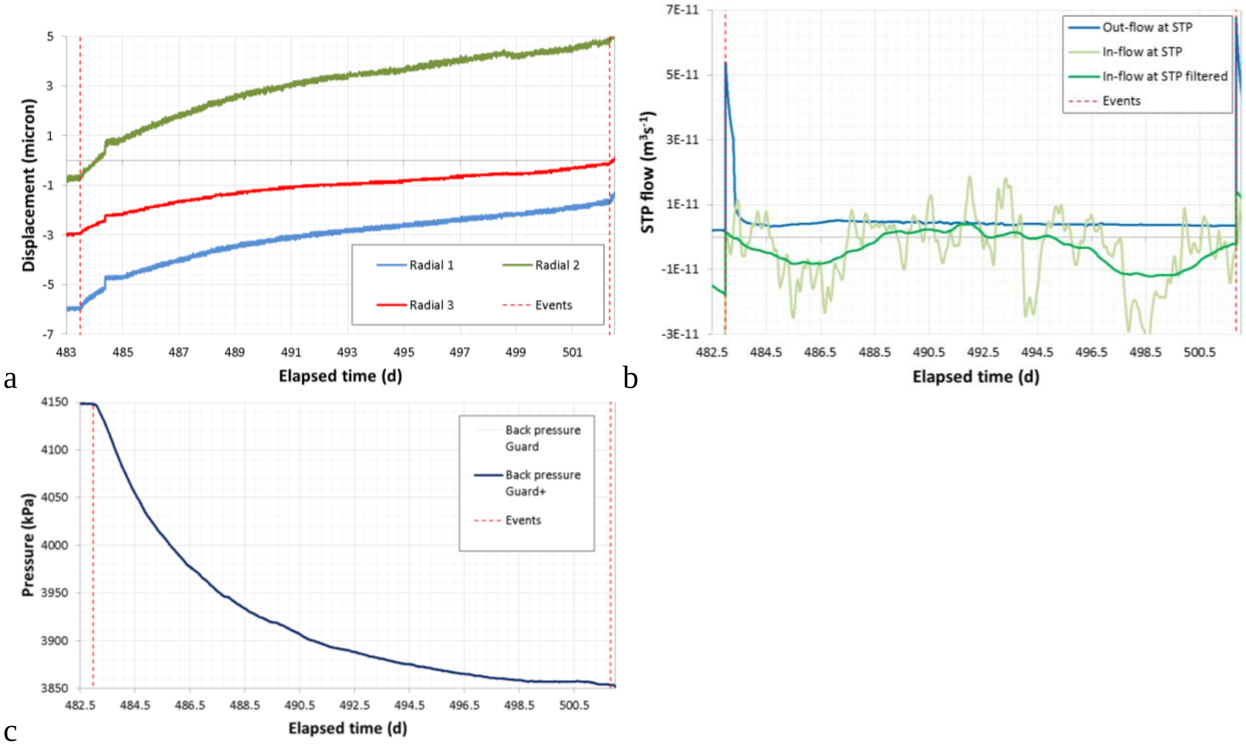

Figure 5-17 Detail of Step 2 of the back-pressure reduction from 3.5 MPa to 2.5 MPa. A) radial strain, b) flow, c) back-pressure guard-ring.

5.6.2 Step 2: Reducing back-pressure to 2.5 MPa

Figure 5-17 shows the detail of the second step of this stage of experimentation with the reduction in back-pressure from 3.5 MPa to 2.5 MPa. As seen, the change in back-pressure resulted in only a small (~75µl) consolidation of the sample volume. During the stage the pressure in the back-pressure guard-ring reduced from 4.15 MPa to 3.85 MPa. The time-dependent nature of the response is due to the drainage of the sample. As a result of drainage, outflow of the sample increased initially and reduced to an asymptote of flow rate of 0.52 µl.h^{-1} (3.4×10^{-12} m^3.s^{-1}) although it has to be noted that due to time constraints full asymptote was not reached. It can be seen that the initial increase in flow was followed by a reduction to a flow of 0.5 µl.h^{-1} (3.0×10^{-12} m^3.s^{-1}) before recovery to a flow rate of 0.75 µl.h^{-1} (5.2×10^{-12} m^3.s^{-1}) followed by decay to the asymptote near 0.52 µl.h^{-1} (3.4×10^{-12} m^3.s^{-1}). During the period inflow into the sample remained constant.

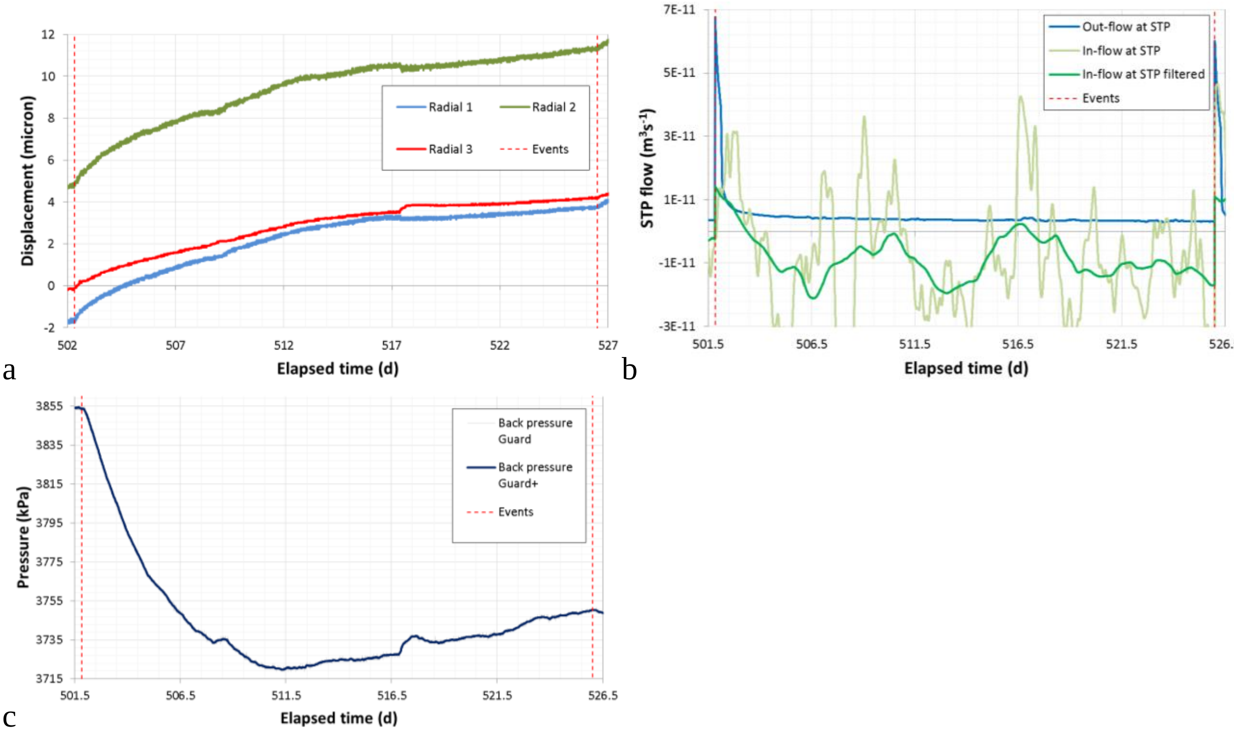

Figure 5-18 Detail of Step 3 of the back-pressure reduction from 2.5 MPa to 1.5 MPa. A) radial strain, b) flow, c) back-pressure guard-ring.

5.6.3 Step 3: Reducing back-pressure to 1.5 MPa

Figure 5-18 shows the detail of the third step of this stage of experimentation with the reduction in back-pressure from 2.5 MPa to 1.5 MPa. As seen, the change in back-pressure resulted in only a small (~100µl) consolidation of the sample volume. During the stage the pressure in the back-pressure guard-ring reduced from 3.85 MPa to 3.72 MPa before increasing to a final pressure of 3.75 MPa. The time-dependent nature of the response is due to the drainage of the sample. As a result of drainage, outflow of the sample increased initially and reduced to an asymptote of flow rate of 0.78 µl.h^{-1} (3.4×10^{-12} m^3.s^{-1}). During the period inflow into the sample remained constant.

5.6.4 Step 4: Reducing back-pressure to 1.0 MPa

Figure 5-19 shows the detail of the fourth step of this stage of experimentation with the reduction in back-pressure from 1.5 MPa to 1.0 MPa. As seen, the change in back-pressure resulted in only a small (~70µl) consolidation of the sample volume. During the stage the pressure in the back-pressure guard-ring reduced from 3.75 MPa to 3.71 MPa before a slight increase in pressure. The time-dependent nature of the response is due to the drainage of the sample. As a result of drainage, outflow of the sample increased initially and reduced to an asymptote of flow rate of 0.9 µl.h^{-1} (2.6×10^{-12} m^3.s^{-1}). During the period inflow into the sample remained constant.

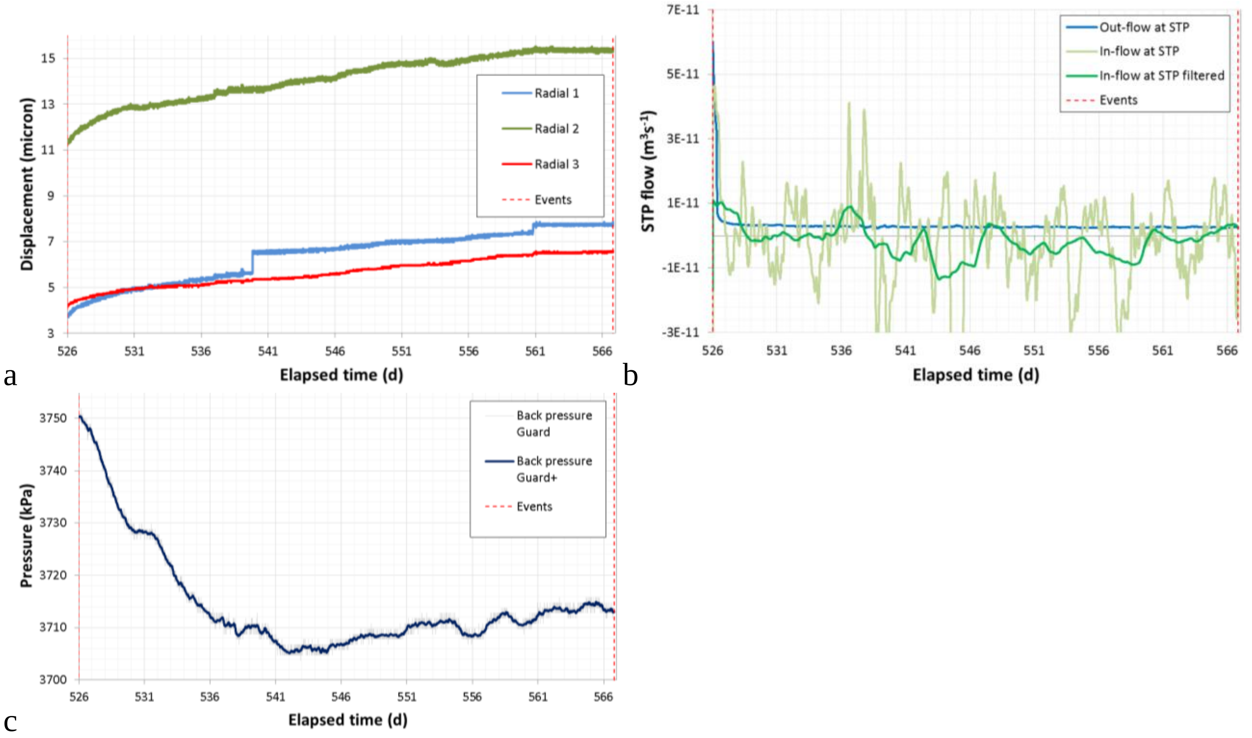

Figure 5-19 Detail of Step 4 of the back-pressure reduction from 1.5 MPa to 1.0 MPa. A) radial strain, b) flow, c) back-pressure guard-ring.

The pressure and flow response seen during several of the steps lowering back-pressure saw an "over-shoot" with flow or pressure reducing, followed by a recovery. This shows the dynamic coupling typical of a hydro-mechanical response.

5.7 POST TEST OBSERVATIONS

The sample was removed from the apparatus on the 23rd May 2012 (Day 566). A total of 18 steps was conducted in order to lower the pressure within the apparatus to atmospheric conditions. Care was taken to ensure that the sample was not placed in extension and that stresses were not emplaced on the sample so as to create failure. The careful lowering of confining pressure, axial stress and pore-pressure in 18 steps means that the potential for failure created by de-pressurisation was minimal. However, the 18 steps were conducted over a period of only a couple of hours, therefore trapped gas within the sample would not have been able to fully drain during de-pressurisation.

The confining fluid was drained once the sample was at atmospheric stresses. It was noted that the glycerol fluid was frothy. Every attempt to eliminate air during the setup of the experiment was taken and it is expected that air content during initial pressurisation was minimal. Therefore it is likely that gas was diffusing through the Hoek sleeve into the confining fluid and this may explain the mass imbalance noted above.

Figure 5-20a shows the sample *in situ* in the experimental apparatus immediately after the loading platen was removed. As can be seen, the majority of the sample end was "wet", whilst the impression of the injection filter appears to show a more dry appearance. This photograph clearly shows a number of fractures in the sample, the most significant runs across the sample from edge to edge, with a secondary fracture seen running from the edge of the injection filter to the outside of the sample. This image shows that all features described in the following paragraphs were unlikely to be formed during the extraction of the sample. However, as previously stated these fractures could potentially have been formed as trapped pressurised gas within the sample expanded during de-pressurisation.

The sample was weighed and measured (see Section 5.7.1) before being carefully examined and photographed. Figure 5-20b to Figure 5-20d show the sample after it was removed fully from the apparatus. The sample end can be seen to be “polished” in places and “rough” in others. It appears that the area close to the injection filter was dry. As the photograph clearly shows a number of fractures have been formed and some of these ran the full length of the sample. The fracture was not planar and in places was made up of a number of intersecting fractures.

The sample was placed within a bath of glycerol and slowly heated. Figure 5-21 shows three photographs of the sample whilst heating. As seen in Figure 5-21a, the majority of escaping bubbles were from the sample ends. However, a number of bubble streams are clearly seen to originate from the length of the sample. Figure 5-21b and Figure 5-21c show a close-up view of the injection end of the sample. As can be observed, gas was seen to escape the sample from a number (10s) of locations. It was evident that the size of the bubble varied, with a few (<5) locations having bubbles significantly larger in size (see Figure 5-21b for two significantly larger bubbles). It has to be noted that a lot more gas was coming out of the injection end, with little gas de-gassing from the back-pressure end. This shows that significantly more gas pathways were formed at the injection end of the sample and only a few of these propagated as far as the back-pressure end. With continued heating, it was seen that a number of gas expulsion sites showed episodic flow, whilst other sites had a continual stream of gas bubbles. This suggests that some pathways were discontinuous, whilst others were continuous and open. It has to be noted that less gas was seen escaping from the sample compared with previous observations of COx (Harrington *et al*., 2012; sample COx-1).

Following heating in glycerol the sample was photographed again. As the glycerol evaporated from the sample surface the fractures were easier to visualise, as seen in Figure 5-22. A series of anastomosing fractures were evident along the length of the sample (Figure 5-22a). Close examination of the fractures (Figure 5-22b and Figure 5-22c) show Mode I (opening) fracturing with little evidence of shear movement. The nature of the fracture resembles a fabric tear, see Figure 5-22c.

Figure 5-20 Observations of the sample SPP_COx-2 prior to heating in glycerol. A). *in situ* in the experimental apparatus prior to sample extraction (back-pressure end), b). the back-pressure end of the sample, c). the injection end of the sample, d). a fracture running the full length of the sample.

Figure 5-21 Observations of sample SPP_COx-2 during heating in glycerol.

Figure 5-22 Observations of sample SPP_COx-2 after heating in glycerol.

5.7.1 Post-test saturation

The sample was re-tested for final saturation at the end of the experiment. The sample was weighed immediately after extraction from the apparatus and recorded a weight of 497.7 g. A total of twelve sample diameter readings were taken, along with five length measurements. After being submerged in glycerol (see above) the sample was placed in the oven for one hour and the weight of the sample was recorded as 484.8 g. As can be seen in Figure 5-23, the sample was put in the oven for a prolonged period in order to dry fully. As seen it took in excess of one week for the sample weight to equilibrate at a final dry weight of 465.1 g.

	Units	**Value**	**Value**	**Change**
Time of measurement		Before gas testing	After gas testing	
Average length	mm	82.45 ± 0.03	82.57 ± 0.03	+ 0.12
Average diameter	mm	55.85 ± 0.04	55.95 ± 0.08	+0.1
Volume	m^3	2.020×10^{-4}	2.030×10^{-4}	$+0.01 \times 10^{-4}$
Average weight	g	495.02	497.69	+ 2.67
Density	$g.cc^{-1}$	2.451	2.452	+ 0.001
Grain density	$g.cc^{-1}$	2.7	2.7	/
Moisture weight	g	28.7	32.6	+ 3.9
Moisture content	%	6.2	7.0	+ 0.8
Dry weight	g	466	465	- 1
Dry density	$g.cc^{-1}$	2.31	2.29	- 0.02
Void ratio		0.174	0.183	+ 0.009
Porosity	%	14.8	15.5	+ 0.7
Saturation	%	96	100	+ 4

Table 5-7 Dimensions and basic properties of the Callovo-Oxfordian claystone test material (sample SPP_COx-2). The data from pre-test measurements of water content from off-cut material adjacent to the core, data for final post-test measurement are directly from the sample. An assumed specific gravity for the mineral phases of 2.70 $Mg.m^{-3}$ (Zhang *et al.* 2007) was used in these calculations.

The sample was weighed, which allowed bulk density to be determined. Table 5-7 shows the pre- and post-test physical properties of the specimen based on the moisture content of the off-cuts (for pre-test), the test sample (for post-test) and a grain density of 2.70 Mg m^{-3} (Zhang *et al.*, 2007). The data presented in Table 5-7 is in good agreement between samples and with the generic values quoted by Zhang *et al.* As can be seen, the test sample increased in volume by approximately 1 cc.

The final saturation of the sample was calculated to be indistinguishable from unity and clearly demonstrates that even after prolonged periods of gas flow through the COx that no measureable desaturation occurred.

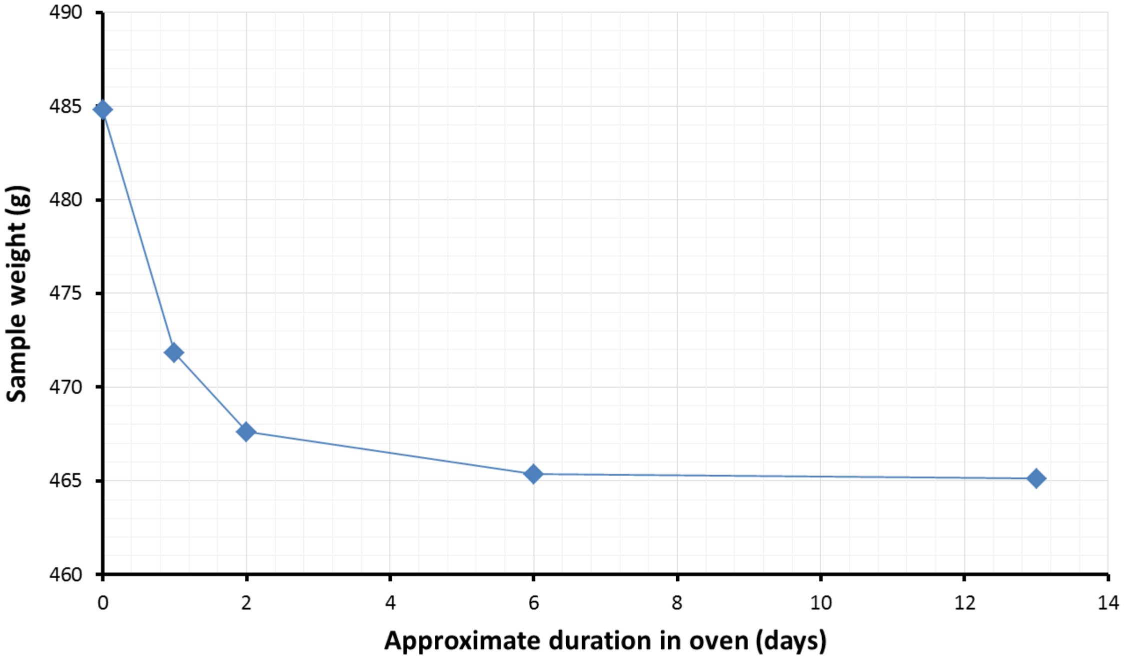

Figure 5-23 Weight of the final sample after a prolonged period of time in the oven.

6 Discussion

The stress-path permeameter was seen to perform very well during testing. The radial displacement data has been invaluable in understanding the deformation of the sample during the stress-path testing and also in identifying the subtle volumetric strain seen at the onset of gas flow through the sample.

6.1 MECHANICAL DEFORMATION

Many of the observations noted show that the Callovo-Oxfordian claystone is highly time-dependent in its deformation. During the initial stage of test SPP_COx-1 the sample swelled and the apparatus successfully measured this deformation. During the successive stages the sample deformed quickly to the change in stress state and showed considerable time-dependent creep during all stages of the test. As the test went on the amount of creep observed increased. However, during each step equilibrium had not been achieved so this may be superposition of deformation from stage to stage. This hypothesis is strengthened by the observations of stages three and seven. Stage three achieved equilibrium and the amount of creep observed in stage four was similar. This showed that creep was present in the sample even after equilibrium had been achieved. During stage seven the sample was held constant for a prolonged period of time and as a consequence the following stage (eight) showed less creep. It is possible that a certain component of the observed creep is caused by pore-pressure and drainage, which due to the low permeability of the sample takes time to homogenise within the sample. A secondary component of creep was caused by the time-dependent deformation (true creep) of the rock.

There were several implications of the observed creep. For the experimental study it meant that each stage of the test had to be conducted to the point of equilibrium. This lengthened the time each step had to be conducted and limited the scope of the full experimental programme. The observed creep also placed a question as to whether deformation in COx is rate-dependent. The time-dependency suggests that heterogeneous pore-pressure distributions are created in deforming samples and that failure may result at different stress levels. Therefore a test conducted quickly may predict a weaker strength than one conducted slowly. This suggests that care should be taken when comparing data from different sources that have used different apparatus, different sized samples, drained or undrained conditions etc. This may explain why failure occurred at a stress-state higher than that predicted for COx by the Hoek-Brown failure criterion. It is also interesting that failure occurred 5.5 days into a constant stress-state step. This begs the question whether ultimate failure would have occurred during the previous stage if it had been left longer, although this is unlikely.

The observed behaviour of pore-pressure at the guard-rings is intriguing. For all stress steps the pore-pressure initially dropped and within a day or two reached a minimum. During each step the axial load was increased and the confining pressure was lowered. It is likely that the pore-pressure response was showing that dilation was occurring which was causing fluid to flow away from the corners of the sample. Once the pressure minimum had been reached, in all but one of the steps the pressure began to rise. This suggests that the deformation at first results in fluid moving away from the sample corners and that with time it is drawn back. This could either be the fluid expelled from the corners returning or pore fluid from the injection point flowing into the now lower-pressure zone. In the early stages of the test (stage 1-7) it was observed that pore-pressure generally returned to that seen at the start of the stage. In later stages it was observed that full pressure recovery was not achieved and over time the pore-pressure at the guard-rings reduced. This may be the result of not conducting each step for sufficiently prolonged time, but may also be indicative of permanent damage occurring to the sample. The observations at the guard-ring show that pore-pressure distribution within the sample was highly complex.

Considerable anisotropy was observed in radial deformation. At all stages it was observed that Radial 1 showed the most deformation, followed by Radial 3 and Radial 2 respectively. This anisotropy will have influenced the formation of the fault in the sample; however the orientation of the fracture was not recorded with respect to the orientation of Radial 1-3.

6.2 ADVECTIVE GAS FLOW

6.2.1 Dilatancy observed at the onset of gas flow

Figure 6-1 shows the interpretation of the onset of gas migration in COx. The data suggest that the first gas entry into the sample occurred at Day 220 when the gas injection pressure was 10 MPa, this was seen as gas reaching the injection-end load cell. At this time the experiment was operated as constant pressure and evidence suggests that gas reached the load-cell, but did not propogate significantly further. A second event was recorded by the load cell at Day 237.32, with pressure increasing in the injection guard-ring at Day 238.55. A day later at Day 239.8 the first indiciation of deformation was recorded at the mid-plane array of radial strain measurement devices. Deformation continued and accellerated approaximately 15 days later.

Stage 1 of gas migration: Figure 6-1a shows the first stage of gas migration. At about Day 220 gas started to enter the sample when the gas injection pressure was 10 MPa (gas breakthrough excess pressure of 5.65 MPa). Gas migrated as far as the load-cell, where it was identified as an anomalous reading. The onset of gas migration may be indicated by a change in slope of the comparison of predicted gas pressure versus observed pressure. It is probable that gas had migrated along a single bedding layer of the COx as the test sample was oriented parallel to bedding. Gas propogation was along dilatant pathways that exploited the pore network of the material. The pathways can be visualised as “ruptures” in the pore network. Around each pathway the fabric would have compressed, which may lead to localised movement of water away from the pathways.

Stage 2 of gas migration: Figure 6-1b shows the second stage of gas migration. Gas propogation throughout the sample was migrating further and had reached the corner of the sample, as seen by the onset of pressure rise at the guard-ring. The geometry of the SPP apparatus means that gas was injected horizontally at one end of the sample, whereas in other apparatus gas is injected at the bottom of the sample. As a result when gas reaches the injection guard-ring it will displace water from the guard-ring into the sample until the guard-ring was saturated with gas. This means that early in the gas migration water was being displaced into the sample, which would result in swelling if the sample was not fully saturated. This stage was identified by a slow increase in injection guard-ring pressure. The start of the stage occurred at Day 237.32 with a second anomalous reading in the injection-end load cell signifying the movement of gas. Pressure in the guard-ring started to increase at Day 238.55. A day later at Day 239.8 the first indiciation of deformation was recorded at the mid-plane array of radial strain measurement devices. This initial strain may have been as a consequence of water expulsion from the guard-ring and small amounts of sample swelling.

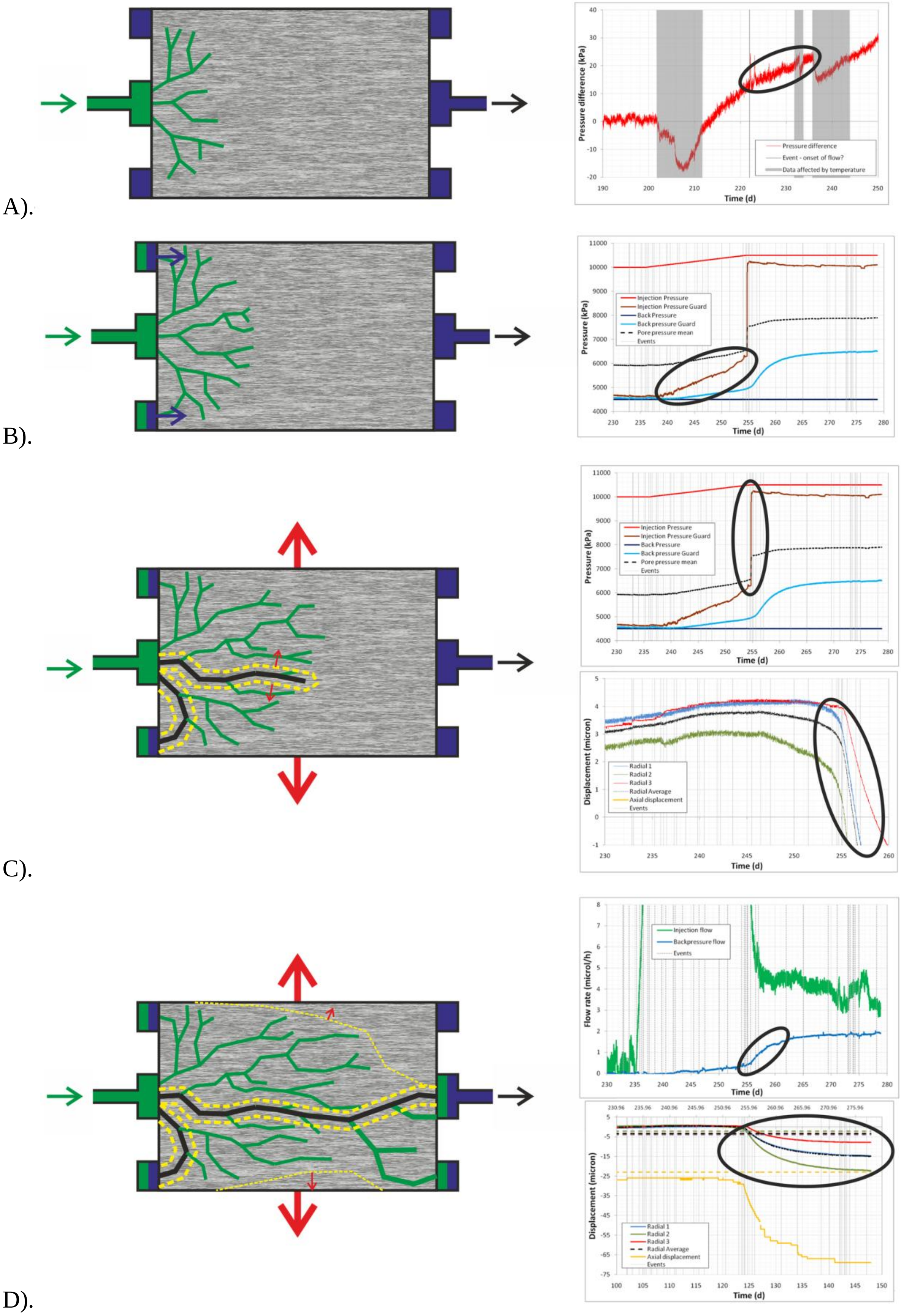

Figure 6-1 Interpretation of the onset of gas flow in COx. A) The onset of gas flow. B) Gas reached the injection-end guard-ring and displaced water into the sample. C) A more significant feature was created causing the pressure in the guard-ring to increase and the sample to start to dilate. D) Gas migration had reached the back-pressure end as seen in a rise of outflow. As more pathways were opened the sample continued to dilate.

Stage 3 of gas migration: Figure 6-1c shows the third stage of gas migration. A large increase in pore-pressure at the injection guard-ring occurred at Day 238.55 and was likely to be the result of a major conductive feature being formed in the sample. As this propagated through the sample it resulted in an accelelration of dilatant deformation. It can be seen that the accelleration of deformation at the mid-plane first occurred 32 days after the first sign of gas migration at Radial 2. Dilatant deformation increase occurred 0.7 days later in Radial 1 and a further 0.4 days later in Radial 3. However, axial deformation did not start to accellerate until 11 days after Radial 2. If all of the observed radial deformation was as a result of water being displaced from the guard-ring into the sample it would be expected that axial deformation would have reacted first. Therefore the observed dilatancy cannot be described completely as caused by swelling. Stage 3 also shows the onset of outflow of fluid from the sample and therefore must indicate gas movement. If all deformation was explained as derived from swelling this would not result in outflow from the sample. Therefore, even though the experimental geometry is likely to result in swelling the majority of observed deformation was caused by the dilatant propagation of gas along pathways.

Stage 4 of gas migration: Figure 6-1d shows the fourth stage of gas migration. Gas had propagated through the sample as far as the back-pressure end. The onset of gas reaching the back-pressure guard-ring at Day 273 indicated that gas was now moving throughout the entire length of the sample. During this stage the sample continued to dilate, which may indicate that the number of gas pathways was increasing.

Observed events (see Table 6-8) show that gas reached the injection guard-ring at Day 238.55, dilatancy was first seen at the mid-plane at Day 239.8 and the back-pressure guard-ring started to increase at Day 240.5. This means that the pressure pulse propogated at a rate of approximately 37.6 mm.day^{-1} or 1.6 mm.h^{-1}. This is interpreted as being a hydro-mechanical response and is created by a change in effective stress as gas started to propogate into the sample.

	Event	Time (Days)	Distance from injection (mm)	Flow (μm.h^{-1})
Hydro-mech	Gas inferred at load cell location	237.07	2.00	/
	Pressure rise in injection guard-ring	238.55	12.00	(675)
	First evidence of dilatation at mid-plane	239.80	41.25	(1250)
	Pressure rise in back-pressure guard-ring	240.50	82.50	(2000)
Gas migration	Gas inferred at load cell location	237.07	2.00	/
	Significant jump in pressure at guard-ring	254.70	12.00	28.3
	Onset of accelerated mid-plane dilation	255.00	41.25	95.9
	Onset of gas at back-pressure guard-ring	273.00	82.50	98.4

Table 6-8 Summary of events that represent the migration of gas through the COx.

The accelleration of strain at the mid-plane occurred at approximately Day 255, whereas pressure at the back-pressure guard-ring initiated at Day 240.5 (nearly 15 days previous). This suggests that the back-pressure response was a hydromechanical response, whereas the accellerated dilatation was one of gas movement. The pressure increase in the injection pressure guard-ring was unstable and this was indicative of gas propogation, whereas the pressure increase at the back-pressure guard-ring was gradual and suggests that this response was not indicative of gas reaching the back-pressure end of the sample and was the result of the hydromechanical coupling. Gas was inferred as reaching the back-pressure end at Day 273. As shown in Table 6-8, the accelleration of dilation caused by the propogation of dilatant gas pathways at the mid-plane and onset of gas reaching the back-pressure end give a gas propogartion rate of approximately 100 μm.h^{-1}. This means that per annum gas may have moved 0.85 m.

Our interpretation has three components; 1) a response caused by the expulsion of water from the injection guard-ring due to the geometry of the test set-up and the resultant swelling of COx; 2) a hydro-mechanical response of the COx as a result of the change of pore-pressure from ambient (4.5 MPa) to the injection gas pressure (10 MPa); 3) a dilatant response as gas propogated through the sample. It is difficult to decouple all three components, but it is difficult to interpret the data in terms of just two-phase flow concepts.

6.2.2 A general model for gas flow in COx

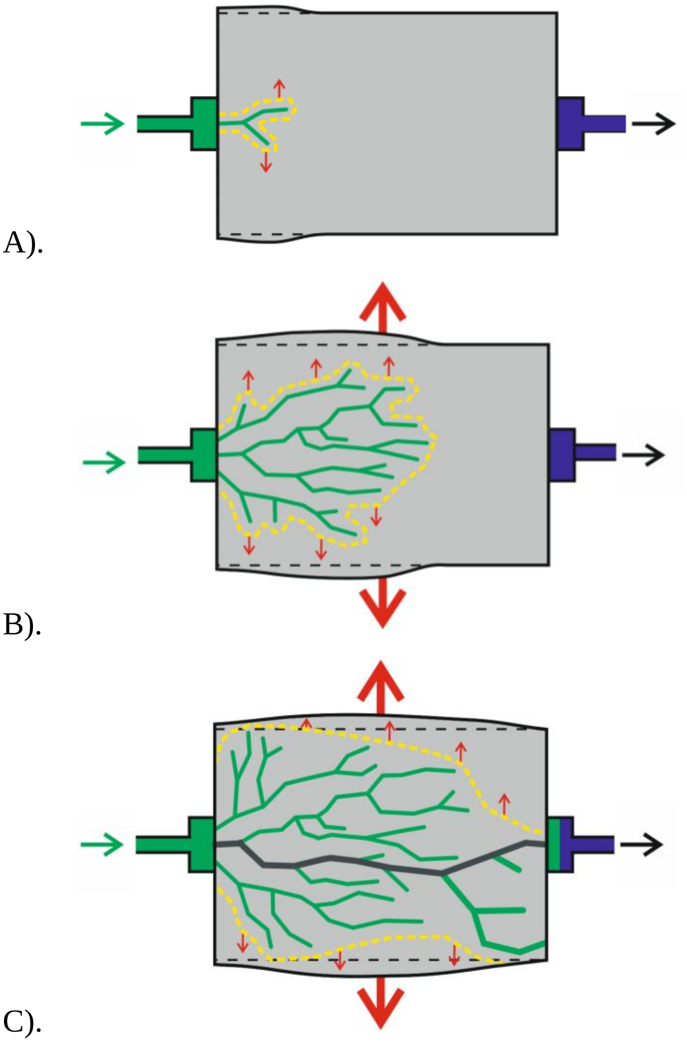

Figure 6-2 A general model for the onset of advective gas flow in Callovo-Oxfordian claystone. A) The onset of gas flow when gas started to enter the sample at the injection port. Each gas pathway causes compaction of COx around the pathway, causing bulk sample dilation. B) A dendritic pattern of gas pathways formed, slowly propagating through the sample. Significant dilation was observed at the mid-plane as the pathways propagate past this location. C) Gas migration had reached the back-pressure end of the sample as seen in a rise of outflow. As more pathways were opened the sample continued to dilate.

Using all of the observations of the current study, combined with observations from isotropic testing of the COx (Harrington *et al*. 2010), flow experiments conducted in COx at LAEGO, Nancy (Cuss *et al*., 2013), and experimental results in other argillaceous materials (Angeli *et al*., 2009; Autio *et al*., 2006; Gallé & Tanai, 1998; Harington & Horseman, 1994, 1997, 1999; Harrington *et al*., 1999, 2009, 2012^{a,b}; Horseman *et al*., 1996, 2004; Ortiz *et al*., 1996, 2002) it is possible to create a general model for the onset of advective gas flow in Callovo-Oxfordian claystone. Figure 6-2 shows the interpretation of the onset of gas migration in COx. A three stage interpretation has been postulated, which fit all of the observations of the BGS and previously published results.

Stage 1 (Figure 6-2a): At the gas entry pressure, gas began to enter the sample. It is probable that gas migrated along a single bedding layer of the COx as the test sample was oriented parallel to bedding. Gas propagation was along dilatant pathways that exploited the pore network of the material; the pathways can be visualised as “ruptures” in the pore network. Around each pathway the fabric compressed, which may lead to localised movement of water away from the pathways.

Stage 2 (Figure 6-2b): The dendritic network of dilatant pathways propagated further into the sample and reached the mid-plane. This resulted in an acceleration of dilatant deformation. Stage 2 also showed the onset of marked outflow from the sample. If all deformation was explained as derived from swelling this would not result in outflow from the sample.

Stage 3 (Figure 6-2c): Gas had propagated through the sample as far as the back-pressure end. The onset of gas reaching the back-pressure guard-ring indicated that gas was now moving throughout the entire length of the sample. During this stage the sample continued to dilate, which may indicate that the number of gas pathways was increasing. Stage 3 can be seen to be the formation of a major conductive feature that connected both ends of the sample. These major features may have been the formation of dilatant fractures as seen in the sample at the end of the test.

6.2.3 Flow shut-off

It was unexpected that whilst waiting for flow to reach steady-state conditions, outflow from the sample started to reduce about Day 320. It was observed that inflow showed an increase prior to the reduction in outflow, peaking at approximately Day 311, and this may have been the driver for the reduction in outflow. The reduction of outflow corresponds with a change in radial strain (contraction of the sample), a reduction of inflow and a reduction of pressure in the back-pressure guard-ring. A few days following the reduction of outflow the injection-end guard-ring pressure increased to approximately equal the injection pressure, this event corresponds with a short-lived peak of inflow. This could be interpreted as flow along the loading platen and the direct connection of the guard-ring and injection port. On retrieval of the sample from the apparatus it was seen that the sample was fractured and small mode-I type fractures could be seen linking the injection port and the guard-ring. This might suggest that the reduction in flow and increase in guard-ring pressure were related to the formation of the observed fractures. However, the opening of mode-I fractures would result in an increase in effective porosity, net volumetric dilation of the sample, an increase of inflow, and if the fracture runs the full length of the sample an increase of outflow; i.e. the fracture would transmit increased amounts of gas. A small increase in axial strain was seen corresponding with the onset of flow reduction, although no radial strain was seen. The formation of a mode-I fracture at the back-pressure end of the sample may explain the reduction in pressure of the back-pressure guard-ring to equal the same pressure as the back-pressure. The fracture would result in the drainage of the guard-ring. However, this would expect to result in an increase of outflow as the guard-ring drained.

Whilst there is evidence of fracturing seen post-testing, the complete dataset does not indicate a clear timing of the formation of these fractures. It is possible that these features were formed at the time of lowering test pressure to ambient levels. This would result in the expansion of trapped gas and if this gas was not able to drain it would result in mode-I fracturing. There is clear evidence of multiple pathways forming through the sample and these may have been the cause of the increase in pressure of the guard-ring. The absence of marked, short-term, radial strain that would be expected during the rapid propagation of fractures suggests that the fracturing occurred during decommissioning of the test.

One hypothesis for the reduction of flow could be the short circuit of the injection end of the sample by fracturing or pathway formation and the increased pressure at the guard-ring resulting in leakage of gas either through the Hoek-sleeve/platen interface or by diffusion through the Hoek-sleeve. The decommissioning of the test did observe a “frothy” nature to the confining glycerol that may indicate that gas was entering the confining system. However, close examination of all behaviour means that gas leakage can be discounted as the cause of the shut-off. At the start of flow reduction it can be seen that inflow increased, meaning it is possible a fracture or conductive pathway formed at this time at the injection end of the sample. However, following this event, flow at the injection end reduced to a condition of no-flow. If shut-off was the result of gas leakage from the apparatus it would be expected that inflow would have increased. It would then be expected that the pressure in the conductive pathways would reduce as gas was lost and this could result in the closure of the formed dilated pathways. The reduction of inflow does not support this hypothesis, nor does the retention of high pressure in the injection guard-ring. The change in confining system volume suggests that no significant gas volume was added to this part of the experimental system. Therefore, although gas leakage from the system cannot be ruled out, it is unlikely to be the cause of the shut-off.

The lowering of confining pressure confirmed that direct communication of the guard-rings and corresponding injection-/back-pressure ports was occurring. The lowering of the confining pressure did not cause closure of the connective features.

It can be seen that by the end of the shut-off period most of the sensor values were similar to when at the point of initiation of gas flow; i.e. radial strain had recovered; back-pressure guard-ring pressure was similar to back-pressure. However, the injection guard-ring was greatly elevated in pressure. A degree of permanent deformation was noted and this is likely to correspond with gas trapped within the sample.

The raising of the injection gas pressure did not result in the re-opening of the conductive features within the sample and outflow and inflow remained low. Therefore, the cause of self-sealing was effective and the sample was now sustaining higher gas pressures without flow through the sample. This suggests that some form of localised consolidation must have occurred near to the injection port.

The cause of shut-off is therefore unknown. Experimental evidence suggests that mode-I type fractures may have been the cause of the shut-off, although the inflow and outflow data do not support this hypothesis.

6.2.4 Lowering of back-pressure

In order to re-initiate gas flow, the back-pressure was lowered in steps from 4.5 MPa to 1 MPa. This has the result of increasing effective stress and increases the gas gradient along the length of the sample. As could be seen, this did not result in re-initiating flow through the sample and only resulted in draining the sample, leading to compaction.

The first step of the test reduced back-pressure from 4.5 MPa to 3.5 MPa. This resulted in a reduction in pressure at the back-pressure guard-ring (BGR) to 4.15 MPa. This shows that the back-pressure systems were no longer in direct contact. Therefore if these had been connected by a tensile mode-1 fracture, this had closed and was no longer conductive. Further reduction of the back-pressure to 1 MPa resulted in the BGR pressure reducing to a steady 3.7 MPa. This value may represent the capiliary threshold pressure, but this pressure also may be the result of gas trapped within the guard-ring not being able to drain, resulting in an elevated pressure.

In lowering back-pressure, outflow from the sample increased and quickly reduced. In several of the steps outflow reduced and recovered before slowly decaying again. This over-shoot of flow is linked to the hydro-mechanical behaviour of the sample and is characteristic of unstable flow. In later stages, i.e. for 1.5 MPa and 1 MPa back-pressure, similar behaviour was seen in the back-pressure guard-ring response, with pressure recovering after an initial reduction.

At the end of each back-pressure reduction stage it can be seen that outflow from the sample was still occurring. However, for all steps there was still a reduction in outflow. Time constraints meant it was not possible to allow flow to reduce to a condition of no flow. Therefore it would appear that the reduction in back-pressure has increased the resultant outflow. This can be explained as sample drainage. For sample SPP_COx-1 it was shown that large samples of COx have considerable time-dependent deformation that is a combination of material creep and drainage. Therefore the outflow seen was the result of this considerable time-dependent behaviour. It can be seen that outflow from both ends of the sample are remarkably similar showing that the outflow is the result of sample drainage and not related to gas flow through the sample.

The experimental setup was not able to determine the phase of the outflow, be it gas or water. The final saturation of the sample was determined to be indistinguishable from 100%. Therefore it is likely that outflow was the expulsion of gas, and possibly free water, from the sample as a result of bulk compaction.

The lowering of back-pressure was an analogue of the stress-path modification that occurs during tunnel advancement. Therefore during tunnelling the wall-rock consolidates, which will result in the raising of the gas entry pressure. In tunnel construction there will be an increase in stress caused by stress concentrations around the tunnel wall. This results in fracturing and the formation of the Engineered Damaged Zone (EDZ), with fractures that are significantly greater in permeability/transmissivity than intact COx.

It has been shown that a reduction in back-pressure results in bulk sample volume reduction. This consolidation increases gas entry pressure. During the shut-off stage it was seen that the reduction in pressure at the back-pressure guard-ring (BGR) was the first recorded event. It is possible that this lowering of pressure resulted in localised consolidation and that this caused the flow to shut-off. The cause of the reduction in BGR pressure has been suggested to have been the formation of a conductive micro-fracture linking the guard-ring with the pressure port. It may be possible that the formation of the fracture/conductive pathway ultimately resulted in the closure of flow through the sample due to the localised nature of the flow paths and their inherent instability being strongly linked with the consolidation of the sample.

6.3 COMPRESSIBILITY AND OBSERVATIONS OF PORE-PRESSURE IN COX

The injection of gas into COx will increase the pore-pressure within the sample from 4.5 MPa to the gas injection pressure (approximately 10.5 MPa). This increase of pore-pressure of 6 MPa can be viewed as being a change in effective stress on the overall sample of the same amount.

Water is a compressible medium with a bulk modulus of 2.2 GPa. The starting moisture content of the sample was calculated to be 28.7 g (i.e. 28.7 ml). The expected change in volume of water for this pressure change can be calculated from:

$$K = -V \frac{dP}{dV}$$

where K is the bulk modulus (2.2 GPa), V = volume of water (28.7 ml), dP is the change in pressure (6 MPa) and dV is the resultant volume change. Therefore:

$$dV = -V.\frac{dP}{K}$$

This gives a change in volume as a result of pressure change of 78 µl. This is much less (~20 %) of the total sample deformation recorded of 360 µl.

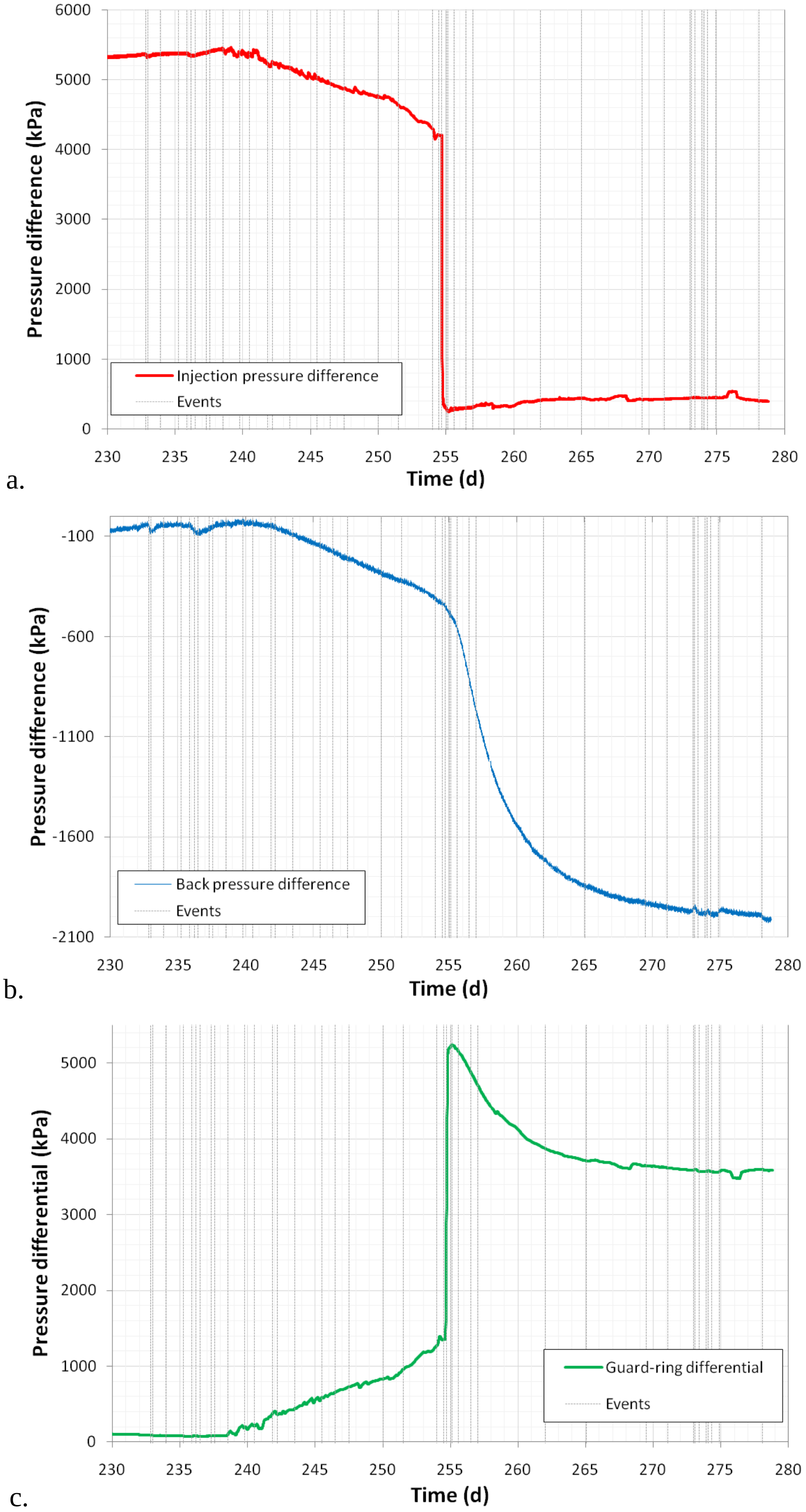

Figure 6-3 Pore-pressure differentials observed within the sample. A) difference between injection pressure and injection guard-ring; b) difference between back-pressure and back-pressure guard-ring; c) difference between injection guard-ring and back-pressure guard-ring.

Figure 6-3 shows interesting data about the large pressure differentials observed within the COx. Figure 6-3a shows the difference between the injection pressure port and the injection-end guard-ring. It should be noted that the distance between these is merely 12 mm between the 20 mm diameter injection frit and 6 mm-wide guard-ring. As seen the pressure difference was in excess of 5.3 MPa, which represents a pressure gradient in excess of 400 MPa.m^{-1}. It can be seen that even after the pressure increased in the guard-ring there is still a pressure differential of a few hundred kilopascals.

The pressure differential was not as pronounced at the back-pressure end of the sample (Figure 6-3b), where initially a very small differential was observed, which resulted in a difference of approximately 2 MPa, which represents a pressure gradient in excess of 160 MPa.m^{-1}.

Marked pressure differential was observed between the injection and back-pressure ends of the sample at the guard-rings (Figure 6-3c). This differential peaks at a value greater than 5 MPa, representing a pressure gradient of 65 MPa.m^{-1}. This differential pressure decays to a steady 3.5 MPa.

The pressure differential observed within COx during testing (as seen in hydraulic and gas testing) leads to very high pressure differentials that appear to be stable. One of the main tenets of rock deformation is that of the law of effective stress, where the stress acting on a sample can be viewed as the total stress minus the pore-pressure (Terzaghi’s law of effective stress; Terzaghi, 1943). It has been well documented that soil-like materials do not perfectly follow Terzaghi’s Law, but this can be modified by a constant. The observed pore-pressure within the current test leads to the question what is the effective stress acting on the sample? We have four different measures of pore-pressure (injection, back-pressure, injection guard-ring, back-pressure guard-ring) and at all times of the experiment these are showing different readings, partly as a result of the boundary conditions imposed on the sample. However, it is clear that COx can accommodate very high stable pressure gradients over very small distances and this is problematic in trying to describe deformation in terms of effective stress.

The observed differences in pore-pressure show that the entire water content of the sample has not undergone a 6 MPa reduction in pressure. A mean pore-pressure of 7.9 MPa was observed which gives a change in average pore-pressure of just 3.4 MPa. This would give an elastic deformation of 40 µl. Therefore the full deformation seen by the sample cannot be explained by elastic deformation of the sample water alone.

7 Summary

The bespoke Stress-Path Permeameter (SPP) has been constructed in order to follow specific stress-paths, whilst allowing volumetric deformation to be monitored during deformation. The apparatus was fully calibrated and shown to perform well. This report describes two experiments conducted on Callovo-Oxfordian Claystone (COx) in order to understand the mechanical deformation of the intact material (SPP_COx-1) and to examine the mechanical response of COx during gas propagation (SPP_COx-2). The radial displacement data has been invaluable in understanding the deformation of the sample.

The original experimental programme aimed to examine the change in gas flow properties during a stress-path. Test SPP_COx-2 showed a gas entry pressure much greater than had been anticipated and as this pressure was close to the confining pressure it was difficult to perform a stress-path experiment. The Hoek-sleeve of the apparatus requires a confining pressure greater than pore-pressure in order to achieve a seal. Therefore raising gas pressure greater than confining pressure is highly likely to lead to jacket failure. As a result of this experimental limitation, gas flow for a static boundary condition representative of the *in situ* conditions for Bure were investigated in detail.

Test SPP_COx-1 (mechanical deformation)

The Callovo-Oxfordian claystone is highly time-dependent in its deformation. During the initial stage of the test the sample swelled and the apparatus successfully measured this deformation. During the successive stages the sample deformed quickly to the change in stress state but showed considerable time-dependent creep during all stages of the test. As the test progressed the amount of creep observed increased. However, during each step equilibrium had not been achieved so this may be superposition of deformation from stage to stage. This hypothesis is strengthened by the observations of stages three and seven, which were prolonged stages and were followed in successive steps by a decrease in time dependent deformation. A certain component of the observed creep is caused by pore-pressure, which due to the low permeability of the sample takes time to homogenise within the sample, i.e. is the result of drainage. A secondary component of creep is caused by the time-dependent deformation (true creep) of the clay minerals.

There are several implications of the observed creep. For the experimental studies it means that each stage of testing has to be conducted to the point of equilibrium. This greatly lengthens the time each step has to be conducted. The observed creep also places a question as to whether deformation in COx is rate-dependent. The time-dependency suggests that heterogeneous pore-pressure distributions are created in deforming samples and that failure may result at different stress levels. Therefore a test conducted quickly may predict a weaker strength than one conducted slowly. This suggests that care should be taken when comparing data from different sources that have used different apparatus, different sized samples, drained or undrained conditions etc. This may explain why failure occurred at a stress-state higher than that predicted for COx by the Hoek-Brown failure criterion. It is also noted that failure occurred 5.5 days into a constant stress-state step when the boundary condition was maintained constant.

The time-dependent nature of deformation observed and possible rate-dependency of deformation also means that experimental data may not be applicable for all applications. For instance, tunnelling results in a rapid change in stress where the COx is unable to sufficiently drain. Convergence post-closure is a much longer process where drainage can be accommodated. Therefore long-term experiments will over-predict the strength and gas entry pressure for tests representative of stress-paths created during tunnelling and short-term experiments will under-predict strength and gas entry pressure for post-closure scenarios.

The observed behaviour of pore-pressure at the guard-rings is complex. For all stress steps the pore-pressure initially drops and within a day or two reaches a minimum. During each step the axial load is increased and the confining pressure is lowered. It is likely that the pore-pressure response is showing that dilation is occurring which is causing fluid to flow away from the corners of the sample where the guard-rings are located. Once the pressure minimum has been reached, in all but one of the steps the pressure begins to rise. This suggests that the deformation at first results in fluid moving away from the sample corners and that with time it is drawn back to the corners. This could either be the fluid expelled from the corners returning or pore fluid from the injection point flowing into the now lower-pressure zone. In the early stages of the test (stage 1-7) it was observed that pore-pressure generally returned to that seen at the start of the stage. In later stages it was observed that full pressure recovery was not achieved and over time the pore-pressure at the guard-rings reduced. This may be the result of conducting each step for insufficiently prolonged time, but may also be indicative of permanent damage and/or dilation occurring to the sample. The observations at the guard-ring show that pore-pressure distribution within the sample is highly complex.

Considerable anisotropy was observed in radial deformation. At all stages it was observed that Radial 1 showed the most deformation, followed by Radial 3 and Radial 2 respectively. This anisotropy will have influenced the formation of the fault in the sample; however the orientation of the fracture was not recorded with respect to the orientation of Radial 1-3. The anisotropy observed may be the result of the sample being oriented parallel to bedding and differences in deformation of the layers seen within COx.

The final test stage showed considerable deformation, with SPP_COx-1 failing following the formation of a fracture/fault oriented approximately 30° to the length of the sample. It is observed that this fracture appears to intersect both corners of the sample and this may be the result of edge effects created by friction acting along the ends of the sample between rock and steel platten. A series of fractures parallel to the main fracture could be seen, as well as a series of conjugate fractures.

Test SPP_COx-2 (gas transport)

During the initial pressurization of the sample approximately 0.11 % volumetric strain was observed. The generation of pore-pressure and rehydration of the sample results in approximately 0.12 % dilational volumetric strain. By Day 21 this swelling strain had equilibrated.

A two-stage constant head test was conducted; pore-pressure was raised to 8.5 MPa and the guard-rings were isolated. Both injection and back-pressure end guard-rings showed an initial decrease in pore-pressure, which within a couple of days started to recover in pressure and equilibrated. The injection end stabilised approximately 1 MPa below the injection pressure, whereas the back-pressure was about 0.5 MPa above the back-pressure. Flow data shows that in the first 7 days of the hydraulic test there was no flow at the back-pressure end of the sample. On Day 62 the back-pressure flow started to increase, reaching a steady-state flow of approximately 1 µl.h^{-1} by Day 87. At the onset of flow out of the sample the bulk sample volume increased, resulting in an additional 0.015 % of volumetric strain being generated (approximately 30 µl volume). The onset of flow also resulted in the guard-ring pressure changing at both ends of the sample, with the back-pressure end having a larger increase of about 0.7 MPa. Injection pore-pressure was lowered to 4.5 MPa on Day 98. Over the remaining 32 days of the low pressure constant head hydraulic test stage the strain was only partially recovered. This was accompanied by the slow decrease in pore-pressure in the injection and back-pressure guard-rings. The injection guard-ring decreased much slower than the guard-ring at the back-pressure end of the sample. By the end of this test stage an additional 0.014 % of dilational strain occurred.

The hydraulic permeability was modelled as being $5.8 – 7.0 \times 10^{-21}$ m^2 with a specific storage of 1.3×10^{-5}.m^{-1}. These results are similar to the permeability results reported by Harrington *et al.* (2012) for COx tests conducted perpendicular to bedding. However, specific was higher for the current test, suggesting that certain inter-beds have more storage capacity and are more permeable than others and these are more accessible in tests conducted parallel to bedding.

Gas testing was initiated on Day 131, with gas entry achieved after three constant-flow ramp stages. The increase in gas pressure resulted in only small amounts of volumetric strain, with approximately 0.02 % strain (contraction) observed as gas pressure increased. During the increase in gas pressure from 4.5 MPa to 9.5 MPa volumetric strain is very small and essentially may be considered to be iso-volumetric. Therefore the increase in gas pressure results in only localised changes in pore-pressure close to the injection port and that the bulk pore-pressure of the sample does not undergo any change in pore-pressure. This is confirmed by the small changes in pressure observed at the guard-rings.

A four stage conceptual model has been developed in order to describe all features observed in COx during the initiation of gas flow.

Stage 1 of gas migration: At about Day 220 gas started to enter the sample when the gas injection pressure was 10 MPa. Gas migrated as far as the load-cell, where it was identified as an anomalous reading. It is probable that gas had migrated along a single bedding layer of the COx as the test sample was oriented parallel to bedding. Gas propogation was along dilatant pathways that exploited the pore network of the material. The pathways can be visualised as “ruptures” in the pore network. Around each pathway the fabric would have compressed, which may lead to localised movement of water away from the pathways.

Stage 2 of gas migration: Gas propogation throughout the sample was migrating further and had reached the corner of the sample, as seen by the onset of pressure rise at the guard-ring. The geometry of the SPP apparatus means that gas was injected horizontally at one end of the sample. Therefore, when gas reached the injection guard-ring it displaced water from the guard-ring into the sample until the guard-ring was saturated with gas (slug flow). Early in the gas migration water was being displaced into the sample, resulting in small amounts of swelling due to the sample being not fully saturated. This stage was identified by a slow increase in injection guard-ring pressure. The start of the stage occurred at Day 237.32 with a second anomalous reading in the injection-end load cell signifying the movement of gas. Pressure in the guard-ring started to increase at Day 238.55. A day later at Day 239.8 the first indication of deformation was recorded at the mid-plane array of radial strain measurement devices.

Stage 3 of gas migration: A large increase in pore-pressure at the injection guard-ring occurred at Day 238.55 and was likely to be the result of a major conductive feature being formed in the sample. As this propagated through the sample it resulted in an accelleration of dilatant deformation. It can be seen that the accelleration of deformation at the mid-plane first occurred 32 days after the first indication of gas migration at Radial 2. Dilatant deformation increase occurred 0.7 days later in Radial 1 and a further 0.4 days later in Radial 3. However, axial deformation did not start to accellerate until 11 days after Radial 2. If all of the observed radial deformation was as a result of water being displaced from the guard-ring into the sample it would be expected that axial deformation would have reacted first. Therefore the observed dilatancy cannot be described completely as caused by swelling. Stage 3 also showed the onset of outflow of fluid from the sample and therefore must indicate gas movement. Although the experimental geometry is likely to result in swelling, the majority of observed deformation was caused by the dilatant propagation of gas along pathways.

Stage 4 of gas migration: Gas had propagated through the sample as far as the back-pressure end. The onset of gas reaching the back-pressure guard-ring at Day 273 indicated that gas was now moving throughout the entire length of the sample. During this stage the sample continued to dilate, which suggests that the number of gas pathways was increasing.

The observed events show that gas reached the injection guard-ring at Day 238.55, dilatancy was first seen at the mid-plane at Day 239.8 and the back-pressure guard-ring started to increase at Day 240.5. This means that the pressure pulse propogated at a rate of approximately 37.6

mm.day^{-1} or 1.6 mm.h^{-1}. This is interpreted as being a hydro-mechanical response and is created by a change in effective stress as gas started to propogate into the sample.

The accelleration of strain at the mid-plane occurred at approximately Day 255, whereas pressure at the back-pressure guard-ring initiated at Day 240.5 (nearly 15 days previous). This suggests that the back-pressure response was a hydromechanical response, whereas the accellerated dilatation was one of gas movement. The pressure increase in the injection pressure guard-ring was unstable and this was indicative of gas propogation, whereas the pressure increase at the back-pressure guard-ring was gradual and suggests that this response was not indicative of gas reaching the back-pressure end of the sample and was the result of the hydromechanical coupling. Gas is inferred as reaching the back-pressure end at Day 273. The accelleration of dilation caused by the propogation of dilatant gas pathways at the mid-plane and the inferred onset of gas reaching the back-pressure end give a gas propogartion rate of approximately 100 μm.h^{-1}. This means that per annum gas may have moved 0.85 m.

The interpretation has three components; 1) a response caused by the expulsion of water from the injection guard-ring due to the geometry of the test set-up and the resultant swelling of COx; 2) a hydro-mechanical response of the COx as a result of the change of pore-pressure from ambient (4.5 MPa) to the injection gas pressure (10 MPa); 3) a dilatant response as gas propogates through the sample. It is challenging to decouple all three components fully. However, taking all observations into consideration and comparing with observations from other tests at BGS and elsewhere a three stage model has been proposed for gas flow in COx.

Stage 1: At the gas entry pressure, gas began to enter the sample. It is probable that gas migrated along a single bedding layer of the COx as the test sample was oriented parallel to bedding. Gas propagation was along dilatant pathways that exploited the pore network of the material; the pathways can be visualised as “ruptures” in the pore network. Around each pathway the fabric compressed, which may lead to localised movement of water away from the pathways.

Stage 2: The dendritic network of dilatant pathways propagated further into the sample and reached the mid-plane. This resulted in an acceleration of dilatant deformation. Stage 2 also showed the onset of marked outflow from the sample. If all deformation was explained as derived from swelling this would not result in outflow from the sample.

Stage 3: Gas had propagated through the sample as far as the back-pressure end. The onset of gas reaching the back-pressure guard-ring indicated that gas was now moving throughout the entire length of the sample. During this stage the sample continued to dilate, which may indicate that the number of gas pathways was increasing. Stage 3 can be seen to be the formation of a major conductive feature that connected both ends of the sample. These major features may have been the formation of dilatant fractures as seen in the sample at the end of the test.

The observed dilatant net volume increase of the COx during testing could be interpreted to be resultant from a change in effective stress. The injection of gas will raise pore-pressure from 4.5 MPa to the gas injection pressure (approximately 10.5 MPa). Assuming that the entire pore network of the sample experienced this 6 MPa change in pore-pressure, the sample strain was estimated to be 78 µl. This is much less (~20 %) than the total sample deformation recorded of 360 µl. However, the experimental set-up measures pore-pressure at four locations (injection, injection guard-ring, back-pressure and back-pressure guard-ring) and this shows that the bulk sample did not undergo a 6 MPa increase in pore-pressure. A mean pore-pressure of 7.9 MPa was observed which gives a change in average pore-pressure of just 3.4 MPa. This would give an elastic deformation of 40 µl. Therefore the full deformation seen by the sample cannot be explained by elastic deformation of the sample water alone.

The recording of pore-pressure at four locations (injection, injection guard-ring, back-pressure and back-pressure guard-ring) shows that the pore-pressure distribution within the test sample is complex. The guard-ring and pressure ports are separated by 12 mm and significantly different pressures are observed. At the injection end of the sample 5.3 MPa difference in pressure was noted between injection port and guard-ring. This demonstrates that pore-pressure increase is very localised and COx is able to sustain considerable pressure gradients over small distances. This makes the use of Terzaghi's law of effective stress difficult and care needs to be taken in adopting this approach.

Flow shut-off

Prior to achieving steady-state flow and equilibration of volumetric strain the outflow from the sample unexpectedly shut-off.

Flow at the injection end of the sample increased and peaked at approximately Day 311 and this may have been the driver for the reduction in outflow from the sample that begin around Day 320. The reduction of outflow corresponded with a change in radial strain (contraction of the sample), a reduction of inflow and a reduction of pressure in the back-pressure guard-ring. A few days following the reduction of outflow the injection-end guard-ring pressure increased to approximately equal the injection pressure; this event corresponds with a short-lived peak of inflow. This is likely to be the formation of a major conductive pathway between the injection port and the guard-ring. Mode-I (pull-apart) type fractures were seen in the fracture at the end of the test. Although these would explain the connectivity between the guard-ring and injection port other evidence does not support the formation of a fracture at this time; namely the lack of dilatant deformation seen at the radial mid-plane. Therefore it is likely that the fractures seen post-testing were made at the time of lowering test pressure to ambient levels when decommissioning the test. This would result in the expansion of trapped gas and if this gas was not able to drain it would result in mode-I fracturing. There is evidence of multiple pathways forming through the sample and these may have been the cause of the increase in pressure in the guard-ring.

Gas leakage from the experimental apparatus can be discounted as a cause of shut-off; either through the seal between jacket and loading plattens or by diffusion through the Hoek-sleeve. The decommissioning of the test did observe a "frothy" nature to the confining glycerol that may indicate that gas was entering the confining system. However, close examination of all behaviour means that gas leakage can be discounted as the cause of the shut-off. At the start of the flow reduction it can be seen that inflow increased, meaning it is possible a fracture or conductive pathway formed at this time at the injection end of the sample. However, following this event, flow at the injection end reduced to a condition of no-flow. If shut-off was the result of gas leakage from the apparatus it would be expected that inflow would have increased. It would then be expected that the pressure in the conductive pathways would reduce as gas was lost and this could result in the closure of the formed dilated pathways. The reduction of inflow does not support this hypothesis, nor does the retention of high pressure in the injection guard-ring. The change in confining system volume suggests that no significant gas volume was added to this part of the experimental system. Therefore, although gas leakage from the system cannot be ruled out, it is unlikely to be the cause of the shut-off.

By the end of full shut-off of flow the sample had recovered radial strain and back-pressure guard-ring pressure was similar to back-pressure. A degree of permanent deformation was noted and this is likely to correspond with gas trapped within the sample.

The raising of the injection gas pressure did not result in the re-opening of the conductive features within the sample and outflow and inflow remained low. Therefore, the cause of self-sealing was effective and the sample was now sustaining higher gas pressures without flow through the sample. This suggests that some form of localised consolidation must have occurred near to the injection port.

The cause of shut-off is therefore unknown. Experimental evidence suggests that mode-I type fractures may have been the cause of the shut-off by lowering gas pressure within the conductive pathways resulting in their closure; although the inflow and outflow data do not support this hypothesis.

In order to re-initiate gas flow, the back-pressure was lowered in steps from 4.5 MPa to 1 MPa. This has the result of increasing effective stress and increases the gas gradient along the length of the sample. However, this did not result in re-initiating flow through the sample and only resulted in draining the sample, leading to compaction. As seen with test SPP_COx-1, large samples of COx have considerable time dependent deformation that is a combination of material creep and drainage. Therefore the outflow seen is the result of this considerable time-dependent feature. It can be seen that outflow from both ends of the sample are remarkably similar showing that the outflow is the result of sample drainage and not related to gas flow through the sample.

The experimental setup is not able to determine the phase of the outflow, be it gas or water. The final saturation of the sample was determined to be indistinguishable from 100%. Therefore it is likely that the outflow is the expulsion of gas, and possibly free water, from the sample as a result of bulk compaction.

A reduction in back-pressure results in bulk sample volume reduction. This consolidation increases gas entry pressure. During the shut-off stage it was seen that the reduction in pressure at the back-pressure guard-ring (BGR) was the first recorded event. It is possible that this lowering of pressure resulted in localised consolidation and that this caused the flow to shut-off. The cause of the reduction in BGR pressure has been suggested to have been the formation of a conductive micro-fracture linking the guard-ring with the pressure port. It may be possible that the formation of the fracture/conductive pathway ultimately resulted in the closure of flow through the sample due to the localised nature of the flow paths and their inherent instability being strongly linked with the consolidation of the sample.

References

British Geological Survey holds most of the references listed below, and copies may be obtained via the library service subject to copyright legislation (contact libuser@bgs.ac.uk for details). The library catalogue is available at: http://geolib.bgs.ac.uk.

ADAMS, B.A., AND WULFSOHN, D. (1997) Variation of the critical-state boundaries of an agricultural soil. *European Journal of Soil Science*, **48**, pp.739-748.

ANAGNOSTOU, G. (1991) *Untersuchungen zur Statik des Tunnelbaus in quellfähigem Gebirge.* Dissertation **No. 9553**. ETH. Zurich, Switzerland.

ANDRA (2005) Dossier 2005 REFERENCTIEL SITE Meuse/Haute-MARNE. TOME 1, 664p.

ANDRA (2005) Dossier 2005 REFERENCTIEL SITE Meuse/Haute-MARNE. TOME 2, 353p.

ANGELI, M., SOLDAL, M., SKURTVEIT, E. AND AKER, E., (2009) Experimental percolation of supercritical CO2 through a caprock. *Energy Procedia* **1**, 3351-3358

ARISTORENAS, G. V. (1992) *Time-dependent behaviour of tunnels excavated in shale*. PhD Thesis. Massachusetts Institute of Technology. Boston, USA.

ASKARIEH, M.M., CHAMBERS, A.V., DABNIEL, F.B.D., FITZGERALD, P.L., HOLTOM, G.J., PILKINGTON, N.J. AND REES, J.H. (2000) The chemical and microbial degradation of cellulose in the near field of a repository for radioactive wastes. *Waste Management*, **20**, 93-106.

ATKINSON, J.H. AND BRANSBY, P.L. (1978) *The Mechanics of Soils: An Introduction to Critical State Soil Mechanics*. McGraw-Hill, New York.

AUTIO, J., GRIBI, P., JOHNSON, L. AND MARSCHALL, P. (2006) Effect of excavation damage zone on gas migration in a KBS-3H type repository at Olkiluotu. *Physics and Chemistry of the Earth*, **31**, 649-653.

AZIZ, K. AND SETTARI, A. (1979) *Petroleum Reservoir Simulation*. Applied Science, London.

BARLA, M. (1999) *Tunnels in swelling ground: Simulation of 3-D triaxial tests by triaxial laboratory testing*. PhD Thesis, Technical University of Turin, Italy, 179p.

BARLA, G. AND BARLA, M. (2001) Investigation and modelling of the Brenva Glacier rock avalanche on the Mount Blanc Range. *ISRM Regional Symposium Eurock 2001*, Balkema, Rotterdam, Espoo, Finlandia, 3-7 giugno, 2001

BARLA, G. (2001) *Tunnelling under squeezing rock conditions*. Eurosummer-School in Tunnel Mechanics, Innsbruck, 2001. pp.98

BELLWALD, P. (1990) *A contribution to the design of tunnels in argillaceous rock*. PhD Thesis. Massachusetts Institute of technology. Boston, USA.

BIOT, M.A. (1941) General theory of three-dimensional consolidation. *Journal of Applied Physics*, **12**, pp. 155-164.

BONINI, M. BARLA, M. AND BARLA, G. (2001) Flac applications to the analysis of swelling behaviour in tunnels. *2nd Flac Symposium on Numerical Modeling in Geomechanics, Lione, 29-31 ottobre, 2001*

BURRUS, J. (1998) Overpressure models for clastic rocks, their relation to hydrocarbon expulsion: A critical re-evaluation, in B. E. Law, G. F. Ulmishek, and V. I. Slavin, eds., *Abnormal pressures in hydrocarbon environments*: AAPG Memoir **70**, p. 35-63.

BYERLEE, J.D. (1967) Frictional characteristics of granite under high confining pressure. *Journal of Geophysical Research*, **72**, pp. 3639-3648.

BYERLEE, J.D. (1975) The Fracture Strength and Frictional Strength of Weber Sandstone. *International Journal of Rock Mechanics and Mining Sciences*, **12**, pp. 1-4.

COTECCHIA, F., AND CHANDLER, R.J. (2000) A general framework for the mechanical behaviour of clays. *Géotechnique*, **50**, pp. 431-447.

CUSS, R.J., RUTTER, E.H., AND HOLLOWAY, R.F. (2003) The Application of Critical State Soil Mechanics to the Mechanical Behaviour of Sandstone. *International Journal of Rock Mechanics and Mining Sciences*, **40**, pp. 847-862.

CUSS, R.J., HARRINGTON, J., GIOT, R., AND AUVRAY, C. (2013) Experimental observations of mechanical dilation at the onset of gas flow in Callovo-Oxfordian claystone. Clays in Natural and Engineered Barriers for Radioactive Waste Confinement: *Geological Society Special Publications*: London, United Kingdom, Geological Society of London

CUSS, R.J. AND HARRINGTON, J.F. (2010) Effect of stress field and mechanical deformation on permeability and fracture self-sealing: Progress Report on the Stress Path Permeameter experiment conducted on Callovo-Oxfordian Claystone. *British Geological Survey Commissioned Report*, **CR/10/151**. 71pp.

CUSS, R.J. (1999) *An experimental investigation of the mechanical behaviour of sandstones with reference to borehole stability*. Ph.D. thesis, Manchester, UK, University of Manchester.

DAVID, C., WONG, T.F., ZHU, W., AND ZHANG, J. (1994) Laboratory measurement of compaction-induced permeability change in porous rocks; implications for the generation and maintenance of pore-pressure excess in the crust. *Pure and Applied Geophysics,* **143**, pp. 425-456.

DEWHURST, D.N., APLIN, A.C., AND SARDA, J.-P. (1999^a) Influence of clay fraction on pore-scale properties and hydraulic conductivity of experimentally compacted mudstones. *Journal of Geophysical Research,* **104**, pp. 29,261-29,274.

DEWHURST, D.N., YANG, Y., AND APLIN, A.C. (1999^b) Permeability and fluid flow in natural mudstones. In: Aplin, A.C., Fleet, A.J., and Macquaker, J.H.S., eds., *Mud and Mudstones: Physical and Fluid Flow Properties*, Geological Society of London, Special Publications, **158**, pp. 23-43.

DIAZ-RODRIGUEZ, J.A., LEROUEIL, S., AND ALEMAN, J.D. (1992) On yielding of Mexico City clay and other natural clays. *Journal of Geotechnical Engineering American Society of Civil Engineers*, **118**, pp. 481-495.

DIMAGGIO, F.L., AND SANDLER, I.S. (1971) Material model for granular soils. *Journal of Engineering Mechanics Division, American Society of Civil Engineers*, **97**, pp. 935-950.

EKEROTH, E., ROTH, O. AND JONSSON, M. (2006) The relative impact of radiolysis products in radiation-induced oxidative dissolution of UO2. *Journal of Nuclear Materials,* **355**, 38-46.

ENGELDER, T. (1993). *Stress regimes in the lithosphere*: Princeton, NJ, United States, Princeton Univ. Press, 457 pp.

ESTEBAN, L., BOUCHEZ, J., L. AND TROUILLER, A. (2006) The Callovo-Oxfordian argillites from the eastern Paris Basin: Magnetic data and petrofabrics, *Comptes Rendus Geosciences* **338**, pp 867-881

GALLÉ, C., AND TANAI, K. (1998) Evaluation of gas transport properties of backfill materials for waste disposal: H2 migration experiments in compacted Fo-Ca clay. *Clays and Clay Minerals,* **46**, 5, 498-508.

GAUCHER, E., ROBELIN, C., MATRAY, J.-M., NÉGREL, G., GROS, Y., HEITZ, J.-F., VINSOT, A., REBOURS, H., CASSAGNABÈRE, A. AND BOUCHE, A.T. (2004) ANDRA underground research laboratory: interpretation of the mineralogical and geochemical data acquired in the Callovo-Oxfordian formation by investigative drilling, *Phys. Chem. Earth* **29**, pp. 55–77.

GEOGIANNOPOULOS, N.G., AND BROWN, E.T. (1978) The critical state concept applied to rock. *International Journal of Rock Mechanics and Mining Sciences and Geomechanics Abstracts*, **15**, pp. 1-10.

HANDIN, J., HAGER, R.V., JR., FRIEDMAN, M., AND FEATHER, J.N. (1963) Experimental deformation of sedimentary rocks under confining pressure; pore-pressure tests. *Bulletin of the American Association of Petroleum Geologists,* **47**, pp. 717-755.

HORSEMAN, S.T., AND HARRINGTON, J.F. (1994) Migration of repository gases in an overconsolidated clay. *British Geological Survey Technical Report* **WE/94/7**.

HARRINGTON, J.F. AND HORSEMAN, S.T. (1997). Projects on the effects of gas in underground storage facilities for radioactive waste (Pegasus project): Gas Migration in Clay. Proceedings of a progress meeting held in Mol, Belgium, 28 and 29 May, 1997, *European Science and Technology Series* (1998) EUR 18167 EN, pp153-173, ISBN 92-828-2757-7.

HARRINGTON, J.F. AND HORSEMAN, S.T. (1999) Gas transport properties of clays and mudrocks. In. Aplin, A.C., Fleet, A.J. and Macquaker, J.H.S. (eds) *Muds and Mudstones: Physical and Fluid Flow Properties. Geol. Soc. London, Spec. Pub.* **158**, 107-124.

HARRINGTON, J.F. AND HORSEMAN, S.T. (1999) Gas transport properties of clays and mudrocks. In. Aplin, A.C., Fleet, A.J. and Macquaker, J.H.S. (eds) Muds and Mudstones: Physical and Fluid Flow Properties. Geol. Soc. London, Spec. Pub. 158, 107-124.

HARRINGTON, J.F., DE LA VAISSIERE, NOY, D.J., CUSS, R.J., AND TALANDIER, J. (2012^a) Gas Flow in Callovo-Oxfordian Clay (COx): Results from Laboratory and Field-Scale. *Mineralogical Magazine*. December 2012, Vol. **76(8)**, pp.3303-3318.

HARRINGTON, J.F., MILODOWSKI, A.E., GRAHAM, C.C., RUSHTON, J.C., AND CUSS, R.J. (2012^b) Evidence for gas-induced pathways in clay using a nanoparticle injection technique. *Mineralogical Magazine*. December 2012, Vol. **76(8)**, pp.3327-3336.

HARRINGTON, J.F. AND NOY, D.J. (2010) Gas and water flow in the Callovo-Oxfordian argillite: Progress 2010. *British Geological Survey Commissioned Report,* **CR/10/101**. 50pp.

HARRINGTON, J.F., NOY, D.J., HORSEMAN, S.T., BIRCHALL, J.D. AND CHADWICK, R.A. (2009). Laboratory study of gas and water flow in the Nordland Shale, Sleipner, North Sea. in M. Grobe, J. C. Pashin, and R. L. Dodge, eds., *Carbon dioxide sequestration in geological media—State of the science: AAPG Studies in Geology* **59**, p. 521–543.

HARRINGTON, J.F., HORSEMAN, S.T. AND NOY, D.J. (2003) Measurements of water and gas flow in Opalinus Clay using a novel guard-ring methodology. *British Geological Survey Technical Report* **CR/03/32**, 35 p.

HARRINGTON, J.F., DE LA VAISSIÈRE, R., NOY, D.J., CUSS, R.J. AND TALANDIER, J. (2012) Gas flow in Callovo-Oxfordian Clay (COx): Results from laboratory and field-scale measurements. *Mineralogical Magazine.* December 2012, Vol. **76(8)**, pp.3303-3318,

HEILAND, J. (2003) Laboratory testing of coupled hydro-mechanical processes during rock deformation. *Hydrogeology Journal*, **11**, pp.122-141.

HOBBS, P.R.N., JONES, L.D., ROBERTS, P. AND HASLAM, E. (2010) SHRINKiT: Automated measurement of shrinkage limit for clay soils. *British Geological Survey Internal Report* **IR/10/077**.

HOEK, E., AND BROWN, E.T. (1980) Empirical strength criterion for rock masses: *Journal of the Geotechnical Engineering Division*, **106**, pp. 1013-1036.

HOLT, R.M. (1990) Permeability reduction induced by a non-hydrostatic stress field. *SPE Formation Evaluation*, **Dec 1990**, pp. 444–448

HORSEMAN, S.T., HARRINGTON, J.F. AND SELLIN, P. (1999) Gas migration in clay barriers. *Engineering Geology,* **54**, 139-149.

HORSEMAN, S.T., HARRINGTON, J.F. AND SELLIN, P. (1996). Gas migration in Mx80 buffer bentonite. In: Symposium on the Scientific Basis for Nuclear Waste Management XX (Boston), *Materials Research Society*, Vol. **465**. 1003-1010.

HORSEMAN, S.T., HARRINGTON, J.F. AND SELLIN, P. (2004) Water and gas flow in Mx80 bentonite buffer clay. In: Symposium on the Scientific Basis for Nuclear Waste Management XXVII (Kalmar), *Materials Research Society*, Vol. **807**. 715-720.

HORSEMAN, S.T., HARRINGTON, J.F., BIRCHALL, D.J., NOY, D.J. AND CUSS, R.J. (2005). Consolidation and rebound properties of Opalinus clay: A long-term, fully-drained test. *British Geological Survey Commissioned Report.* **CR/05/128.** 60 pp.

HUBBERT, M.K., AND RUBEY, W.W. (1959) Role of fluid pressure in mechanics of overthrust faulting: 1 - Mechanics of fluid-filled porous solids and its application to overthrust faulting. *Geological Society of America Bulletin,* **70**, pp. 115-166.

HUDSON, J.A., AND HARRISON, J.P. (1997) *Enginerring rock mechanics: an introduction to the principles*. Oxford, Elsevier Science Ltd.

ITASCA Inc. (1996) *FLAC 3D Fast Lagrangian Analysis of Continua.* Version 1.1, User's manual.

JONES, M.E., LEDDRA, M.J., AND ADDIS, M.A. (1987) Reservoir Compaction and Sea Floor Subsidence due to Hydrocarbon Extraction. *Offshore Technology Report* **OTH 87 276**, HMSO, London

JONES, M.E. (1994) Mechanical principles of sediment deformation. In: Maltman, A., ed., *The geological deformation of sediments*. London, Chapman and Hall, pp. 37-71.

KATSUBE, T.J., BOITNOTT, G.N., LINDSAY, P.J., AND WILLIAMSON, M. (1996) Pore structure evolution of compacting muds from the seafloor, offshore Nova Scotia. In: Anonymous, ed., Eastern Canada and national and general programs. *Current Research - Geological Survey of Canada,* pp. 17-26.

KATSUBE, T.J., ISSLER, D.R., AND COYNER, K. (1996) Petrophysical characteristics of shale from the Beaufort-Mackenzie Basin, northern Canada; permeability, formation factor, and porosity versus pressure, Interior plains and Arctic Canada. *Current Research - Geological Survey of Canada*. pp. 45-50.

KATSUBE, T.J. (2000) Shale permeability and pore-structure evolution characteristics. *Geological Survey of Canada*. Ottawa, ON, Canada. Pages: 9.

KEANEY, G.M.J., MEREDITH, P.G., AND MURRELL, S.A.F. (1998) Laboratory study of permeability evolution in a 'tight' sandstone under non-hydrostatic stress conditions. *Rock Mechanics in Petroleum Engineering*, **1** 8-10 July 1998, Trondheim, Norway, Society of Petroleum Engineers, SPE/ISRM 47265, pp. 329-335.

KIRBY, J.M. (1994) Simulating soil deformation using a critical-state model; I, Laboratory tests. *European Journal of Soil Science*, **45**, pp. 239-248.

KIRBY, J.M., AND O'SULLIVAN, M.F. (1997) Critical state soil mechanics analysis of the constant cell volume triaxial test. *European Journal of Soil Science*, **48**, pp. 71-78.

KREIS, P. (1991) Hydrogen evolution from corrosion of iron and steel in low/intermediate level waste repositories. *Nagra Technical Report,* **NTB 91-21**.

KWON, O., KRONENBERG, A.K., GANGI, A.F., AND JOHNSON, B. (2001) Permeability of Wilcox Shale and its effective pressure law. *Journal of Geophysical Research, B, Solid Earth and Planets,* **106**, pp. 19,339-19,353.

LEDDRA, M.J., JONES, M.E., AND GOLDSMITH, A.S. (1993) Compaction and shear deformation of a weakly-cemented, high porosity sedimentary rock. In: Moon, C.F., ed., *The Engineering Geology of Weak Rock*., **8**: Engineering Geology Special Publication, Geological Society of London, pp. 45-54.

LEDDRA, M.J., PETLEY, D.N., AND JONES, M.E. (1992) Fabric changes induced in a cemented shale through consolidation and shear. In: Tillerson, J.R. and Wawersik, W.R. eds, *Rock Mechanics, Proceedings of the 33rd U.S. Symposium*, Balkema, Rotterdam.

LOE, N.K., LEDDRA, N.M., AND JONES, M.E. (1992) Strain states during stress-path testing of the Chalk. In: *Rock Mechanics. Proceedings of the 33rd U.S. Symposium*, Tillerson, J.R. and Wawersik, W.R.W. (eds.), A.A. Balkema, Rotterdam, pp.927-936.

MAÂTOUK, A., LEROUEIL, S., AND LA ROCHELLE, P. (1995) Yielding and critical state of a collapsible unsaturated silty soil. *Géotechnique*, **45**, pp. 465-477.

MALTMAN, A. (1994) *The geological deformation of sediments*. London, United Kingdom, Chapman and Hall, 362 pp.

MARSCHALL, P., HORSEMAN, S.T., AND GIMMI, T. (2005) Characterisation of Gas Transport Properties of the Opalinus Clay, a Potential Host Rock Formation for Radioactive Waste Disposal, *Oil & Gas Science and Technology – Rev*. IFP, **60**, 1, pp 121-139.

MCLINTOCK, F.A., AND WALSH, J.B. (1962) Friction on Griffith cracks in rock under pressure. *Proceedings of the 4th US National Congress on Application Mechanics*, New York.

MENÉNDEZ, B., ZHU, W., AND WONG, T.F. (1996) Micromechanics of brittle faulting and cataclastic flow in Berea Sandstone. *Journal of Structural Geology*, **18**, pp. 1-16.

MITCHELL, R.J. (1970) On the yielding and mechanical strength of Leda clays. *Canadian Geotechnical Journal*, **7**, pp. 297-312.

MORROW, C., SHI, L.Q., AND BYERLEE, J.D. (1984) Permeability of fault gouge under confining pressure and shear stress. *Journal of Geophysics Research*, **89**, pp. 3193-3200.

NERETNIEKS, I. (1984) Impact of alpha-radiolysis on the release of radionuclides from spent fuel in a geologic repository. *Materials Research Society Symposium* (Boston, USA, 14 November 1983), Volume: **26**, 1009-1022.

NEUZIL, C.E., BREDEHOEFT, J.D. AND WOLFF, R.G. (1984) Leakage and fracture permeability in the Cretaceous shales confining the Dakota aquifer in South Dakota. In: *Proceedings of First C.V. Theis Conference on Geohydrology* in Dublin, Ohio. Jorgensen, D.G. and Signor, D.C. (eds.). National Water Well Association. pp.113-120.

NG, R.M.C., AND LO, K.Y. (1985) The measurements of soil parameters relevant to tunnelling in clays. *Canadian Geotechnical Journal*, **22**, pp. 375-391.

OHNAKA, M. (1973) The quantitive effect of hydrostatic confining pressure on the compressive strength of crystalline rocks. *J. Phys. Earth*, **21**, pp. 125-140.

ORTIZ, L., VOLCHARET, G., DE CANNIERE, P., AERTSENS, M., HORSEMAN, S.T., HARRINGTON, J.F., IMPEY, M., AND EINCHCOMB, S. (1996). MEGAS - Modelling and Experiments on Gas Migration in Repository Host-rocks. Proc. EU PEGASUS Meeting at Rapolina-Terme, Italy, 14-15 June 1995. *Nuclear Science and Technology Series*, EUR 16746 EN, Luxembourg, 127-147.

ORTIZ, L., VOLCKAERT, G. AND MALLANTS, D. (2002) Gas generation and migration in Boom Clay, a potential host rock formation for nuclear waste storage. *Engineering Geology*, **64**, 287-296.

PETLEY, D.N. (1999) Failure envelopes of mudrocks at high confining pressures, in Macquaker Joe, H.S., ed., *Muds and mudstone; physical and fluid-flow properties*, **158**: Geological Society Special Publications London, United Kingdom, Geological Society of London, pp. 61-71.

PETLEY, D.N., JONES, M.E., LEDDRA, M.J., AND LOE, N.K. (1992) On changes in fabric and pore geometry due to compaction and shear deformation of weak North Sea sedimentary rocks. *North Sea Oil and Gas Reservoirs III*. London, Graham and Trotman.

REMVIK, F., AND SKALLE, P. (1993) Shale-fluid interaction under simulated downhole conditions, and its effect on borehole stability, in Haimson, B.C., ed., *Rock mechanics in the 1990s*., **30**; 7: *International Journal of Rock Mechanics and Mining Sciences and Geomechanics Abstracts* Oxford-New York, International, Pergamon, pp. 1115-1118.

ROCSCIENCE (1998) Examine3D, *User's Manual*. Rocsicence Inc. Univesity of Toronto

ROSCOE, K.H. AND BURLAND, J.B. (1968) On the generalised stress-strain behaviour of "wet" clay. In: *Engineering Plasticity*. Heyman, J. and Leckie, F.A. (eds.). Cambridge University Press. pp.535-609.

ROSCOE, K.H., SCHOFIELD, A., AND WROTH, C.P. (1958) On the yielding of soils. *Géotechnique*, **8**, pp. 22-53.

ROUSESET, D. AND CLAUER, N. (2003) Discrete Clay Diagenesis in a Very Low-Permeable Sequence Constrained by an Isotopic (K-Ar and Rb-Sr) Study, *Contributions to Mineralogy and Petrology*, **145**, pp 182-198.

SCHOFIELD, A. (1998) Mohr Coulomb error correction. *Ground Engineering*, **31**, pp. 30-32.

SCHOFIELD, A., AND WROTH, C.P. (1968) *Critical State Soil Mechanics.* London, McGraw-Hill, 310 pp.

SCHUTJENS, P.M.T.M. AND DE RUIG, H. (1997) The influence of stress-path on compressibility and permeability of an overpressurised reservoir sandstone: some experimental data. *Phys Chem Earth*, **22,** pp. 97–103

SHAH, K. (1997) An elasto-plastic constitutive model for brittle-ductile transition in porous rocks. *Proceedings of the 29th Symposium on Fatigue and Fracture Mechanics*, ASTM, Standford, California, June 1997.

SMART, N.R., CARLSON, L., HUNTER, F.M.I., KARNLAND, O., PRITCHARD, A.M., RANCE, A.P. AND WERME, L.O. (2006).. Interactions between iron corrosion products and bentonite. *Serco Assurance Report,* **SA/EIG/12156/C001.**

STEINER, W. (1992) Swelling rocks in tunnels: characterisation and effect of horizontal stresses. *Eurock '92*. pp. 163-168. Thomas Telford. London, U.K.

TAVENAS, F., AND LEROUEIL, S. (1977) Effects of stresses and time on yielding of clays . *Proceedings of the 9th International Conference on Soil Mechanics*, Tokyo, 1977.

TERZAGHI, K. (1943) *Theoretical Soil Mechanics*. New York, John Wiley.

VAUGHAN, P.R. (1985) Mechanical and hydraulic properties of *in situ* residual soils. *First International Conference in Geomechanics of Tropical and Saprolitic Soils*, Brasilia, Brasil.

WALSH, J.B., AND BRACE, W.F. (1984) The effect of pressure on porosity and the transport properties of rock. *Journal of Geophysical Research. B*, **89**, pp. 9425-9431.

WEETJENS, E. AND SILLEN, X. (2006).. Gas Generation and Migration in the Near Field of a Supercontainer-Based Disposal System for Vitrified High-Level Radioactive Waste, *Proc. 11th Int. High-Level Radioactive Waste Management Conf.* (IHLRWM), Las Vegas, Nevada, April 30–May 4, 2006.

WENK, H.-R., VOLTOLINI, M., MAZUREK, M., VAN LOON, L.R. AND VINSOT, A. (2008) Preferred Orientations and Anisotropy in Shales: Callovo-Oxfordian Shale (France) and Opalinus Caly (Switzerland), *Clays and Clay Minerals*, **56**, pp 285-306.

WHEELER, S.J., AND SIVAKUMAR, V. (1995) An elasto-plastic critical state framework for unsaturated soil. *Géotechnique*, **45**, pp. 35-53.

WIKRAMARATNA, R.S., GOODFIELD, M., RODWELL, W.R, NASH, P.J. AND AGG, P.J. (1993).. A preliminary assessment of gas migration from the Copper/Steel Canister. *SKB Technical report* **TR93-31**.

WILEVEAU, Y., AND BERNIER, F. (2008) Similarities in the hydromechanical response of Callovo-Oxfordian clay and Boom Clay during gallery excavation. Physics and Chemistry of the Earth, 33, S343–S349.

WONG, T.-F., DAVID, C., AND ZHU, W. (1997) The transition from brittle faulting to cataclastic flow in porous sandstones; mechanical deformation. *Journal of Geophysical Research, B, Solid Earth and Planets*, **102**, pp. 3009-3025.

WOOD, D.M. (1990) *Soil behaviour and critical state soil mechanics*. Cambridge, United Kingdom, Cambridge University Press, 462 pp.

ZHANG, C-L, ROTHFUCHS, T., SU, K., AND HOTEIT, N. (2007) Experimental study of the thermo-hydro-mechanical behaviour of indurated clays. *Physics and Chemistry of the Earth*, 32, 957–965.

ZHU, W., AND WONG, T.-F. (1997^a) Shear-enhanced compaction in sandstone under nominally dry and water-saturated conditions. In: Kim, K., ed., *ISRM international symposium, NY Rocks '97. International Journal of Rock Mechanics and Mining Sciences and Geomechanics Abstracts*, **34**, pp. 372.

ZHU, W., AND WONG, T.-F. (1997^b) The transition from brittle faulting to cataclastic flow; permeability evolution. *Journal of Geophysical Research, B, Solid Earth and Planets*, **102**, pp. 3027-3041.

ZHU, W., MONTESI, L.G.J., AND WONG, T.-F. (1997) Shear-enhanced compaction and permeability reduction: Triaxial extension tests on porous sandstone. *Mechanics of Materials*, **25**, pp. 199-214.

ZHU, W., AND WONG, T.F. (1994) Permeability evolution related to the brittle-ductile transition in Berea Sandstone. In: Anonymous, ed., *AGU 1994 fall meeting.*, **75; 44 Suppl.**: *Eos*, Transactions, American Geophysical Union. pp. 638.

ZOBACK, M.D., AND BYERLEE, J.D. (1975) The effect of microcrack dilatancy on the permeability of Westerly Granite. *Journal of Geophysics Research*, **80**, pp. 752-755.

Appendix 1

Time	Injection flow	Injection guard	Back-pressure guard	Load cell	Radial strain 1	Radial strain 2	Radial strain 3	Axial strain	Back-pressure flow	Related to temperature	Pump status	Time interval	Time interval (gas)
205.75				/\	#	#	#			Y	Constant flow mode		
208.35				\/									
211.6				/\									
216				#									
218.5					#	#	#						
220				#									
220.45				#									
221.875	**#**			↓									0.0
222.25					#	#	#			?			0.4
223.5				/\									1.6
232.85		#	#				Blip			?			11.0
233				#									11.1
233.95				#									12.1
235.25							#			?			13.4
235.87		#	#							?			14.0
236.2					#	↓				?			14.3
236.5				#min		\/	#			/\			14.6
237.32				↑									15.4
237.57				/\									15.7
238.55		**Gas**		#									16.7
239.8					#	**#_**	#						17.9
240.5			#										18.6
241.85			#	↓									20.0
242.2									**#**				20.3
243.5						**#↓**	**#_**						21.6
245.5					#	\/							23.6
246.45						/\	/\						24.6
247.5									#				25.6
250					/\								28.1
251.5					#		#						29.6
254						↓↓						**0**	32.1
254.5									#			0.5	32.6
254.7037		↑			↓↓			#				**0.7**	32.8
255.03											Constant pressure mode	1.0	33.2
255.13		/\					↓↓					**1.1**	33.3
255.6			#						#			1.6	33.7
256.5				#								2.5	34.6
257									#			3	35.1
262				/\					#			8	40.1
265.03								↑				**11.0**	43.2
269.5									#_				47.6
271.1				↑									49.2
273			# **Gas**										51.1
273.105			\/										51.2
273.4			#										51.5
273.9			#										52.0
274.05			\/										52.2
274.3			#										52.4
274.9			↓										53.0

Table 0-9 Summary of all events relevant to onset of gas flow through the COx. Key: # = deflection in reading; #_ = reading has reached plateau; ↑ = sharp increase in reading; ↓ sharp decrease in reading; ↓↓ = onset of accelerated radial strain; /\ = peak in reading; \/ = trough in reading; Gas = evidence that gas has reached guard-rings.